DIPLOMARBEIT

PHOTOINDUCED CHANGES OF ELECTRICAL PROPERTIES IN SrTiO₃

ausgeführt am

Institut für Chemische Technologien und Analytik,

FB Elektrochemie,

der Technischen Universität Wien

unter Anleitung

*von Univ.-Prof. Dipl.-Phys. Dr. Jürgen **Fleig** und Univ.Ass. Dipl.-Ing. Dr.rer.nat. Markus **Kubicek***

durch

Richard Peter Barna

Matrikelnummer: 01427689

Adelheid-Popp Gasse 24 2/6/03/01

A-1220 Wien

Wien, am 13.11.2018

Richard Barna

Abstract

An enhanced oxygen incorporation rate into the $SrTiO_3$ lattice induced by ultraviolet light, was first reported in the early 2000's and was solely studied in one further work, leading to a limited insight into the effect as of today. In the present thesis this photoelectrochemical interaction was further investigated in order to get a deeper understanding of the underlying processes. Single crystal undoped $SrTiO_3$ was chosen as the optically active material. Thin film electrodes were deposited on both sides and the working electrodes were microstructured into either a grid shape or into circular microelectrodes. Systematic measurements of electrochemical impedance spectroscopy (EIS), as well as photovoltage and photocurrent measurements were conducted on the samples in air, at different temperatures, while exposed to ultraviolet light and in dark. The effect of the electrode material was investigated as well, using a metal (platinum), a mixed ionic electronic conductor (LSC, $La_{0.6}Sr_{0.4}TiO_3$), and a transparent conductor (Al doped ZnO). Impedance spectra showed the existence of three semicircles, which were analyzed, interpreted and consequently an improved equivalent circuit was suggested. UV light in general caused the decrease of the resistance of all processes, however increasing temperature leads to a diminishing light effect. The electrode material was found to not only affect the space charge related effects, but also the equilibration time under and after UV irradiation. Photovoltage and photocurrent measurements showed, that ultraviolet light induces two separate processes in the sample; on one hand a space charge related photovoltage, on the other hand a stoichiometry change caused by an enhanced oxygen incorporation rate.

Kurzfassung

Eine erhöhte Sauerstoffeinbaurate in das $SrTiO_3$-Gitter, induziert durch ultraviolettes Licht, wurde erstmals in den frühen 2000ern beschrieben und wurde nur in einer weiteren Arbeit untersucht, was zu einem bis heute nur sehr begrenzten Einblick in den Effekt. In der vorliegenden Arbeit wurde dieser photoelektrochemische Effekt weiter untersucht, um ein tieferes Verständnis der zugrundeliegenden und begleitenden Prozesse zu erhalten. Einkristallines undotiertes $SrTiO_3$ wurde als optisch aktives Material gewählt. Dünnschichtelektroden wurden auf beiden Seiten abgeschieden und die Arbeitselektroden wurden entweder zu einem Gitter oder zu kreisförmigen Mikroelektroden mikrostrukturiert. Eine systematische Versuchsreihe von Elektrochemische Impedanzspektroskopie (EIS), Photospannungs- und Photostrommessungen wurde an den Proben in Luft bei verschiedenen Temperaturen durchgeführt, während sie ultraviolettem Licht und Dunkelheit ausgesetzt wurden. Die Wirkung des Elektrodenmaterials wurde ebenfalls untersucht, wobei ein Metall (Platin), ein gemischt-ionischer elektronischer Leiter (LSC, $La_{0,6}Sr_{0,4}TiO_3$) und ein transparenter Leiter (Al-dotiertes ZnO) verwendet wurden. Impedanzspektren zeigten die Existenz von drei Halbkreisen, deren Hintergründe analysiert und diskutiert wurden, um so ein verbesserter äquivalenter Schaltkreis vorzuschlagen. Das UV-Licht verursachte in jedem Fall die Reduzierung des Widerstandes aller Transportprozesse, wobei das Ausmaß des Lichteffekts mit steigender Temperatur abnimmt. Es wurde gefunden, dass das Elektrodenmaterial nicht nur die raumladungsbezogenen Effekte beeinflusst, sondern auch die Äquilibrierungszeit unter und nach der UV-Bestrahlung. Messungen von Photospannung und Photostrom zeigten, dass ultraviolettes Licht zwei getrennte Phänomene in der Probe induziert; einerseits verursacht es eine raumladungsbezogene Photospannung andererseits eine Stöchiometrieänderung durch eine erhöhte Sauerstoffeinbaurate.

Table of Contents

Motivation

Since the beginning of known human history, we have used solely the renewable energy sources around us. Feeding the fire with biomass, using the wind, to grind grain and produce flour, bathing in hot bathes heated by geothermal energy are only a few examples.

A new era dawned at the end of the XVIII. century, when a Scottish inventor named James Watt realized the possibilities of using steam, created by burning coal, a new source of energy. In a short period of time many others followed and improved the idea, and the industrial revolution spread unstoppable through the western world. During two centuries we have learned to use fossil fuels to create electricity, to heat our homes, to drive our cars and we became fundamentally dependent on a non-renewable source of energy.

After two centuries this dependency is clearly showing its negative side-effects to us: Burning carbon-based fuels produces carbon-dioxide, which is the most significant contributor to greenhouse effect and thus to climate change, which according to even the optimistic predictions, will change our lives in the forthcoming decades. Another constant threat is the depletion of these raw materials, which in absence of alternative energy sources could lead to social unrest, and in extreme case to wars.

Although my work presented in this thesis is only a drop in the ocean, its aim is to contribute to the ever growing knowledge of alternative energy sources and therefore to a more sustainable and peaceful future for us and the next generations.

1. Introduction

Photoelectrochemistry (PEC) is concerned with the interaction of light with electrochemical systems. It is an active field of research, as it is well-aligned with the growing demand for renewable and sustainable energies. An important related research area of PEC is photovoltaics, which deals with semiconductor materials capable of converting photons into electricity by absorbing light. This is the so called photovoltaic effect.

One of the materials showing this phenomenon is strontium titanate ($SrTiO_3$, STO), which was chosen for this study. Despite the fact, that it is an already widely used semiconductor material, with many applications, and accordingly has an extensive literature, there are still unanswered questions about its behavior under UV illumination. The next section will introduce the reader to the basics of photoconductivity and solar cells, briefly go through the fundamentals of electrochemical impedance spectroscopy, furthermore present the most important properties of strontium titanate and two electrode materials used in this research. Subsequently the questions will be stated, which this thesis is concerned with.

1.1. Photoconductivity

Photoconductivity is an optoelectronic phenomenon which involves enhancement of conductivity of a material as a result of excitation of valence electrons caused by photon absorption[1]. Although organic and inorganic materials both can show photoconductive properties, this thesis will mainly concentrate on the inorganic materials, more precisely on the semiconductors as a relevant group. Photon absorption in semiconductors can be either intrinsic or extrinsic. In the case of intrinsic absorption an electron from the valence band absorbs a photon and gets excited into the conduction band (Figure 1.1(a)), creating an electron-hole pair. Extrinsic absorption can only occur in case of additional energy states in the bandgap due to impurities. In that case an electron jumps either from the valence band to an in-between state (Figure 1.1(b)), or from an in-between state to the conduction band (Figure 1.1(c)). In both cases only one type of free charge carrier gets generated. Figure 1.1(d) and (e) shows electron and hole trapping respectively. Extrinsic absorption also shows the importance of impurities and defects regarding photoconductivity.
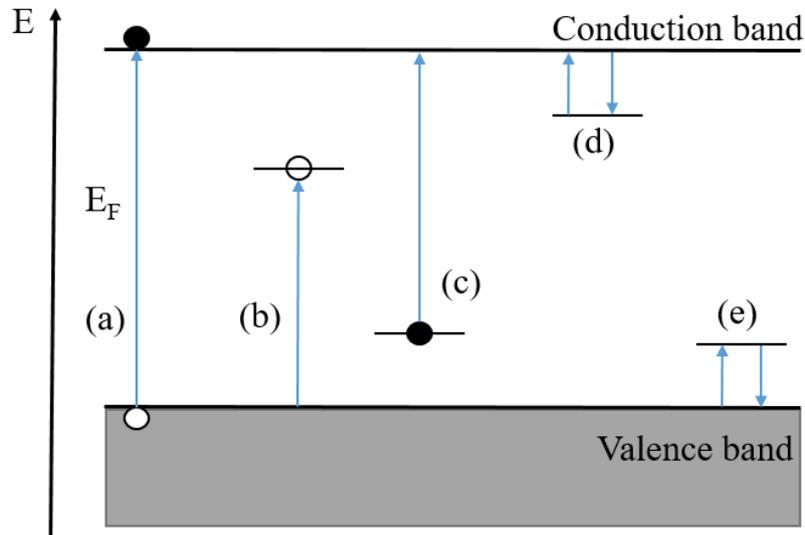
Figure 1.1 - Possibilities of electron excitation through photon absorption; (a) Intrinsic, (b) and (c) Extrinsic, (d) and (e) trapping

In case the photoconducting material is part of an electric circuit or connected to another material, the type of contacts also affects the processes. Two contact types to be considered are ohmic contact and a Schottky-junction. Generally, between a semiconductor and a metal or another semiconductor, a Schottky barrier will form due to the difference in Fermi levels (Figure 1.2).
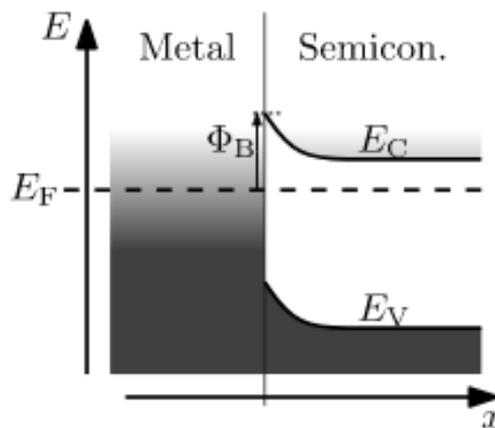

Figure 1.2 - Formation of Schottky barrier between a semiconductor and a metal[1]

---

[1] By Nanite - Own work, CC0, https://commons.wikimedia.org/w/index.php?curid=26491510

Depending on the relationship between the Fermi levels at the connection, a Schottky barrier will impede the flow of one charge carrier type. Figure 1.3. shows a p-n junction between two semiconductors. Electrons can flow freely towards the n-type conductor, but have to climb a potential barrier if the direction is switched.
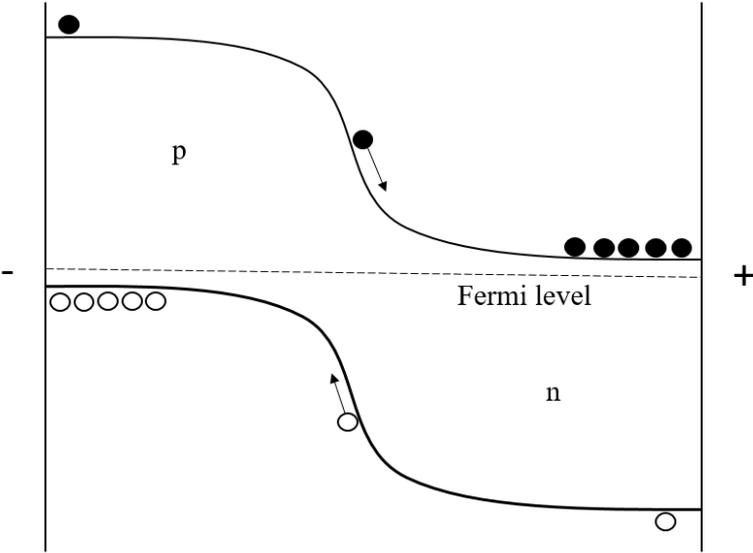
Figure 1.3 - Band schema of a p-n junction

An ohmic behavior can be achieved if the Fermi levels are close to each other.

The microstructure of the semiconductor material also plays an important role in the photoconductive properties. While a single crystal acts as a homogeneous medium, a polycrystalline material contains grain boundaries. Grain boundaries can create potential barriers similar to a back-to-back Schottky barrier. An example for an n-type material is shown in Figure 1.4. Existence of grain boundaries generally decreases electric and thermal conductive properties of a material[2].

Figure 1.4 - Energy-band diagram for an intergrain barrier in an n-type material

Photoexcitation not only increases the free electron density (Δn), but can also increase the effective electron mobility (μ^*)[3, 4]. As an example, electron holes generated through photon absorption can get captured at negatively charged grain boundaries, therefore decreasing the barrier and increasing overall electron mobility.
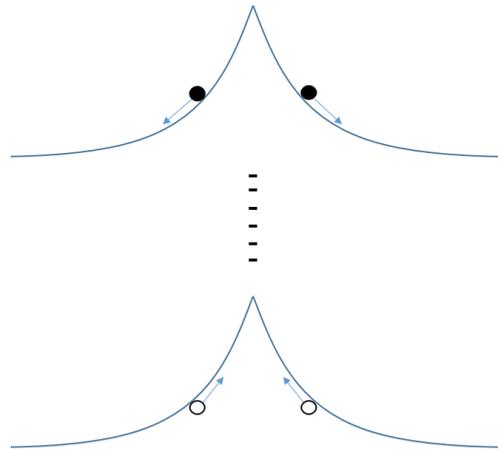
Photoconductive properties enable a large variety of applications. The most common application of photoconductors is as a photoresistor in an electric circuit. An example is polyvinylcarbazole as a conductive polymer used widely in photocopying[5]. Photoresistors can also be applied as photodetectors, such as lead sulphide, which is used as infrared detector for astronomical measurements[6]. The change in resistance is also utilized as a photodiode for instance SiC used for autocorrelation measurement of femtosecond pulses[7] or lead selenide as infrared photodiode[8]. Phototransistors applications are also known, such as GaAs structures are used as field-effect transistors[9].

1.2. Photovoltaic and solar cells

Solar cells, or photovoltaic (PV) cells, are devices capable of converting the energy of light directly into electrical energy. In order for any system to function as a PV cell it must fulfil three requirements: First upon absorption of light electron-hole pairs must be generated. Second a transport reaction must lead to the separation of these charge carriers. Finally, some sort of "check valve" is necessary, which prevents the photo-induced electrons and holes from recombination. This also implies, that an external path must exist, where the electrons can lose

their energy and recombine with the holes. Through this path the energy can be extracted e.g. by driving electrical applications or by charging energy storage devices[10]. However, there are many commercially available and even more experimental setups which fulfill these requirements, this section will only discuss semiconductor and perovskite solar cells as two relevant groups for this thesis.

Most solar cells are based on semiconductors, silicon being the prime example. The most crucial property of a semiconductor in photovoltaic research is its bandgap energy (E_g). Bandgap is the energy range between the valence band and the conduction band, where in intrinsic semiconductors no electron states exist. Photon absorption can only happen if the energy of the photon is equal to or larger than the bandgap energy ($h\nu \geq E_g$). The efficiency is the highest in case $h\nu$ equals E_g. In this case all of the photons energy is used to excite the electron from the valence band to the conduction band. If the photon energy is higher than the bandgap, absorption still takes place, however the efficiency is lower, as the energy difference dissipates in the form of heat through relaxation processes in the semiconductor. This behavior also points into a direction of the existence of an upper theoretical limit for the efficiency of such photovoltaic systems. This was calculated and discussed in detail by Shockley and Queisser[11], which later become known as the well-known Shockley-Queisser limit. They concluded that this upper limit of the efficiency for a single *p-n* junction lies at 30% with a bandgap of 1.4 eV. This limit was since then overcome by creating multijunction devices through layering materials with different bandgap energies, but most commercially available products still operate below this limit. Table 1.1. shows some examples of efficiency levels of typical solar cell devices on the market.[12]

Table 1.1 - Some examples of materials used as solar cells and their maximum efficiency[2]

Type	Efficiency [%]
Silicon (crystalline)	10.5 - 25.6
Silicon (amorphous)	10.2 - 11.4
Dye-sensitized cell	10.0 - 11.9
III-V cells	21.0 - 28.8
Organic	9.5 - 11.0

---

[2] measured under the global AM1.5 spectrum (1000W/m2) at 25 °C

Multijunction devices	12.7 - 37.9

Perovskite solar cells (PSCs), as the name suggests have a perovskite structured compound as the light harvesting active layer in them[13]. In most cases these materials are hybrid organic-inorganic lead or tin halides, but as this thesis shows binary oxide ceramics, such as strontium titanate, are also suitable candidates. It is important to note, that despite the structural similarity the two groups work on a different principle. While halide-based PSCs are classical PV cells, binary oxides build photoelectrochemical cells, which means that the illumination causes not only the classical electron-hole pair generation, but also a redox reaction in the form of oxygen-ion incorporation into the lattice. This is detailed in subsequent chapters PSCs containing organic compounds are generally simple to manufacture with wet chemical techniques, however their stability is still a problem to overcome[14-18]. On the other hand, ceramic perovskites are although stable, the manufacturing process shows disadvantages similar to other semiconductor materials (e.g. high temperature, controlled atmosphere).

1.3. Electrochemical Impedance Spectroscopy

When voltage is applied to a circuit, electric current flows through it, which is in most cases opposed by the circuit. The measure of the ability to resist the flow of current is the electrical impedance. It can be defined as the ratio of the voltage- and current-phasors at frequency (ω) [19]:

$$Z(\omega) = \frac{U}{I} \tag{1}$$

The SI unit of impedance is Ohm (Ω).

The impedance of a circuit can be measured by applying an AC voltage to an electrochemical cell, while measuring the current that flows through the cell. In electrochemical impedance spectroscopy, usually sinusoidal AC voltage is applied

$$U(t) = U_0 \sin(\omega t) \tag{2}$$

where U(t) is the voltage at any given time t, U_0 is the amplitude of the signal and ω is the radial frequency. The radial frequency can be converted to the more often used frequency by dividing it with 2π:

$$f = \frac{\omega}{2\pi} \ [Hz] \tag{3}$$

If the AC voltage is sinusoidal, the AC current signal can be analyzed by assuming a sinusoidal Fourier series. In linear or pseudo-linear systems the AC current response to a sinusoidal AC voltage will be sinusoidal, and only be shifted in phase (φ), while other variables (e.g. frequency, amplitude) will stay constant (Figure 1.5).
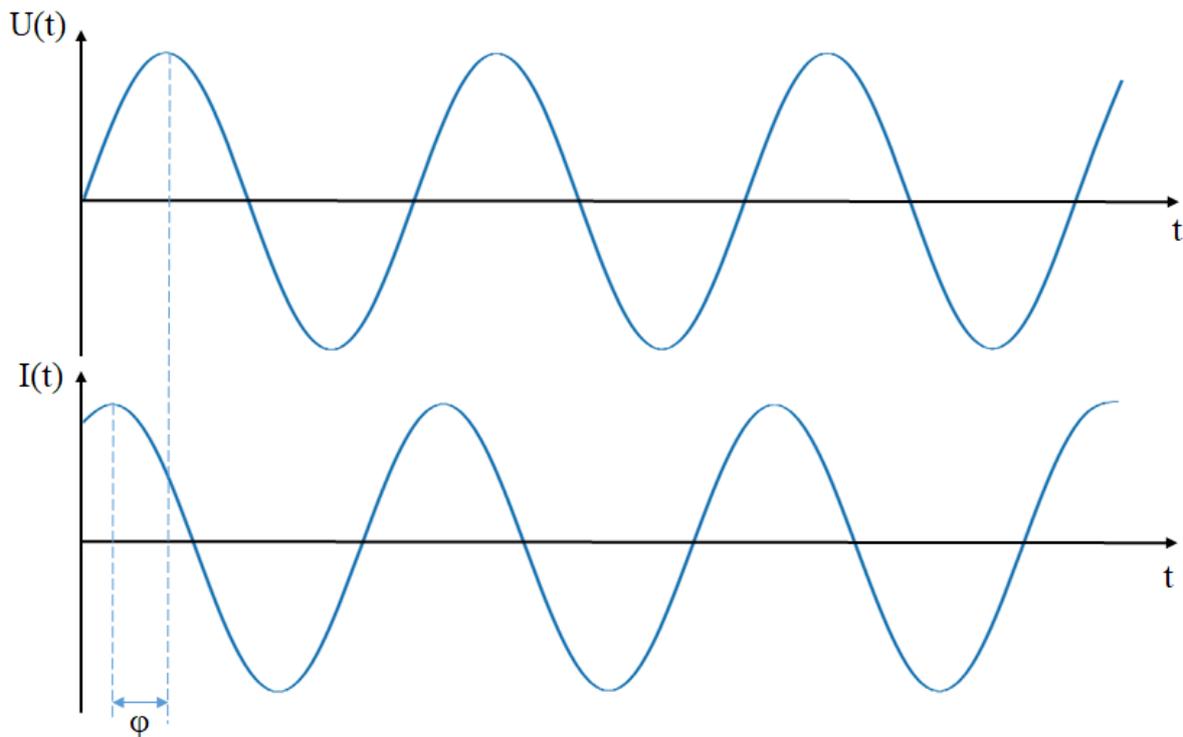

Figure 1.5 - Sinusoidal current response in a (pseudo-)linear system. φ is the phase shift

This can be expressed as the following function:

$$I(t) = I_0\sin(\omega t + \varphi) \tag{4}$$

8

where I(t) is the current signal at any given t time, I_0 is the amplitude and φ is the phase shift. If we combine equation (2) and (4) with equation (1) we can express the impedance in terms of magnitude Z_0 and phase shift φ:

$$Z(\omega) = \frac{U(t)}{I(t)} = Z_0 \frac{\sin(\omega t)}{\sin(\omega t + \varphi)} \tag{5}$$

It is also possible to express the impedance as a complex function. In this case the potential is described as

$$U(t) = U_0 e^{j\omega t} \tag{6}$$

and the current response as

$$I(t) = I_0 e^{j(\omega t - \varphi)} \tag{7}$$

By these the impedance can be represented as a complex number,

$$Z(\omega) = Z_0 e^{j\varphi} = Z_0(cos\varphi + jsin\varphi) \tag{8}$$

The impedance $Z(\omega)$ in Equation (8) can be described as a combination of a real-part ($Z_0cos\varphi$) and an imaginary-part ($Z_0jsin\varphi$). Impedance data is often presented in the form of a Nyquist plot, in which the real part of the complex impedance is plotted against the imaginary part. In the Nyquist plot the impedance is represented by a vector pointing from the origin to a given measurement point. The length of this vector is equal to $|Z|$, while the angle between the vector and the X-axis is the phase angle. However, the Nyquist plot is very helpful in identifying conduction processes, the biggest disadvantage is that the frequency is displayed on the axes and is therefore sometimes indicated at individual points.

Another often used possibility for the display of the 3-dimensinal EIS data is the Bode plot. In this case the phase angle or log(Z) is plotted against the logarithmic frequency. Although in this case all the information is visible, the measured electrochemical processes are more difficult to recognize compared to the Nyquist plot, therefore the two plotting methods are often used in parallel.

EIS measurements are simple to conduct compared to other techniques, however one has to be cautious with the results. In order for an impedance spectrum to be valid, it has to fulfil three criteria: linearity, stability and causality.

In order to achieve linearity, one can look at the Butler-Volmer equation[20, 21], which describes the relation between the current and the overpotential in an electrochemical cell:

$$i = i_0 [e^{\frac{\alpha_A nF}{RT}\eta} - e^{-\frac{\alpha_C nF}{RT}\eta}] \tag{9}$$

where i is the current, i_0 is the exchange current, η is the overpotential, α_A and α_C are the anodic and cathodic charge transfer coefficient respectively, n is the number of electrons, F is the faraday constant, R is the universal gas constant and T is the absolute temperature. According to equation (9) the current is growing exponential with increasing potential. A limiting case of the Butler-Volmer equation is the low overpotential region, where the so called polarization resistance can be deduced. In this case equation (9) can be simplified to

$$i = i_0 \frac{nF}{RT}\eta \tag{10}$$

In equation (10) the relation between the current and the overpotential is linear. Therefore, in order to fulfil the criteria of linearity, small voltages are used during EIS measurements.

Stability of the measured system is important, as an impedance measurement often takes quite some time (15-20 minutes). If the system drifts during the measurement, it can lead to false fitting results or conclusions. A good example is strontium titanate upon UV illumination,

which was measured in the framework of this thesis. As the reaction in STO is much faster than the EIS measurement, conclusions had to be made cautiously.

The third requirement for a valid EIS measurement is causality. This implies, that the measured changes should always happen due to the applied signal.

1.3.1. Evaluation and interpretation of electrochemical impedance spectra

Based on the linear circuit theory, from the viewpoint of any pair of terminals in a linear electrical circuit, the circuit behaves as if it is consisted solely of a source and an impedance [22]. In the case of EIS measurement the source is known, and the impedance can be modeled by a combination of simple circuit elements, also called an *equivalent circuit*. This approach simplifies the interpretation and calculation of otherwise complicated EIS spectra.

As in the framework of this thesis solely two-terminal circuit elements, meaning current goes in one side and exits on the other, were considered, this section will only discuss those in detail. The three basic two-terminal circuit elements are resistors (R), conductors (C) and inductors (L). The impedance of these elements are summarized in Table 1.2.

Table 1.2 – Impedance and equivalent circuit symbol of different circuit elements

Circuit Element	Impedance	Equivalent circuit symbol
Resistor (R)	$Z_R = R$	
Conductor (C)	$Z_C = 1/j\omega C$	
Inductor (L)	$Z_L = j\omega L$	

An ideal resistor has a purely real, while an ideal capacitor and inductor have purely imaginary impedance.

An ideal resistor always obeys Ohm's law[23]:

$$R = \frac{U}{I} \tag{11}$$

where R is the resistance, U is the applied voltage and I is the electric current flowing through the resistor. R is also independent from the frequency, which also means that for any AC frequency, current and voltage signals through a resistor are always in phase. Reactive circuit elements like capacitors and inductors have more complex behavior and don't follow Ohm's law.

A capacitor is a passive electrical component which stores electrical energy in an electric field [24]. An ideal capacitor has a constant capacitance which is determined by the electric charge (Q) on the conductor and the voltage (U) between them:

$$C = \frac{Q}{U} \ [F] \tag{12}$$

From the viewpoint of impedance, a capacitor causes a +90° displacement of the current signal if a sinusoidal voltage is applied:

$$I = I_0 \cos(\omega t + 90°) \tag{13}$$

On the other hand an inductor stores electrical energy in a magnetic field [24], which is generated by an electric current flowing through it. The inductance (L) is defined by the magnetic flux (ϕ) and the corresponding electric current (i):

$$L = \frac{d\Phi}{di} \tag{14}$$

The current flowing through an inductor has a phase shift of -90°.

Most of the electrochemical cells cannot be modeled by simple circuit elements. Instead combination of these elements are necessary. In the case of serial combination, the equivalent impedance equals the sum of the impedances,

$$Z_{eq} = Z_1 + Z_2 + \cdots + Z_n \tag{15}$$

while in the case of parallel connection the equivalent impedance is calculated by using the following formula,

$$\frac{1}{Z_{eq}} = \frac{1}{Z_1} + \frac{1}{Z_2} + \cdots + \frac{1}{Z_n} \tag{16}$$

In order to be meaningful, every element in the fitted model should represent an electrochemical process. This also requires preliminary knowledge of the measured system. In this section only the most relevant processes will be introduced.

Every element of an electrochemical cell generates some impedance, which has to be considered. As the electrodes are usually chosen to be good conductors, the most significant is the resistance of the electrolyte. If current flows uniformly, then the resistance can be calculated by the general equation:

$$R = \rho \frac{l}{A} \tag{17}$$

where l is the length, A is the cross-section of the electrolyte, and ρ is the resistivity. Latter is often preferred over resistance because of its size independence, which makes it easier to compare electrochemical cells with different dimensions.

In the case of uniform current flow, the electrolyte in between the two conducting electrodes can also act as a dielectric of a plate capacitor, in which case the relative permittivity of the electrolyte can be calculated by the according equation:

$$\varepsilon = \frac{C}{\varepsilon_0}\frac{d}{A} \tag{18}$$

where C is the capacitance, d is the distance between the two plates, A is the area of the plates and ε_0 is the vacuum permittivity. Unfortunately, in many cases the requirement of uniform current flow is not fulfilled, which raises the necessity of modified equations. One such relevant case is if imperfect contacts are used, such as so called microelectrodes. In this work they are used together with a large electrode in order to be able to neglect the impedance contribution at the large electrode, which is always small compared to the impedance of the cell parts close to the microelectrode.

In this work microelectrodes are understood as circular thin film electrodes with much smaller diameter than the thickness of the electrolyte. It was proved in multiple studies, that between such an imperfect contact and an extended counter-electrode most of the applied voltage drops in the vicinity of the microelectrode[25-29]. The bulk resistance, in this case often called spreading resistance(R_{spr}), is then given by the following equation[26-28],

$$R_{spr} = \frac{\rho_{bulk}}{2d_{me}} \tag{19}$$

with d_{me} and ρ_{bulk} being the diameter of the microelectrode and the bulk resistivity respectively. As in Equation (19) R_{spr} is solely dependent from the diameter, microelectrodes are often used for investigation of depth inhomogeneity. A schematic representation of the difference in depth profiling between a grid electrode and a microelectrode is shown on Figure 1.6.
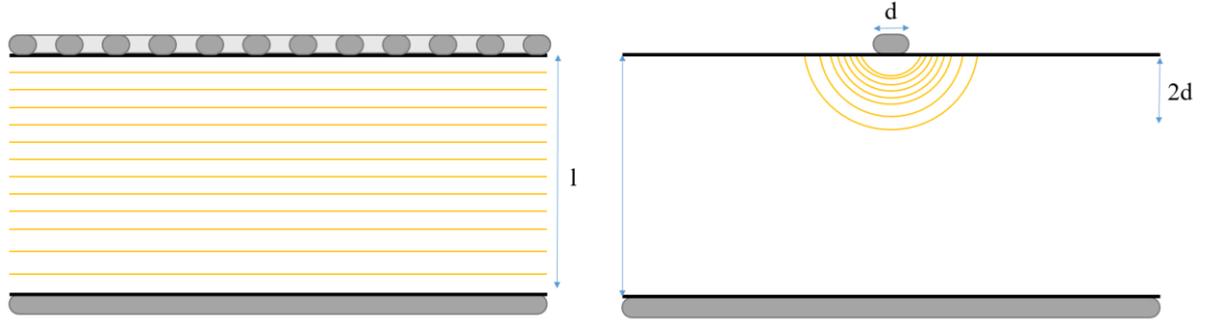
Figure 1.6 - Schematic equipotential lines in case of a grid top electrode (left) and a microelectrode of a diameter d (right)

Just as in the case of electrodes with extensive surfaces, if a voltage is applied to the electrochemical cell, a capacitance forms between the microelectrode and the counter electrode [30]. This layer can be modeled as a capacitor with a capacitance equal to

$$C = \frac{2d_{me}}{\varepsilon_{rel}\varepsilon_0} \tag{20}$$

The different capacitances of real samples are often found to be non-ideal and cannot be modeled by an ideal capacitor. Instead, in this work a constant phase element (CPE) is used [31, 32], first mentioned by Fricke[33]. A CPE has two variables: α and Q. Both are independent from the frequency. α is equal to or smaller than one. If $\alpha = 1$, then Q has a capacitive dimension, and the effective capacitance (C_{eff}) equals to Q. If $\alpha < 1$ then Q cannot represent the capacitance anymore and C_{eff} has to be extracted. Brug et al[34] developed a relationship for Faradaic systems and blocking electrodes as well, which fits the expectations of this thesis as well:

$$C_{eff} = Q^{\frac{1}{\alpha}}R_f^{\frac{(1-\alpha)}{\alpha}} \tag{21}$$

Where R_f is the resistance, which is in parallel connection with the CPE element.

As the last section showed, the most typical electrochemical processes can be represented by a combination of one or more resistors and capacitors. A parallel RC element has the characteristic shape of a perfect semicircle in the Nyquist plot[31] with the diameter R[35].

15

Measurements of electrochemical cells, however, often show a slightly distorted semicircle. In such cases a parallel connection of a resistor and a constant phase element improves the goodness of the fit (larger R^2) when fitting an equivalent circuit (Figure 1.7).
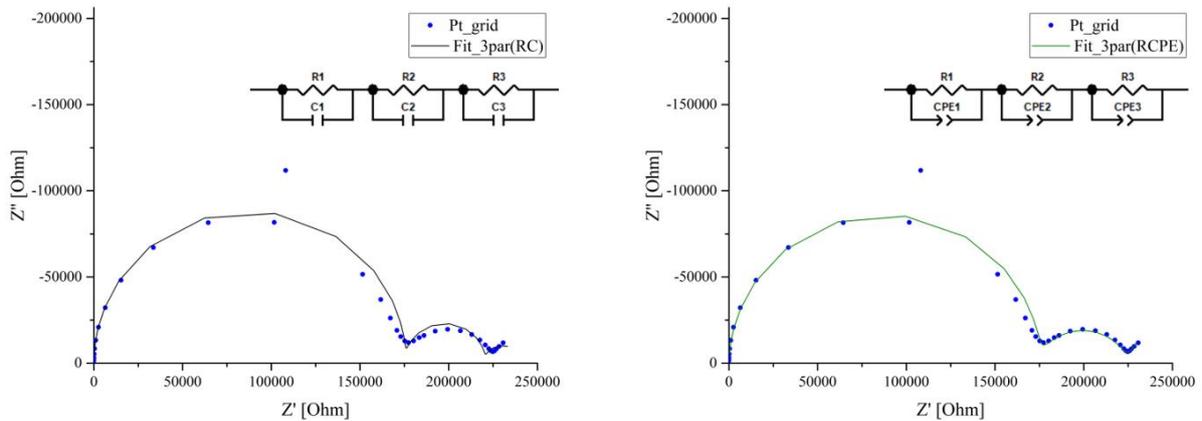

Figure 1.7 - Example of an EIS spectrum fitted with three parallel RC elements (left) and with R-CPE elements (right)

1.4. Strontium titanate

Strontium titanate (STO) is a centrosymmetric material with the chemical formula $SrTiO_3$. It has a cubic perovskite structure above 105 K (Figure 1.8)[36]. This means, that in the ideally cubic unit cell strontium-ions are sitting in the cube corner positions (red), titanium-ions in the body center positions (yellow), and oxygen-ions in the face center positions (blue). Under 105 K the structure transforms into tetragonal[37-39] with an anti-ferrodistortive transition[40]. STO is paraelectric in both structural phases. Even though under cryogenic conditions, it approaches a ferroelectric transition, stays paraelectric due to quantum fluctuations, making it a quantum paraelectric material[41]. Nonetheless "quantum ferroelectricity" can be induced in this state by oxygen-isotope exchange[42], by an external electric field[39], by stress[43] or even by calcium substitution[44]. In the low temperature region strontium titanate shows several interesting properties, such as giant piezoelectricity[45] or light-induced persistent magnetism[46]. The synthetic pure crystal is colorless or slightly yellow[47], but under reducing conditions or by donor doping, due to additional electrons in the conduction band, turns black[47-49]. It has a high refractive index (around 2.4)[50, 51], and a remarkably high relative permittivity (around 300) at room temperature, which is independent of frequency in a wide range[52]. The permittivity follows the Curie-Weiss Law on higher temperatures[52, 53],

16

but shows significant deviation at around 50 K[54], with a maximum of around 18,000 at 1.4 K in the quantum paraelectric state.
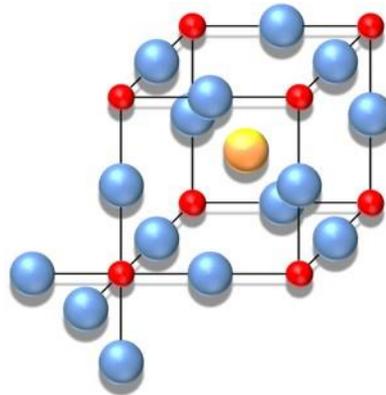

Figure 1.8 - Perovskite structure

Although the research of the electrical and conductive properties of strontium titanate dates back to the early 1950's [52], it took decades, until through modelling the defect chemistry, the behavior of STO under various conditions were fully understood, with results about the ongoing investigation of its persistent photoconductivity (PPC) from as late as 2016[55]. The next sections will try to summarize the major results and conclusions of the field.

1.4.1. Defect chemistry of strontium titanate

In the following section and later on for the description of defects in the crystal lattice the Kröger-Vink notation will be used [56].

The number and quality of point defects has a significant effect on the properties of strontium titanate. First Paladino et al. concluded, that an oxygen vacancy defect model is applicable to strontium titanate [49] and since then, many others used his model with success in their own research[57-60]. This implies, that non-stoichiometricity will mainly be compensated by oxygen vacancies[57]. Therefore, understanding the nature of these defects is fundamental to understanding the electrical behavior of bulk strontium titanate. The three main sources[61, 62] are reduction or loss of oxygen,

$$O_O \leftrightarrow \frac{1}{2} O_2(g) + V_{\ddot{O}} + 2e' \tag{22}$$
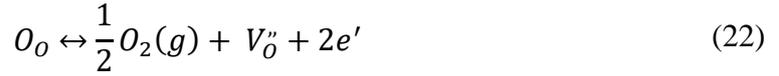
cation non-stoichiometry by means of excess TiO_2,

$$TiO_2 \rightarrow Ti_{Ti} + 2O_O + V_{Sr}'' + V_{\ddot{O}} \tag{23}$$
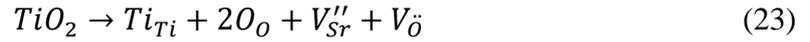
or the incorporation of acceptor-type impurities such as substitution of $2TiO_2$ for Fe_2O_3.

$$Fe_2O_3(-2TiO_2) \rightarrow 2Fe_{Ti}' + 3O_O + V_{\ddot{O}} \tag{24}$$
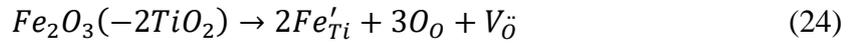
It is important to note, that the reduction reaction (22) is only reversible at elevated temperatures, as below around 500°C the surface reaction is considered frozen-in[63], and the oxygen vacancies become less and less mobile[64-67].

However, in equations (22), (23) and (24) the oxygen vacancies are doubly-ionized, multiple studies showed, that this assumption is only true on elevated temperatures, in undoped or acceptor doped samples. In case of donor doped (electron rich) STO a second ionization step occurs at around 550 °C[57, 68]:

$$V_{\ddot{O}} + e' \leftrightarrow V_{\dot{O}} \tag{25}$$

At lower temperatures oxygen vacancies trap the second electron, and stay neutral[69].

As multiple computational studies predicted[70, 71] and later Cordero et al. [72] experimentally found oxygen vacancies tend to form clusters in a linear fashion even at δ values of 0.002. Formation of pairs or chains result in higher activation energy for vacancy diffusion and a higher resistivity of the sample. Through quenching at sample production the thermodynamic equilibrium can be hindered, but annealing on 800°C enables the formation of more stable pairs.

Merkle et al. [62, 64] also found that due to electrostatic interaction, Fe'_{Ti} sites and $V_{\ddot{O}}$ can also form pairs, but these dissociate above 300°C.

Morin and Oliver[66] found, that the concentration of extrinsic oxygen vacancies (s. Eq. 24) exceeds the ones from equilibrium stoichiometry even in undoped samples, as acceptor dopants, mainly in the form of iron and aluminum impurities, are present in commercially available single crystals[73]. These unintentional dopants give rise to multiple effects, which have to be taken in consideration. Contrary to aluminum, iron is a multivalence dopant, therefore is able to trap conduction band electrons:

$$Fe'_{Ti} + e' \leftrightarrow Fe^{x}_{Ti} \qquad (26)$$

This effect decreases the overall conductance of the sample. The relative fraction of Fe^{3+}/Fe^{4+} is dependent on temperature, oxygen partial pressure and total iron concentration[64].

Additional possibility of point defects, interstitial defects are usually considered improbable in perovskites for geometrical (high packing density) and energetic reasons (higher formation enthalpy compared to Schottky defects) as well. Defects in the titanium lattice are unlikely as the Ti^{4+} ions are in deep potential minimum[74].

1.4.2. Conductive properties

The conductive properties of strontium titanate are largely dependent on temperature, point defects, doping, stoichiometry changes and even oxygen partial pressure (p_{O2})[52, 57-59, 61-63, 74-78].

Starting with the temperature, as most ceramic and semiconductor materials, STO has a negative temperature coefficient [79]. On low temperature strontium titanate is primarily a bad ionic conductor, while above ca. 750 K even though ionic conductivity increases because of the mobilizing oxygen vacancies, electronic conduction starts to dominate due to the thermal excitation of free charge carriers from the valence band [63].

As mentioned in section 1.4.1, stoichiometric, undoped STO is a slight p-type conductor, due to iron and aluminum being a significant impurity even in pure synthetic strontium titanate samples. However, by additional doping the conductive properties of strontium titanate can be tuned between a good electron conductor (e.g. Nb doping) and a good hole conductor (e.g. Fe doping).

The effect of oxygen partial pressure (p_{O_2}) on conductivity can be divided into three regions, according to which element of the charge neutrality equation is dominant[57, 61]: At extremely low p_{O_2} the reduction reaction dominates. Elimination of oxygen from the lattice generates oxygen vacancies and electrons, thus increasing the conductivity (s. also Eq. 22). In this region STO is an n-type conductor with electrons and oxygen vacancies as major charge carriers:

$$e' \approx 2[V_{\ddot{O}}] \tag{27}$$

Increasing the oxygen partial pressure will drive the incorporation of atomic oxygen, generating holes

$$V_{\ddot{O}} + \frac{1}{2}O_2 \rightarrow O_O + 2h^{\cdot} \tag{28}$$

Which then recombine with the electrons

$$nil \leftrightarrow e' + h^{\cdot} \tag{29}$$

resulting in a drop in conductivity. This process continues until the electron and hole concentration evens out, at which point the majority charge carriers are oxygen vacancies, characterized by a conductivity minimum:

$$2[V_{\ddot{O}}] = [A'] \tag{30}$$

The minimum point shifts towards lower p_{O_2} with increasing acceptor doping[75]. Further increase of the oxygen partial pressure will result in filling up of the extrinsic oxygen vacancy sites, generating electron holes (s. Eq. 28). Therefore, solely by changing oxygen partial pressure strontium titanate can become an n-type or p-type conductor.

Considering equation (22-24) the complete charge neutrality for undoped strontium titanate can be given as[61],

$$2[V_{\ddot{O}}] + [h^{\cdot}] = 2[V_{Sr}''] + [A'] + [e'] \tag{31}$$

where $[A^{'}]$ is a singly charged acceptor impurity.

1.4.3. Photo-induced changes

It is a well-established fact, that strontium titanate, as most large-bandgap semiconductors show photoconductive properties, which means that by absorbing a photon with energy at least equal to E_g ($\approx$3.2eV), an electron will get excited from the valence band to the conduction, generating an electron and hole pair[80]. However, further investigation of the interaction of strontium titanate with light is mostly restricted to the cryogen temperature range up to room temperature. In this region it was found, that STO shows green[81, 82] and blue photoluminescence[83] under UV illumination in the QPE phase[84], or at room temperature under vacuum conditions[85]. Multiple trapping effects of the photogenerated charge carriers were investigated, regarding Ti^{3+}-V_o-Ti^{3+}[86, 87] and $Fe_{Ti}'V_{\ddot{O}}$[64] defect associations, which however dissociate at elevated temperatures.

Contrary, the photo-related effects in the high temperature region were not investigated as deeply yet. Merkle et al.[88] have found, that illumination of STO with ultraviolet light induces not only photoconductivity, but also chemical changes in the form of enhanced oxygen incorporation into the lattice. From the fact, that sub-bandgap light had no such effect on the material, and that the excorporation rate stayed unchanged she concluded, that conduction band electrons play a major role in the oxygen incorporation reaction.

Further research on the high temperature light interaction of strontium titanate was done by Walch[89], who conducted extensive voltage and impedance measurements on samples with

slightly iron doped strontium titanate thin films and nominally undoped bulk samples as well, with yttria stabilized zirconia (YSZ) electrolyte. He measured the change in light effect under various temperature and atmospheric conditions, moreover the effect of the electrode material and the thickness of the electrolyte. The most important conclusion was the separation of two processes under UV illumination: The photovoltaic and the stoichiometric contribution. The former is fast (10-100 μs), and is caused by the illumination of the Schottky barrier at the STO|electrode interface, which acts as a solar cell. The latter is slower (100-1000 s), and is caused by the incorporation of oxygen into the STO lattice. If an electrolyte is also present in the photoelectrochemical cell, this creates a Nernst voltage across the cell, which is measurable after turning the UV illumination off. This means, that strontium titanate can act as a light charged battery.

1.4.4. Applications

Strontium titanate has many applications due to its remarkable properties, this section will bring a few example. STO is an often used substrate material[90], as large and precisely doped single crystals can be grown[91]. Its relatively high relative permittivity is often used in different electroceramic applications, such as a field transistor [92, 93] or a DRAM [94-96]. Due to its oxygen partial pressure sensitive conductivity, STO is often used as a high temperature oxygen sensor [97-99], or as UV-sensitive photodetector[100]. It also acts as a photocatalyst in water-splitting reactions in the presence of cocatalysts [101-103]. Its oxygen conductivity has awoken interest in the application as anode material in solid oxide fuel cells[104]. Due to its high-refractive index[50], which is close to that of diamond, it was widely used as a diamond simulant in the 1970's.

1.5. Lanthanum strontium cobaltite / Sr doped lanthanum cobaltite ($La_{1-x}Sr_xO_{3-\delta}$)

Lanthanum cobaltite is a perovskite with a chemical formula of $LaCoO_3$. In its pure form it is paramagnetic[105, 106]. On room temperature it has rhombohedral structure, with a phase transition to cubic at around 500 °C[107, 108]. This transition also occurs upon applied stress, making it a ferroelastic material[109]. In undoped form it is a p-type semiconductor.

Lanthanum cobaltite shows significant/remarkable changes upon doping. Accordingly, an extensive literature exists investigating effects of A site substitution with alkali earth elements (e.g. Ca, Ba, Sr) and 3d-transition metal substitution on B site (e.g. Mn, Fe, Ni, Cu)[107, 110-120]. However as in the framework of this thesis it is used solely as an electrode material and is not a part of the main concerns, this section is limited to the discussion of the changes upon strontium substitution in general with a focus on the properties of 40% strontium substituted lanthanum cobaltite ($La_{0.6}Sr_{0.4}CoO_{3-\delta}$, LSC).

Petrov et al.[107] have found that the rhombohedrally distorted perovskite structure of pure lanthanum cobaltite changes not only with temperature, but also depends on the amount of strontium substitution (x). In the case of x = 0.4 the transition temperature drops from around 500 °C to 290 °C. Strontium substitution above 20% also changes the magnetic property from paramagnetic to soft ferromagnetic, with a Curie-temperature of 321 K. Conductive and magnetic properties are directly influenced by the changes in defect chemistry upon doping. Petrov et al. in their research got to the conclusion that strontium substitution on the A site (Sr'_{La}) generates negative effective charge, and is compensated either by oxygen vacancies ($V_0^{\cdot\cdot}$) or by the oxidation of cobalt (Co'_{Co}). The overall electroneutrality condition is thus given by the following equation:

$$[Co'_{Co}] + 2[V_0^{\cdot\cdot}] = [Sr'_{La}] \tag{32}$$

The ratio of the compensating defects is also dependent on the strontium content (x). Under 40% doping cobalt oxidation is predominant however, on larger doping levels oxygen vacancies are more likely to form[107, 119, 121]. The relative importance of oxygen vacancies also increases with increasing temperature and with decreasing oxygen activity.

LSC also shows a metal-insulator transition [122-125] at elevated temperatures. The transition is smooth and indicated by the sign change of the temperature dependence of the conductivity, which is positive for semiconductors and negative for metals. The transition temperature decreases with increasing strontium content, while the process is also affected by oxygen non-stoichiometry. Mineshige et al.[119] have found that over 25% strontium doping, LSC shows metallic conduction already on room temperature. Petrov et al.[107] have measured an electrical

conductivity value for $La_{0.6}Sr_{0.4}CoO_{3-\delta}$ at around 3000 S/cm at 100 °C and around 1600 S/cm at 700 °C. Conductivity is also independent from oxygen activity under 500 °C.

Lanthanum strontium cobaltite is also an excellent oxygen ion conductor, thus it is also called a mixed ion electron conductor (MIEC). Berenov et al. have found an activation energy for oxygen diffusion of 1.84 eV, and a tracer diffusion coefficient in the range of 10^{-12} cm^2/s for 400 °C and 10^{-10} cm^2/s at 500°C[126].

Doped lanthanum cobaltites are used in high temperature solid oxide fuel cells (SOFC) as cathode material [127-129], while current research suggests that $La_{0.6}Sr_{0.4}CoO_{3-\delta}$ is also a promising candidate material for low temperature operation (600 °C)[130]. LSC also has catalytic properties[131], and can be used as oxygen permeation membrane [132].

1.6. Aluminum-doped zinc oxide (AZO, ZnO:Al)

Pure ZnO is an n-type semiconductor with a direct bandgap of 3.3 eV[133]. Due to its large bandgap, it is optically transparent in the visible range. At standard conditions it crystallizes in hexagonal wurtzite structure. It is widely used as a conductive, transparent window material in multi-junction solar cells[134, 135], as piezoelectric transducer[136], as invisible thin film transistor (TFT)[137-139], and in many other optoelectronic applications.

Donor doping further widens the possible field of applications. Some of the most important dopants are fluorine, boron, aluminum, gallium, indium, tin, from which aluminum stands out, by its abundance and non-toxicity. Al-doping generates a free electron in the conduction band, therefore significantly increasing conductivity, reportedly by up to six orders of magnitude[140], while also improving charge carrier density and electron mobility[141]. Incorporation of aluminum into the ZnO lattice is limited[133], which leads to a conductivity maximum at 2-3 % doping[140, 142]. AZO was extensively researched as a potential low-cost alternative to tin doped indium oxide as a transparent conductor.

1.7. Aim of the research

First Merkle [88] suggested, that the illumination of strontium titanate with UV light induces not only a photovoltaic, but also an electrochemical change in the material, in the form of

enhanced oxygen incorporation kinetic. Walch [89] later confirmed this and successfully described the voltage change, that occurs in STO under UV illumination with a two component model. However, the work of Walch also concluded, that the processes are more complex and some elements are still not understood. Consequently, the aims of this research are:

- further explore and get a better understanding of the changes in strontium titanate under UV illumination
- measure the effect of the electrode material on the light effects

2. Experimental aspects

In this section first the methods and detailed steps of sample preparation will be described, followed by characterization of the measurement setup and devices used in the framework of this thesis. Subsequently the measurement programs are introduced to the reader.

2.1. Sample preparation

In order to measure the effect of light on strontium titanate, photoelectrochemical cells with thin film electrodes on both sides were prepared. For all samples the same substrate material was used, namely, undoped single crystal $SrTiO_3$ (STO, Crystec, Germany). Three different electrode materials were chosen, platinum (Pt), lanthanum strontium cobaltite $(La_{0.6}Sr_{0.4}CoO_{3-\delta}$, LSC) and aluminum doped zinc oxide (AZO). The preparation method of metal and doped ceramic thin films differ, therefore they will be discussed separately in the next sections.

2.1.1. Samples with platinum thin film electrodes

Undoped STO single crystals, polished on both sides, of the size 10x10x0.5 mm^3 were first cut into smaller pieces obtaining four substrates of sizes varying between 3-5x10x0.5 mm^3. In the second step, the pieces were cleaned with per analysis ethanol. Afterwards an approximately 100 nm thick platinum layer was deposited by DC magnetron sputtering on both sides using a Bal-Tec Med 020 Coating System (Pt target purity 99.95% obtained from Ögussa, Austria). The sputtering parameters are summarized in Table 2.1.

Target	Pt
Desired film thickness [nm]	100
Current [mA]	100
Time [s]	150
Ar pressure [mbar]	$2*10^{-2}$

In the fourth step the top layers, in the following called top electrodes, were micro-structured into different shapes by standard lithography (negative photoresist: Micro Resist Technology - ma-N1420, developer: Micro Resist Technology - ma-D 533s). One top electrode was structured into a current collector grid with a width of 25 µm and 30 µm (s. Figure 2.1. (a)). The other three were structured into microelectrodes of different diameters (one sample with 300-200-100 µm, two samples with 200-100-50 µm, s. Figure 2.1. (b)). The micro-structuring was concluded by Ar^+ ion beam etching, 4 kV, ~1 mV. The last step of the sample preparation was a 60 seconds long ultrasonication in acetone.

2.1.2. Samples with doped ceramic thin film electrodes

The STO single crystals described in section 2.1.1 were cut and cleaned the same way. In the third step an electrode layer was deposited on both sides of the strontium titanate single crystals via pulsed laser deposition (PLD) using Kr-F excimer laser (Lambda COMPex Pro 201F, $\lambda =$ 248 nm). The LSC target was synthesized using the Pechini method[143], described in detail in the PhD thesis of G. Rupp [144]. The AZO target was prepared by a solid state ceramic synthesis route. The deposition parameters are presented in Table 2.2.

Table 2.2 - PLD parameters for two different electrode materials

Parameter	AZO	LSC

Desired film thickness [nm]	200	200
Target distance [cm]	6	6
Temperature [°C]	520-640	510-640
Cooling rate [°C/min]	15	15
O_2 pressure [mbar]	$2.0*10^{-2}$	$4.0*10^{-2}$
Laser energy per pulse [mJ]	400	400
Rate [pulse/min]	5	5
Deposition time [145]	30	30

After the deposition, the top electrodes were micro-structured into current collector grids (25 µm wide, 30 µm gap, s. Figure 2.1. (a)), or microelectrodes (200-100-50 µm in diameter, s. Figure 2.1.(b)) by the same procedure as for the samples with platinum layers described in section 2.1.1.
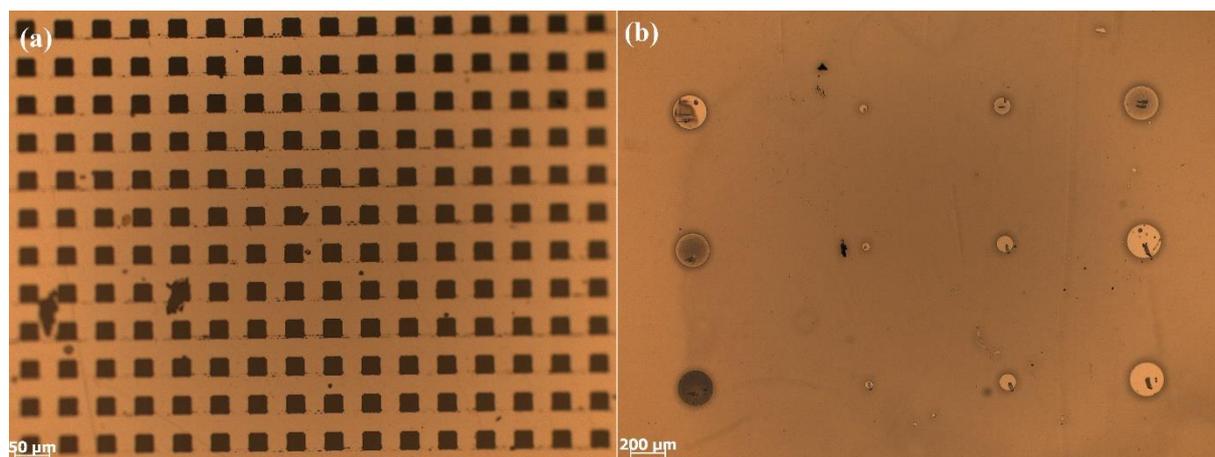
Figure 2.1 - Microscope image of the microstructured top electrodes with grid (a) and microelectrodes (b)

2.2. Measurement setup

The electrochemical measurements were conducted on a micro-contact heating stage. This complex setup is described in detail by T. Huber [146]. On top the samples were contacted with a platinum tip, which was attached to a piezoelectric microcontroller, and on bottom with a conducting platinum plated sapphire plate, respectively. The electrochemical impedance spectroscopy (EIS) and the DC current measurements were carried out on an Alpha-A High Performance Frequency Analyzer (Novocontrol Technologies, Germany) with a POT/GAL interface. In AC modus the voltage was set to 10 mV (RMS), and was only increased to 50 mV (RMS) in the case of platinum microelectrode samples due to higher noise levels. The DC current was measured at zero external potential. The voltage in DC modus was measured on a Keithley 2000 multimeter. In both DC measurements the time resolution was set to 0.1 sec, or with other words 10 measurement point were taken per second.

The UV source was a light-emitting diode (LED) element (Led Engin LZ4-00U600; 365 nm, 11 W electric power), which was mounted on top of the sapphire window of the measurement chamber. The distance between the sample and the LED was roughly 2.4 cm. In depth analyzation and intensity calculation of the LED was previously conducted by Rotter [147]. Contrary to the data sheet, which suggests a power yield of around 60 mW/cm^2, Rotter found that the intensity of the LED's power was closer to 6.2 or 8.6 mW/cm^2. In his PhD thesis Walch [89] has measured the transmission spectrum of the sapphire window, and observed an almost constant 80-90% transmission on a range from 250 to 1,000 nm.

Optical microscope images were taken with a Zeiss Imager.M1m.

2.3. Measurement program

The AC measurements were conducted following the same temperature and UV program for every sample. This program is summarized in Figure 2.2.
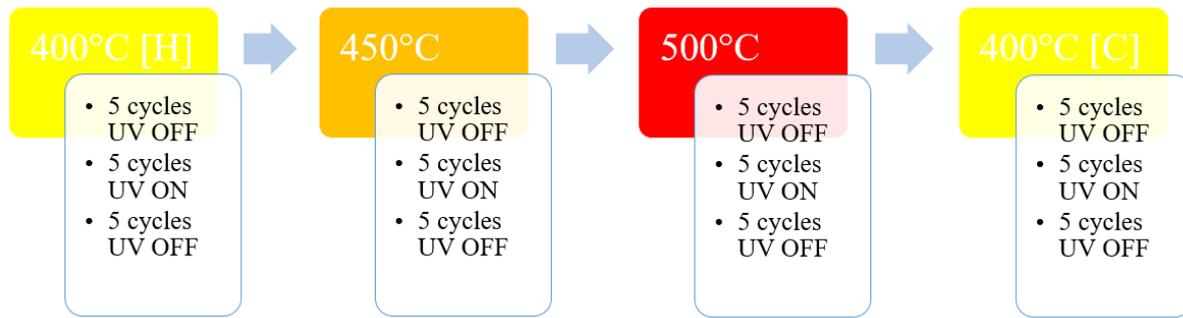
400°C [H]	450°C	500°C	400°C [C]
• 5 cycles UV OFF • 5 cycles UV ON • 5 cycles UV OFF	• 5 cycles UV OFF • 5 cycles UV ON • 5 cycles UV OFF	• 5 cycles UV OFF • 5 cycles UV ON • 5 cycles UV OFF	• 5 cycles UV OFF • 5 cycles UV ON • 5 cycles UV OFF

Figure 2.2 - Measurement program of the AC modus

The temperature program consisted of four steps: 400°C, 450°C, 500°C and again 400°C. The lowest temperature was chosen to be 400°C, as on one hand below 400°C, the oxygen exchange reaction rate is extremely low, and therefore technically considered frozen-in[64-67]. On the other hand, below 400°C the impedance of the strontium titanate substrate is too high to be easily measured. The upper limit was decided to be 500°C as previous experiences in the working group showed, that in some cases the platinum lifts-off the surface of the STO at around temperatures higher than 530°C [89]. The samples were measured a second time at 400°C in order to determine, whether any change occurred in the sample at 500°C. To distinguish the two measurements on the same temperature, the first step is referred to as 400°C [H], which stands for "heat up", and the fourth step as 400°C [C], acronym for "cool down". The samples were measured in a frequency range of $10^6 - 10^{-1}$ Hz. One full measurement in this range is referred to as a *cycle,* and it lasts approximately 3 minutes. Five such cycles were measured in each of the three steps of the UV illumination program: One before, one during and one after UV illumination. The whole measurement was controlled automatically using a JavaLab program.

The DC measurement (photovoltage and photocurrent) program consisted also of the same temperature and UV illumination program (Figure 2.3) as the AC for the sake of comparability, and taking the same factors into consideration. In every temperature step 10 minutes were measured before UV illumination, 10 minutes under and 10 minutes after illumination respectively. The timespan was chosen, so that it is comparable to one UV program step (5 cycles) in the AC measurement program, where the limiting factor was the measurement speed. (Recording a whole impedance spectra took around 3 min vs 0.1 s for a DC measurement point.)
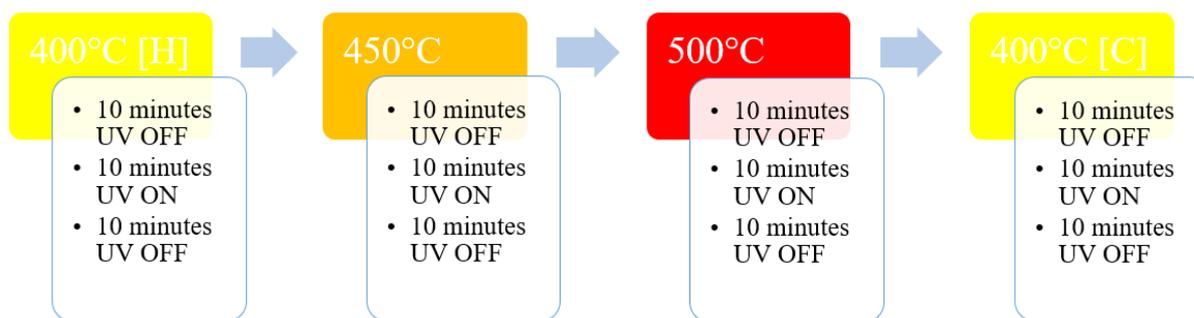
Figure 2.3 - DC measurement program

Slight changes were implemented later in the duration of each UV program step, as the different electrode materials and sizes showed different relaxation times, while the other parameters were kept unmodified. These will be discussed in detail during the results and discussion section.

3. Results and discussion

The aim of this thesis was to gain a better understanding of the nature of the changes, which take place in strontium titanate under UV irradiation. Therefore, systematic measurements were done, by changing only one parameter (e.g. temperature, UV irradiation, electrode material, electrode shape) at a time for the sake of comparison. On one hand the AC electrochemical measurements were performed to give an insight on the overall changes of electrical properties and the number of different processes under UV illumination. On the other hand, DC electrical measurements give us a superior time resolution, and show the photoconductivity as well as the lasting effect of ultraviolet light on STO.

3.1. Effect of electrode material and shape

In the framework of this master thesis three different electrode materials were used: platinum, lanthanum strontium cobaltite ($La_{0.6}Sr_{0.4}CoO_{3-\delta}$, LSC), and aluminum doped zinc oxide (AZO). The goal of the diversity was to be able to distinct the processes caused or affected by the electrode, from those derived purely from strontium titanate. While platinum is a metal with extremely good electron conducting properties (120 nΩ·m at 20 °C [148]), it has a very poor oxygen-ion conductivity[149]. Therefore, the oxygen exchange reaction can only happen on the triple phase boundary (Figure 3.1(a)). Contrary to platinum, LSC is a mixed ionic electronic

conductor (MIEC) (s. Section 1.5), which allows oxygen to be exchanged on the whole electrode surface (Figure 3.1 (b)).
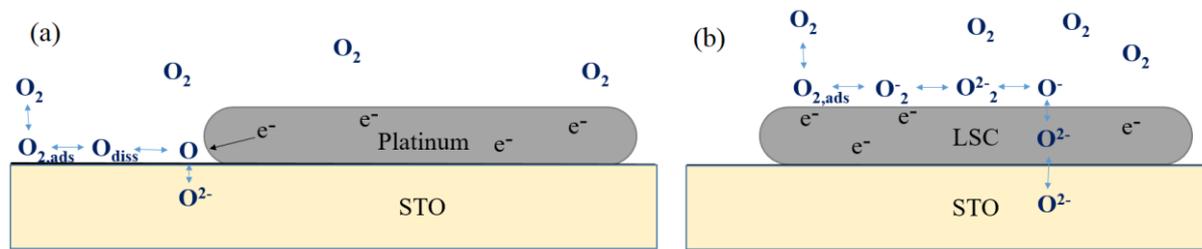
AZO has the unique combination of electrical conductivity and transparency[150]. As a consequence, the whole STO surface is able to react with the light. Unfortunately, the measurement with AZO electrodes showed, that under the measurement conditions (up to 500°C, UV-light) they were not stable and decomposed. As multiple samples showed the same behavior, AZO was only measured as a grid electrode and the results of those measurements could not be directly compared to those with LSC and platinum.

As it was described in section 2.1, the top electrodes were micro-structured into either a grid shape or to microelectrodes with different diameters, with the intention to gather information from different parts of the STO substrate. The grid current collector has the advantage of lower overall resistance, however at the same time covering 75% of the substrate surface, and hence the efficiency of the illumination is low. It also forms a plate capacitor with the counter electrode, therefore being able to probe the whole bulk of the substrate. The microelectrodes on the other hand have a much smaller surface area, which allows light to interact with strontium titanate on a larger relative area. Microelectrodes also have the advantage of probing a localized area of the substrate of about two times their diameter in depth [25].

3.2. Electrochemical impedance spectroscopy

Section 1.3.1. introduced the concept of fitting the impedance spectra with an equivalent circuit and through that quantitative information (e.g. resistance, capacitance) can be obtained. Each imperfect semicircle can be represented by a parallel R-CPE element, which are connected in

series. An example of a typical EIS spectrum and the fitted curve with the equivalent circuit is shown on Figure 3.2.
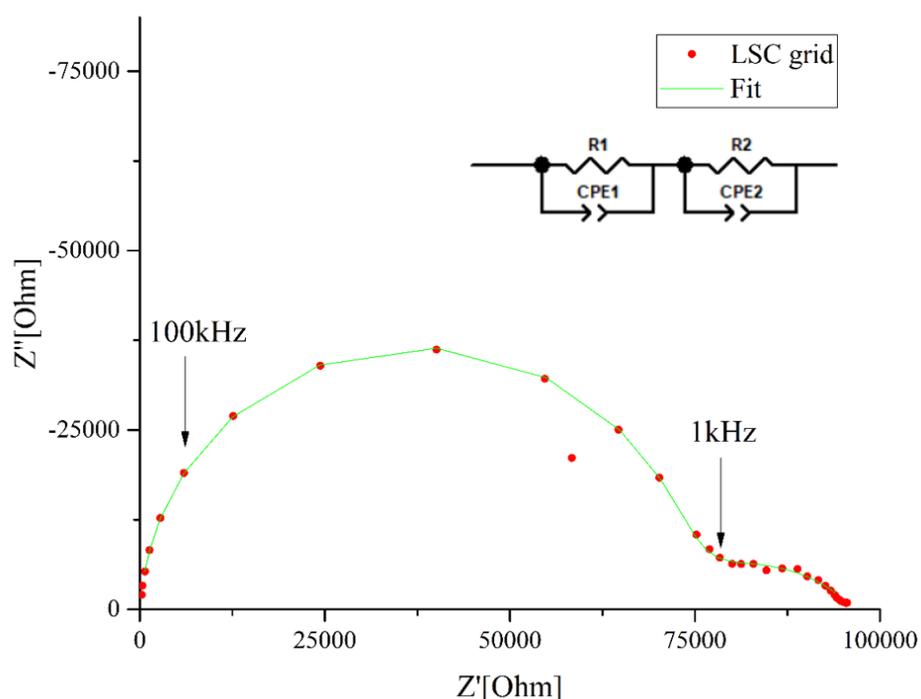

Figure 3.2 - An example of a typical impedance spectrum obtained from a sample with LSC grid electrode at 400°C in dark (red) and the fitted curve (green) using an equivalent circuit of two par(R-CPE) element

Figure 3.3 shows the impedance spectra of three different electrode materials with grid shape, while Figure X.X. two microelectrodes of different material. In the case of platinum two full semicircles are visible, with a third one starting, however most of it is outside of our standard measurement range. The high-frequency semicircle is significantly larger, and is closer to a perfect semicircle, than the middle one, which is slightly distorted. On the EIS spectrum of the AZO electrode three semicircles can be observed as well. However, the high-frequency semicircle is only realized as a shoulder on the left side of the mid-frequency semicircle, which made the precise fitting difficult. Contrary to the other two electrode materials, in this case the low-frequency semicircle is the largest, however the lower frequency part is incomplete and suggests a shoulder on the right side, outside of the chosen basic measurement range. The impedance spectrum of the sample with LSC grid electrode has a similar course as the one with platinum electrode, however the low-frequency semicircle is clearly missing in this case.
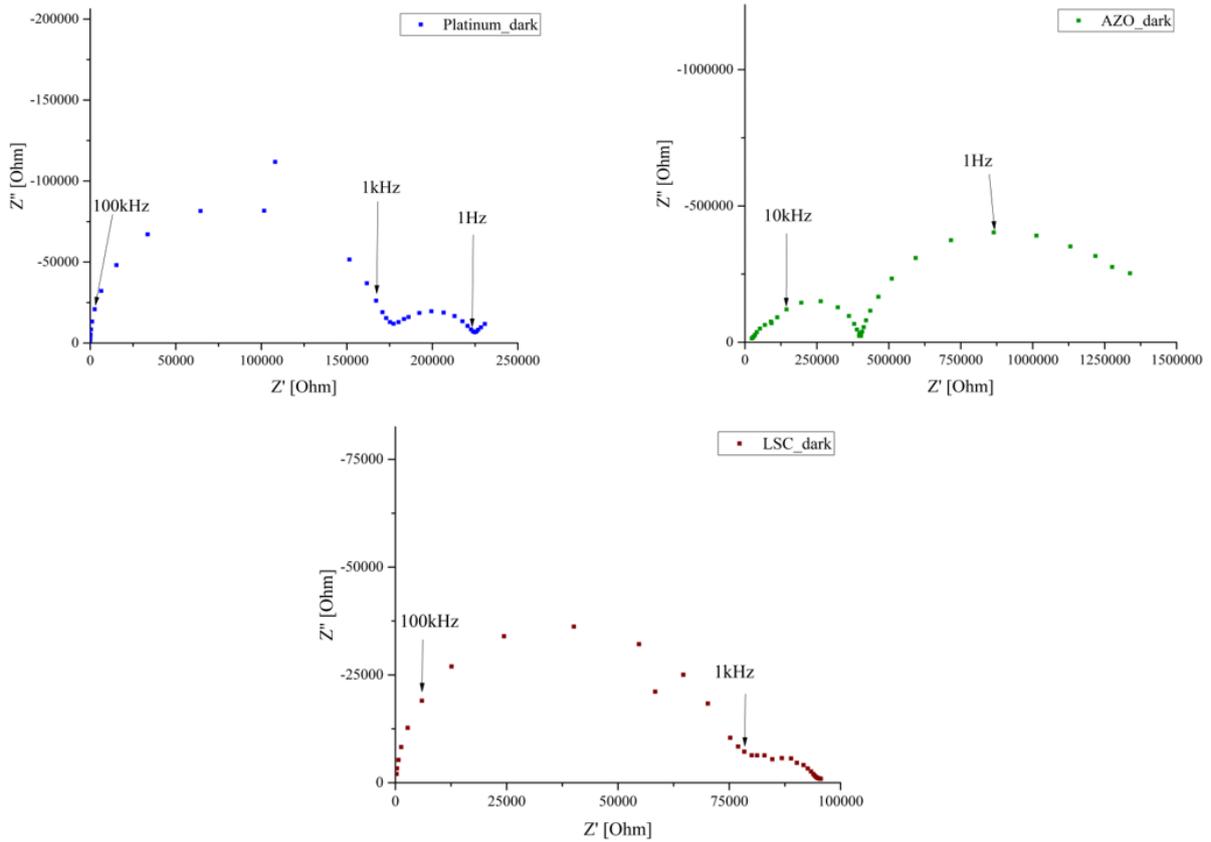
Figure 3.3 - EIS spectra of three STO with three different electrode (grid) material at 400°C
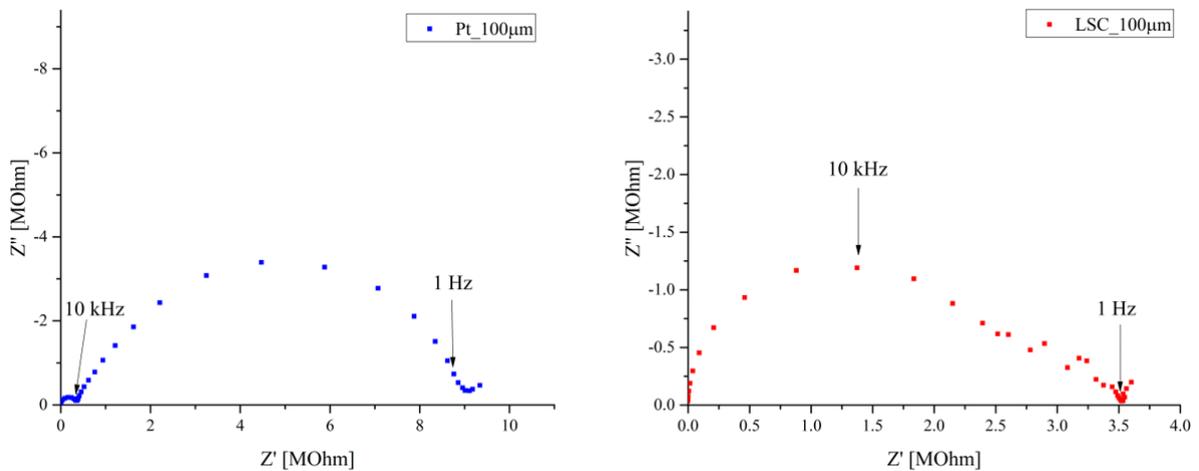

Figure 3.4 - EIS spectra of two STO samples with two different microelectrode material at 400 °C

The effect of UV illumination is significant in all three cases, see Figure 3.5, Figure 3.6 and Figure 3.7. The EIS spectrum of the sample with platinum grid electrode shows a change in the size relation of the high- and mid-frequency semicircle. The illumination has a larger effect on the high-frequency semicircle, as it gets even smaller than the mid-frequency. The third

semicircle either shifts to even smaller frequencies, as a slight hint might be visible at the end of the second semicircle, or it disappears completely, and the small feature on the right side is solely the ongoing change due to the illumination. The EIS spectrum of the sample with LSC grid electrode shows a proportional change in illuminated condition, only the absolute value decreases significantly, while the overall shape does not change notably. The case of the AZO grid electrode is tough to evaluate. The whole spectrum displays the most substantial change, with an order of magnitude contraction. The ascending side of the earlier mid-frequency semicircle lies outside of the measurement region, which means that the left shoulder and the earlier high-frequency hemicycle is not visible. The in dark largest low-frequency semicircle is notably distorted, while there seems to be a fourth feature, which is however too noisy for evaluation.
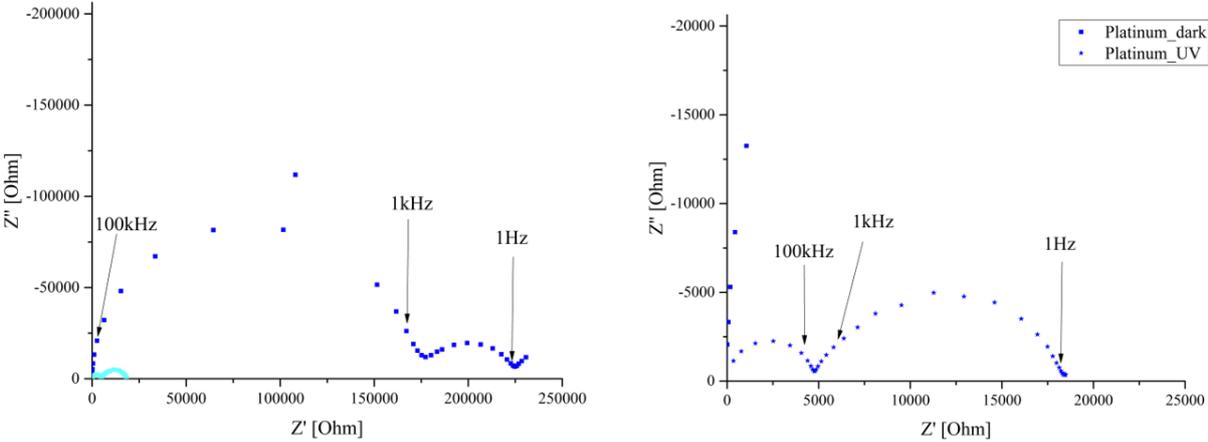

Figure 3.5 - EIS spectra of a sample with platinum grid electrode at 400°C in dark (left) and under UV illumination (right)
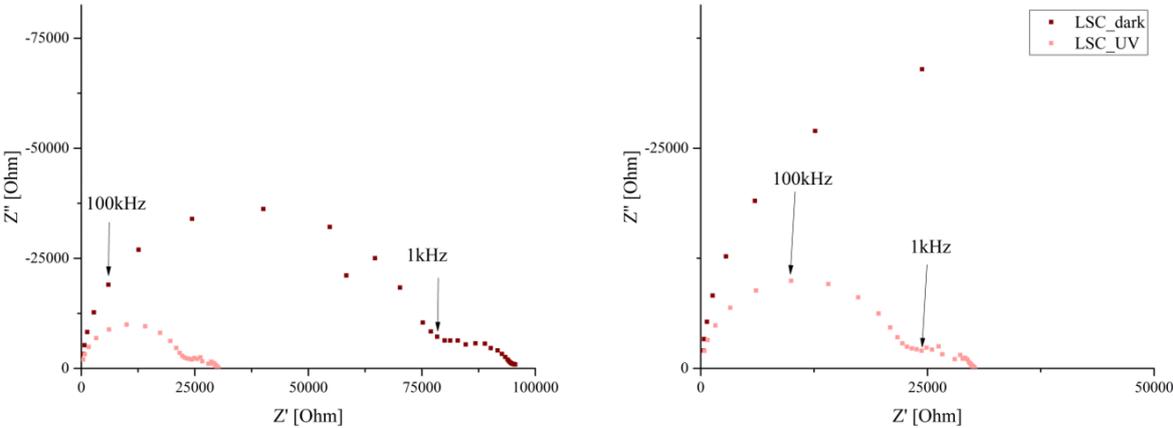

Figure 3.6 - EIS spectra of a sample with LSC grid electrode at 400°C in dark (left) and under UV illumination (right)
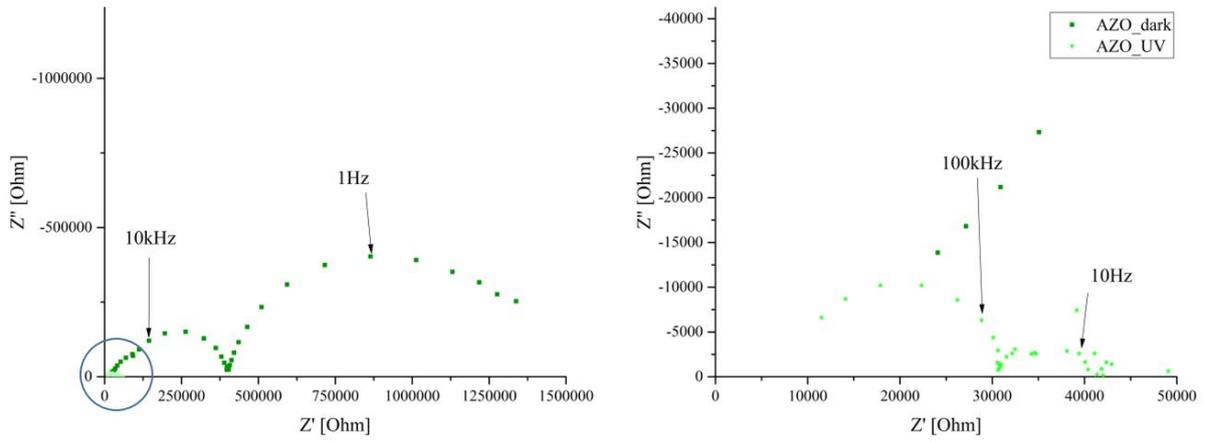
Figure 3.7 - EIS spectra of a sample with AZO grid electrode at 400°C in dark (left) and under UV illumination (right)

Assuming that each of these semicircles represent a separate electrochemical process in the sample, the next sections will investigate the behavior of these under different experimental conditions and by looking at the tendencies will make an attempt to deduct the nature of the given process.

3.2.1. Investigation of the high-frequency semicircle

Comparison of the fitted resistance and capacitance values between different samples are not possible, due to the extensive nature of these values. Therefore, a size independent property was necessary to be found. Earlier results of Walch[89] suggested, that the first arc is caused by the bulk of strontium titanate. This assumption is also supported by the nearly perfect shape of the semicircle. Size independent measure of the resistance in the case of a bulk matter is the resistivity. In the case of a grid electrode, current flow is uniform, thus the resistivity can be calculated by the general equation:

$$\rho_{grid} = R * \frac{A}{l} \tag{33}$$

where l is the thickness of the STO substrate (500 μm) and A is the surface area, which was calculated with the help of microscope images. In the case of the microelectrodes, resistivity can be calculated from the equation of the spreading resistance, introduced in section 1.3.1.:

35

$$\rho_{microelectrode} = 2Rd_{me} \tag{34}$$

where d_{me} is the diameter of the microelectrode.

If the high-frequency semicircle is caused by the strontium titanate bulk, then in the case of the grid top electrode, the capacitance is caused by the parallel plate capacitor, formed by the top and bottom electrodes, with the STO as dielectric in between. As a size independent measure, the relative permittivity can be calculated from the equation of the parallel plate capacitor:

$$C = \frac{\varepsilon\varepsilon_0 * A}{d} \tag{35}$$

where ε is the relative permittivity, ε_0 is the vacuum permittivity, A and d are analogous to Equation (33). In the case of microelectrodes, an analogous method can be used to calculate the capacitance as for the spreading resistance:

$$C = \frac{2d_{me}}{\varepsilon\varepsilon_0} \tag{36}$$

In the following presentation of the EIS results, on the X axis the so-called *cycles* will be plotted, which were introduced in section 2.3. This represents on one hand a rough time scale, as one cycle lasted approximately 3 minutes, on the other hand indicates the UV program as well, as five cycles were measured before, five during, and five after illumination of the sample with ultraviolet light. On the Y axis, the calculated properties (rel. permittivity, resistivity) are plotted.

Starting with the calculated resistivity values of the high-frequency semicircle, in Figure 3.8 the three different electrode materials are compared at 400°C.
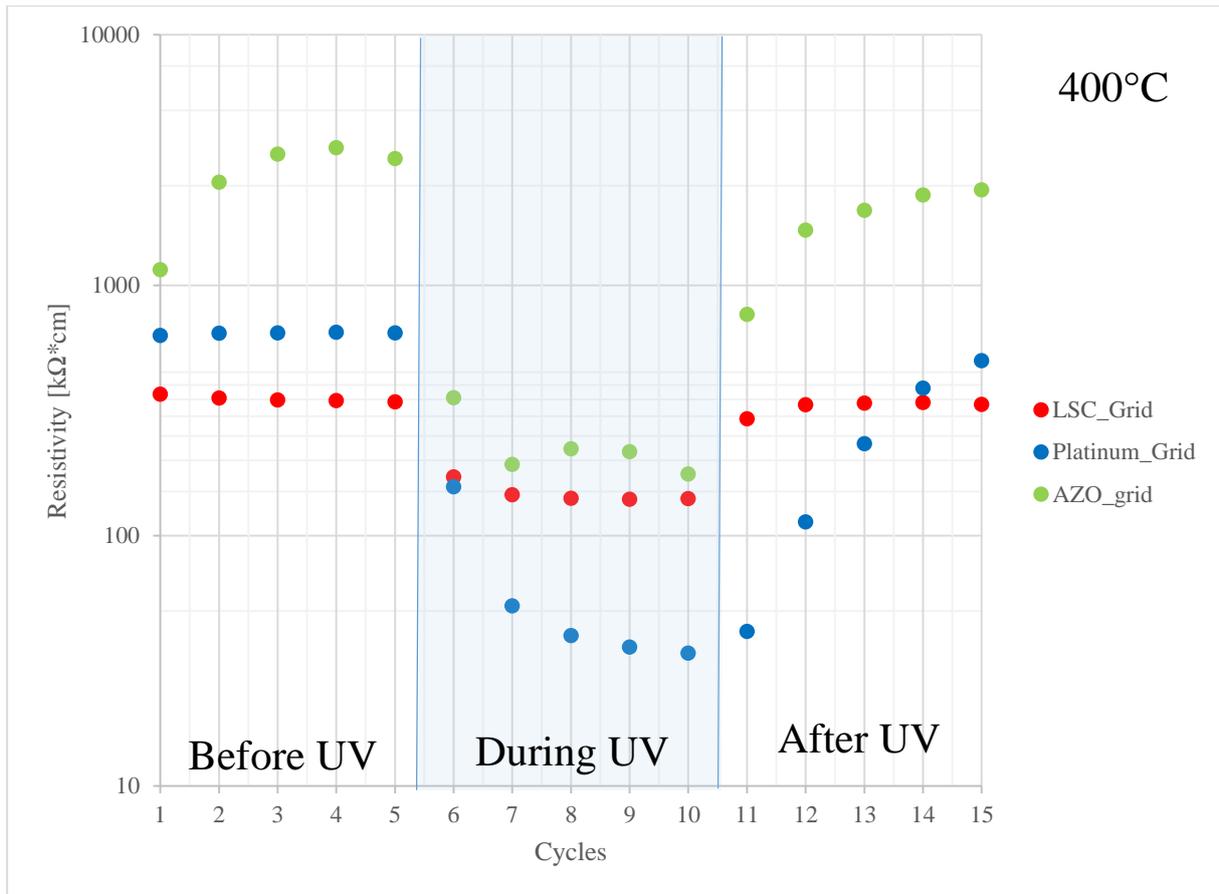
Figure 3.8 - Resistivity of the high-frequency semicircle with three different grid shaped electrode materials at 400°C

The dark values are relatively close to each other in the case of all three samples, however the one with AZO grid electrode gradually increases over time. Regardless of the electrode material, the resistivity decreases significantly under UV illumination. The change is about an order of magnitude in the case of AZO and platinum, and a factor of four with LSC electrode. Although the temporal resolution is poor, the difference in the rate of relaxation after UV is clearly visible. The sample with LSC electrode completely relaxes to the original dark value in about 6 minutes (end of second measurement cycle), while the other two samples require more than 15 minutes. The first assumption that comes to mind is photoconductivity. The photogenerated free charge carriers increase the conductivity significantly, however this effect is most pronounced in the top few micrometers of the sample, and in order to cause significant change throughout the sample, the mean free path of electronic charge carriers must be assumed to be long. Additionally, photoconductivity is characterized by a quick jump not only when UV is turned on, but also as illumination is turned off, as the additional free charge carriers quickly recombine. In the case of platinum and AZO grid electrode, this quick jump is clearly absent, while for LSC electrode it cannot be determined, due to the bad temporal resolution.

37

Furthermore, photoconductivity is independent from the electrode material, while the results show, that equilibration times and extent of the effect are both influenced. Merkle[88] reported, and Walch[89] supported the idea, that oxygen incorporation kinetics are enhanced by UV illumination. This could well explain both the difference in extent and equilibration times. Oxygen incorporation is significantly slower than photoconductivity, while it also generates electron holes, increasing hole conductivity:

$$\frac{1}{2}O_2 + V_{\ddot{O}} \rightleftharpoons 2h^{\cdot} \tag{37}$$

In dark at 400 °C the oxygen exchange kinetics are limited by the surface reaction, that means an evenly distributed decrease in oxygen vacancy concentration, and a homogeneous increase of hole concentration. Under UV illumination the oxygen incorporation on STO is accelerated and the rate limiting step is less obvious. The electrode material also affects the oxygen exchange reaction depending on its oxygen ion conductivity. The difference between reaction paths are explained in detail in section 3.1. A MIEC electrode, like LSC, accelerates the reaction in both ways, as the whole electrode surface is active. Contrary in the case of electrodes with bad ionic conductivity (Pt, AZO) only the triple phase boundary is active, and the surface below the electrode is blocked from oxygen exchange. This could explain the difference not only in equilibration time after UV, but also the difference in the magnitude of the photo-effect. As oxygen is incorporated into the STO lattice under UV illumination, the decreased concentration of oxygen vacancies pushes the equilibrium reaction to the direction of oxygen excorporation. This is significantly faster with LSC grid electrode, therefore less oxygen can incorporate, which results in a lower overall photo-effect. On the other hand, in order to compensate the enhanced incorporation reaction, platinum and AZO need a significantly lower oxygen vacancy concentration, which results in higher hole concentration, and thus a larger UV effect. The reason for the faster response under UV illumination with LSC is not obvious however.

Temperature dependence of the resistivity with different electrode materials is shown in Figure 3.9. While the samples with LSC and platinum both show a clear decreasing trend with similar slopes, no such tendency can be determined for the one with AZO grid.
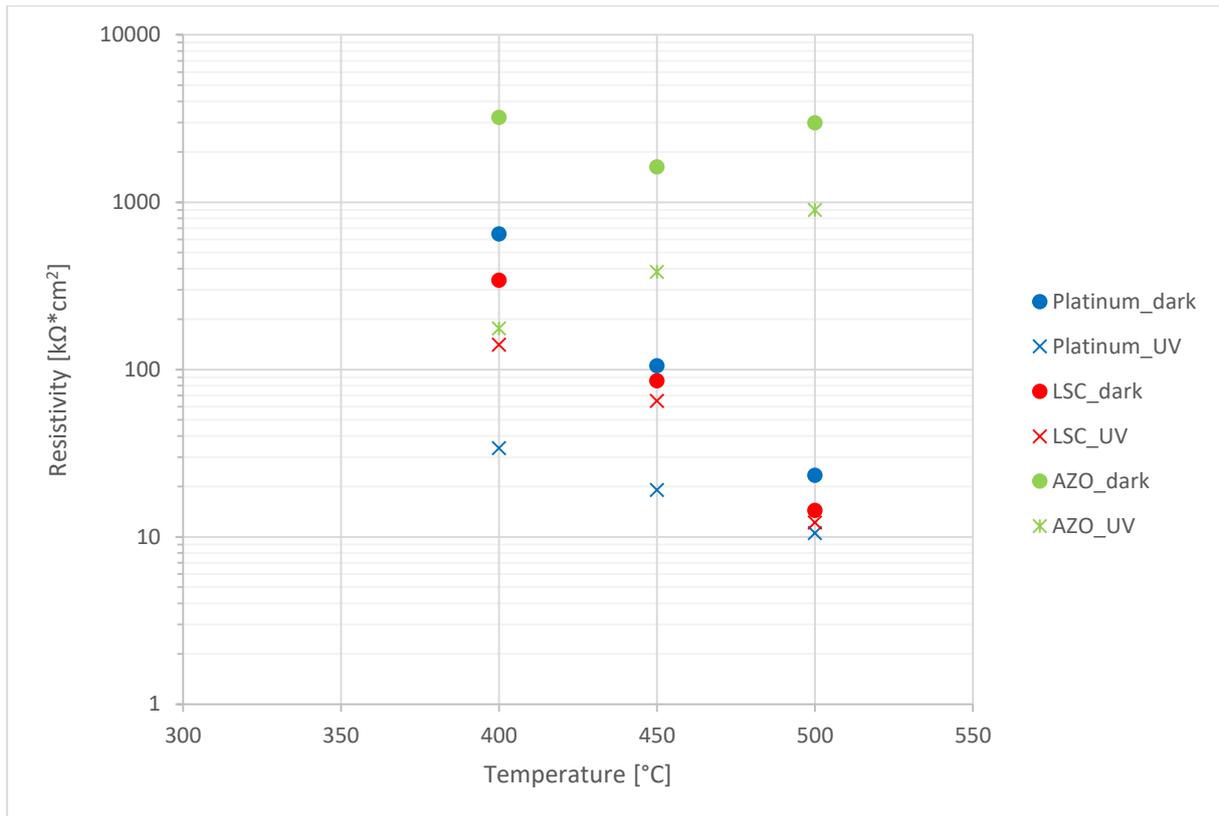
Figure 3.9 - Temperature dependence of the calculated resistivity of the high-frequency semicircle with different grid electrodes

The UV illumination caused increase of the conductivity diminishes with increasing temperature. This might be attributed to the fact that the illumination and heating has a similar effect on the conductivity of the sample, as photoexcitation and thermal activation both increase the number of free charge carriers. There are still two orders of magnitude difference between the thermal excitation energy (at 500°C kT = 75 meV) and the photon excitation energy (ca. 3eV), which leaves plenty of room for further free charge carrier generation. However, recombination depends on temperature and the effect of temperature dependent defect concentrations on the surface reactions might play a role as well.

Resistivity is preferred instead of the directly fitted resistance, as it should be size independent. Figure 3.10. shows calculated values for different sized LSC and platinum microelectrodes. Unfortunately, the impedance spectra of the sample with AZO microelectrodes were inconsistent and couldn't be evaluated meaningfully. The initial dark values show discrepancy, partially due to the clearly not equilibrated start-state from earlier illumination or temperature cycles. Under UV illumination however, the resistivity drops to very similar values in not only the case of all three different sizes of microelectrodes, but also for both samples with different

electrode materials. Slight differences can be observed in the relaxation speed after the UV light was turned off, however, this effect does not scale clearly with the electrode size. The LSC microelectrodes show a slightly faster relaxation compared to platinum, although these rates are significantly slower than those seen by the samples with grid electrodes, possibly because the electrode surface is significantly smaller. The smaller surface however also ensures a longer relaxation time, and thus makes it visible, that the equilibrium is reached significantly faster under UV compared to relaxation after UV. This observation also fits into the proposed idea, that the increased conductivity is caused by the *via* UV enhanced oxygen incorporation.
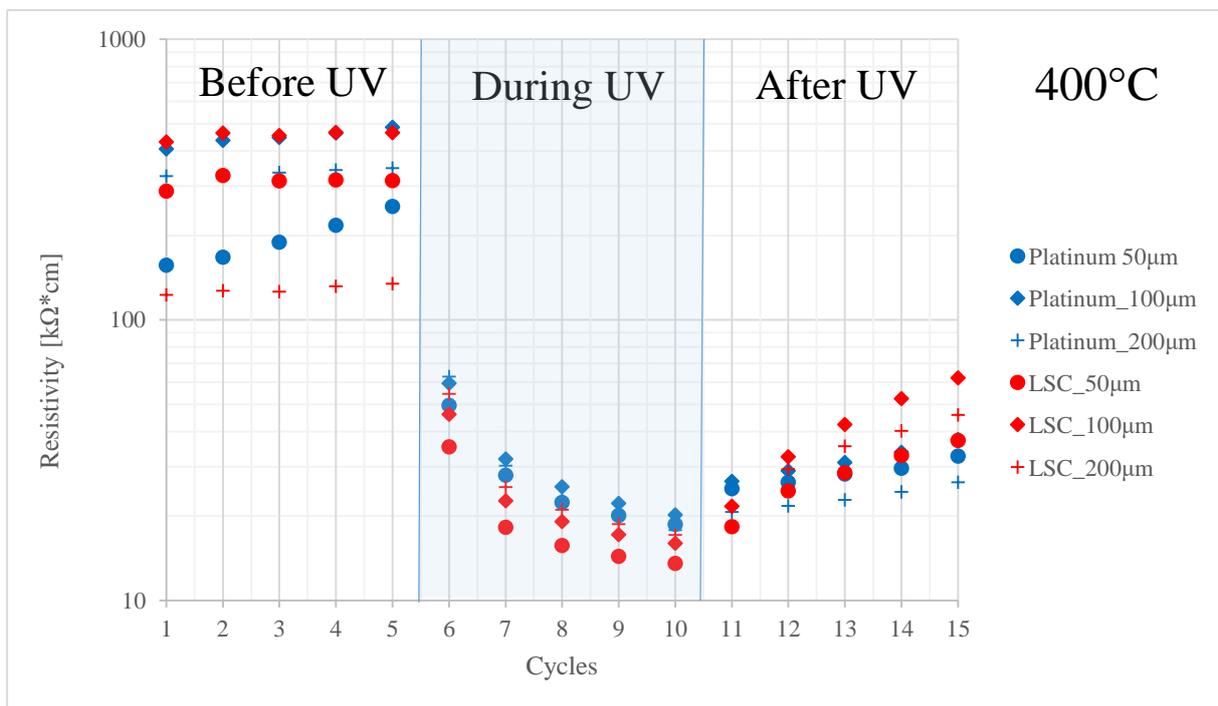

Figure 3.10 - Resistivity values of the high-frequency semicircle for samples with microelectrodes of different sizes and materials

It is worth mentioning, that all five samples with different electrode shapes and materials react very similarly to UV illumination. This underpins the assumption that the high-frequency arc is caused by the STO bulk, which is the same in the two samples.

The relative permittivity values were calculated from the fitted capacitance results. In Figure 3.11. the effect of UV illumination is shown for samples with different electrode materials at 400 °C. The values with LSC and platinum grid electrodes are very close to each other and react similarly to UV light, while for AZO it is hard to determine, as the sample was seemingly not in equilibrium before the illumination. Nevertheless, from the increasing tendency of the dark

measurement points, a similarly close value can be deducted as for the other two samples. In all three cases the permittivity drops significantly under UV irradiation, by a factor two for LSC grid, by around 30% with platinum current collector, and around 60% with AZO grid.
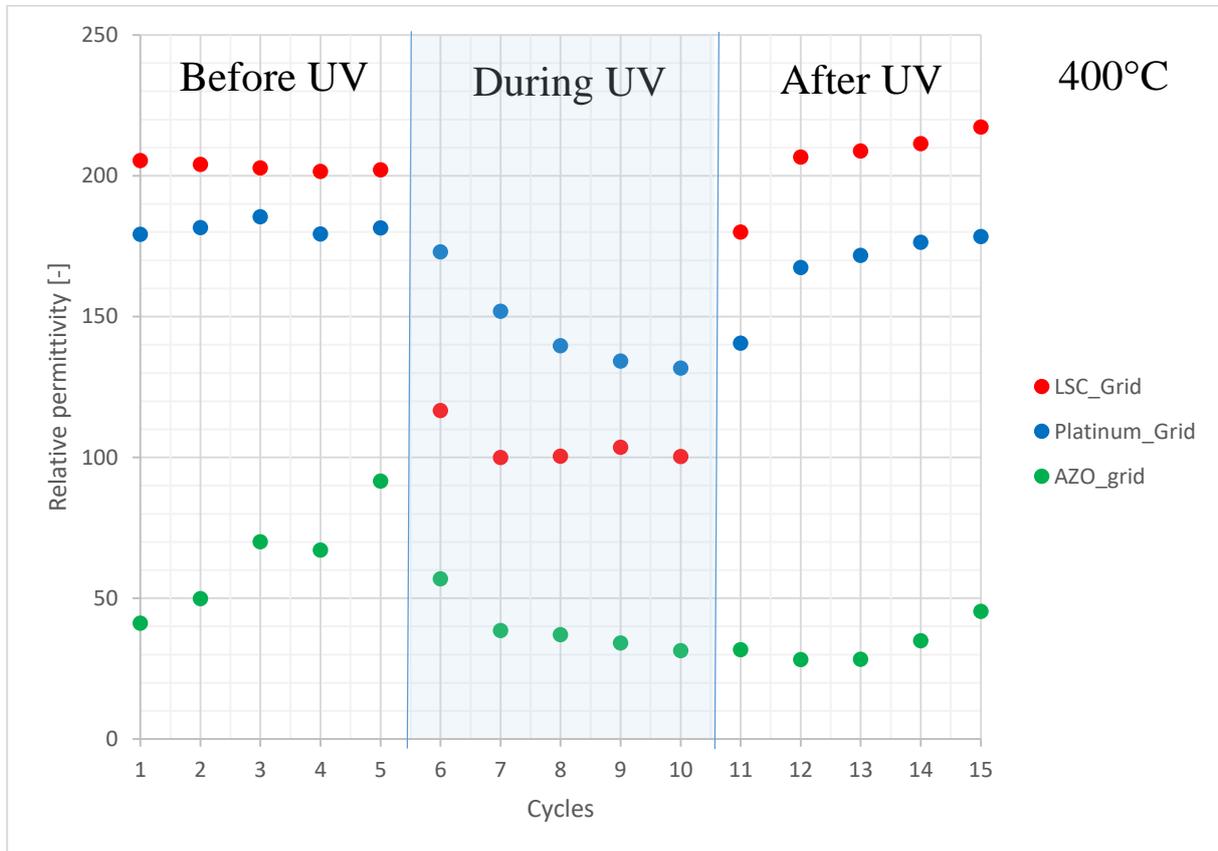

Figure 3.11 - Effect of UV irradiation on the relative permittivity of the high-frequency semicircle for samples with three different electrode materials

However, the temperature program consisted of two steps at 400 °C, one at the beginning and one at the end, explained in detail in section 2.3. An unusual behavior was observed in the case of the sample with LSC grid electrode, shown in Figure 3.12. The above described UV effect completely disappears in the cool down step. Speculation is quite difficult about the possible reasons based solely on these results, however the most probable scenario, is that a non-equilibrium state was frozen-in during the sample preparation up to 400 °C, and could only reach thermodynamic equilibrium at around 500 °C. As an example, multiple studies concluded, that argon-ion bombardment creates a defect rich surface layer[86, 151, 152], or even the pulsed laser deposition can reportedly reduce the substrate[65, 153]. In the literature one can find multiple observations and quantum mechanical calculations about the clustering of different combinations of point defects. For instance, Cordero[72] describes in his work a

linear chain-like clustering of oxygen vacancies, which has far-reaching effects on the conductive properties of strontium titanate, although much higher temperature is necessary to reach thermodynamic equilibrium.
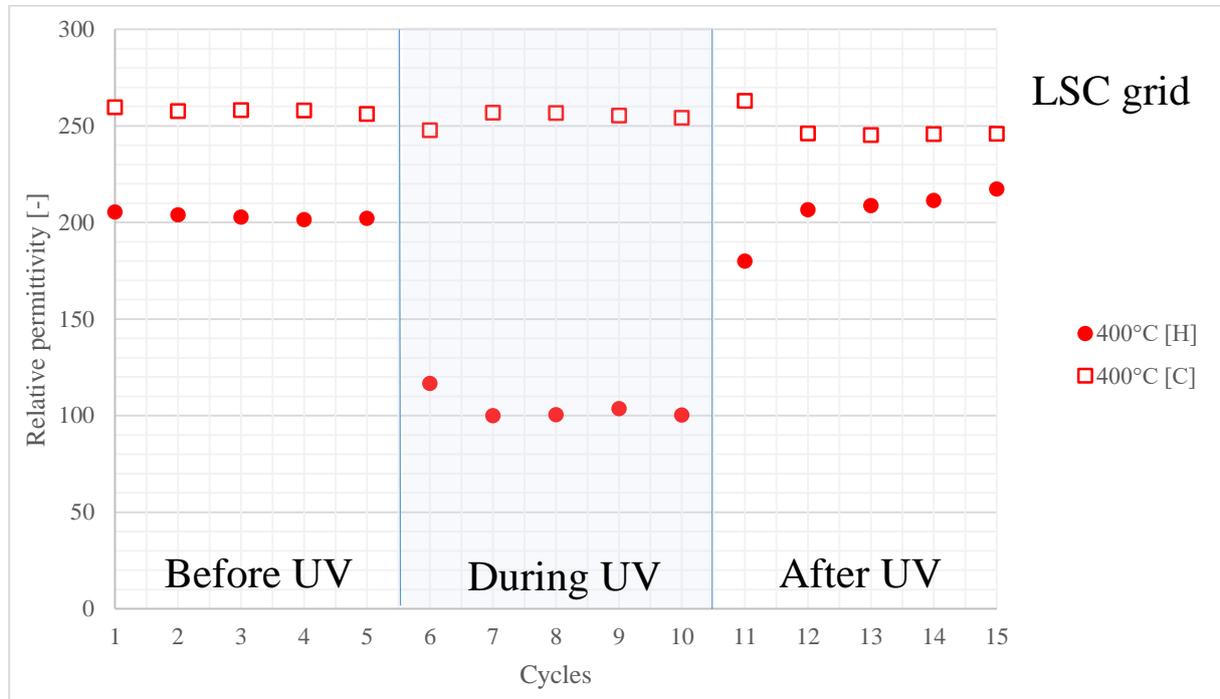

Figure 3.12 - Effect of UV illumination on the relative permittivity values of the high-frequency semicircle with LSC grid electrode at 400°C heatup [H], and cooldown [C] step

Investigation and complete understanding of this effect is beyond the limits of this thesis, nevertheless the platinum grid sample was re-measured as well (Figure 3.13). The results show, that contrary to LSC, the sample with platinum grid electrode does not change after the first heat up, as the values of the "cool down" step of that measurement overlap with that. However, after several further electrical measurements at elevated temperatures, the re-measured values show a similar tendency. Instead of a significant decrease, UV irradiation causes a slight increase in the permittivity, which gradually decreases over time. Contrary to LSC, in this case the dark value did not change.
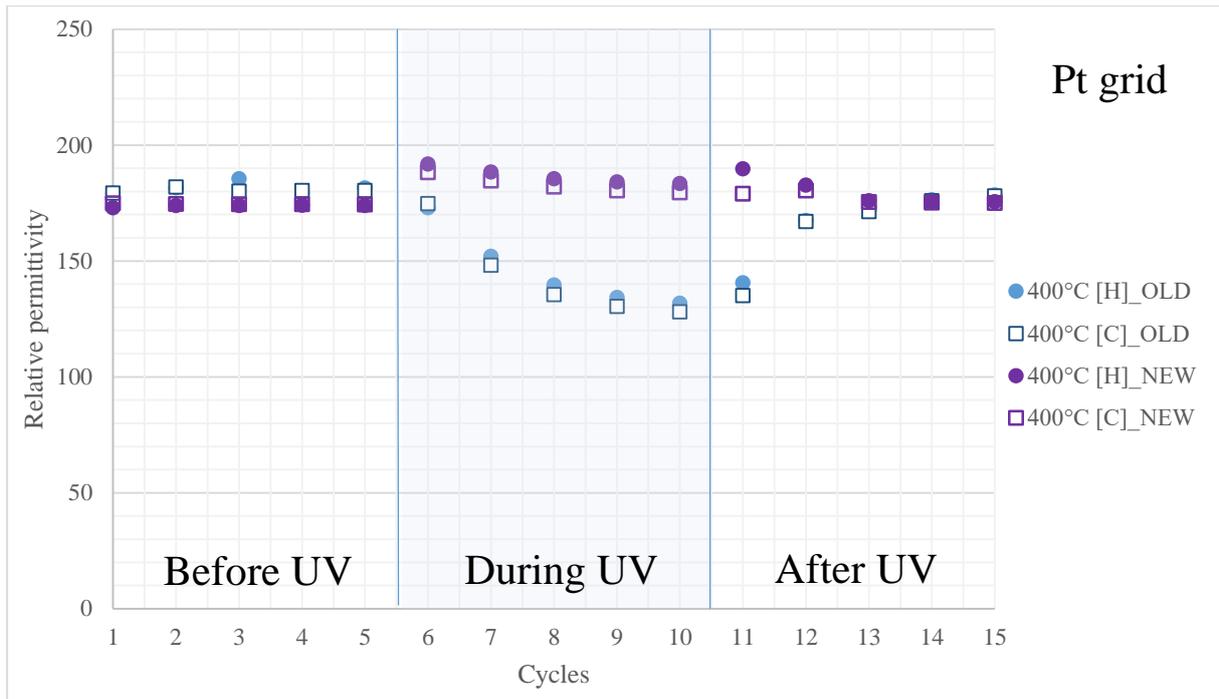
Figure 3.13 - Comparison of the calculated relative permittivity of the high-frequency semicircle of a sample with platinum grid electrode, measured direct after sample preparation (OLD), and again after several further measurements (NEW)

The sample with LSC grid electrode was measured again as well, in order to check further potential changes (Figure 3.14). The results clearly show, that no further change occurred during the several other measurements or due to the time spent at elevated temperatures.
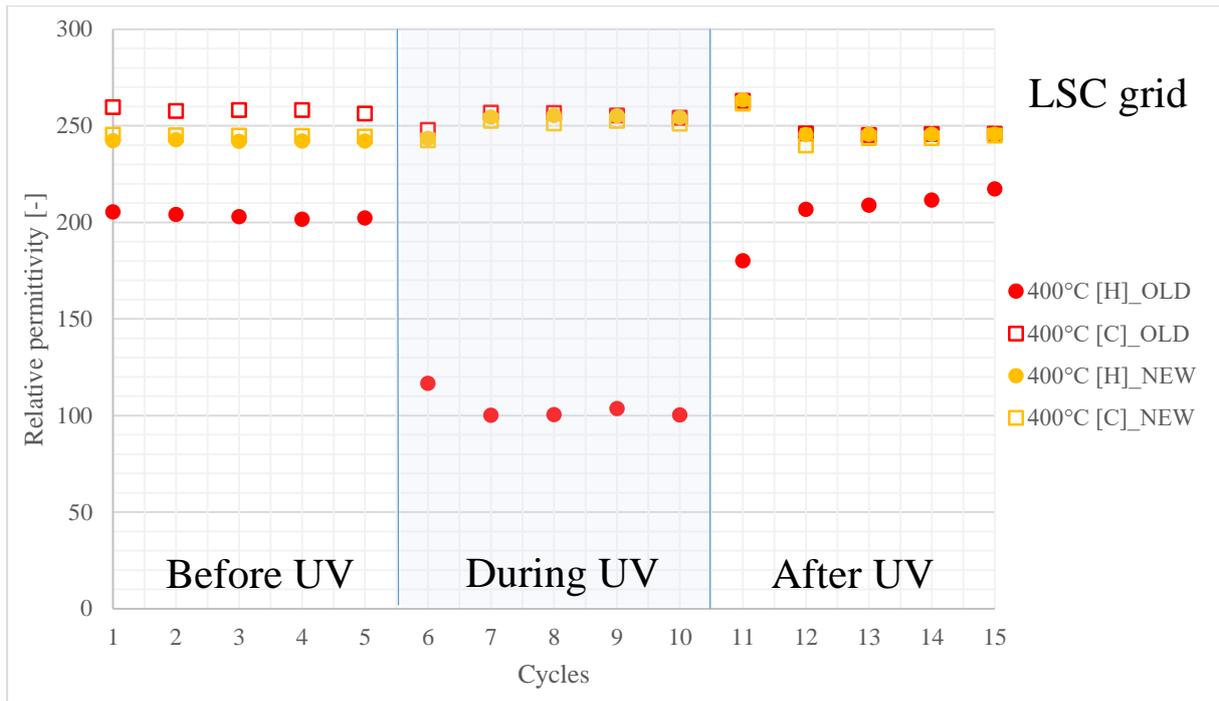
Figure 3.14 - Comparison of the calculated relative permittivity of the high-frequency semicircle of a sample with LSC grid electrode, measured directly after sample preparation (OLD), and again after several further measurements (NEW)

Contrary to the relative permittivity, the general UV effect on the resistivity is unchanged (Figure 3.15), however slight discrepancies can be observed. The conductivity increases more significantly for both platinum and LSC under UV irradiation, however the dark values got slightly lower for LSC and somewhat higher for platinum electrode. Relaxation after UV illumination got slower with platinum grid electrode, whereas with LSC no detectable change can be realized. The underlying reason is unkown at the moment.
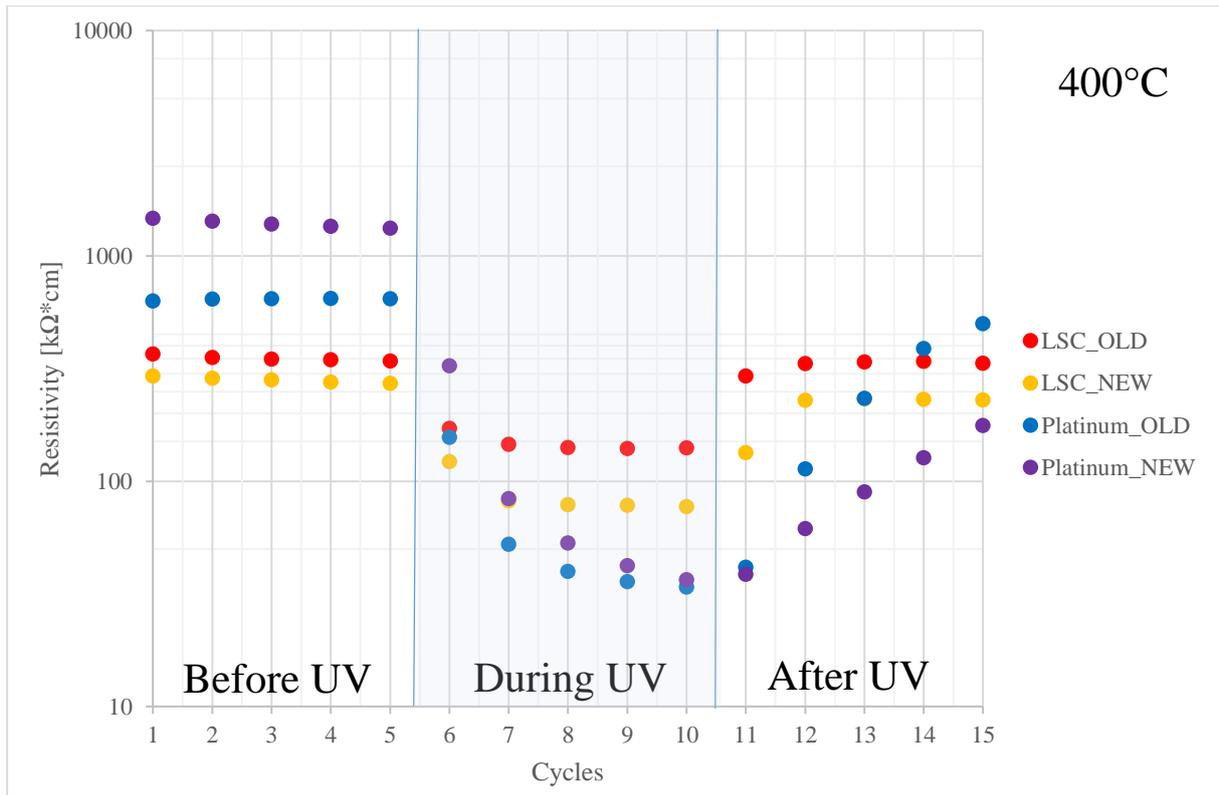
Figure 3.15 - Comparison of the resistivity of the high-frequency semicircle for samples with two different electrode materials, measured directly after sample preparation (OLD), and again after several further measurements (NEW)

Repeated EIS spectra of the sample with AZO electrode could not be obtained, as the results showed that under the measurement conditions (up to 500 °C, UV-light) they were not stable or decomposed over time. Due to this reason, and due to additional difficulties in the sample preparation of the micorelectrode sample, AZO is excluded from the rest of the discussion.

As the later repeated measurement results probably include the thermodynamic equilibrium state, in the following sections those will be used.

Temperature dependence of the relative permittivity of the grid samples together with the UV effect is shown in Figure 3.16. A clear tendency is difficult to deduct from three points, but we can state that the permittivity decreases with increasing temperature, which fits well with the idea that the high-frequency semicircle stems from the strontium titanate substrate. Furthermore, the measured values are in the same order of magnitude as the literature value of STO (300 on 25 °C). However, directly measured relative permittivity value is difficult to find. As an estimation we can use the work of Linz, who successfully applied the Curie-Weiss law for the low temperature region[52]:

$$\varepsilon = \frac{C}{T-\theta} = \frac{8.5 * 10^4}{T - 17K} \tag{38}$$

where C is a constant, and θ is the Curie-temperature. According to Barrett[53] this estimation is well applicable for the high-temperature region too. A comparison of the estimated relative permittivity values and the measured ones are shown in Figure 3.16 as well.
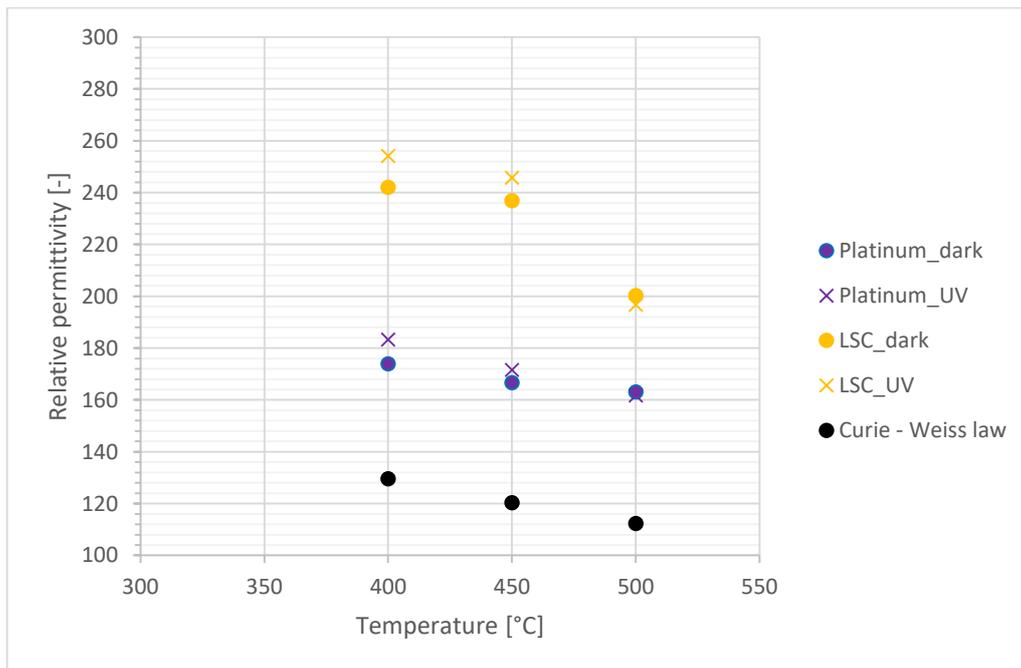

Figure 3.16 - Temperature dependence of the calculated relative permittivity values for the high-frequency semicircle of samples with grid electrodes

For 400 °C the relative permittivity is expected to be around 130. Although the values for either electrode materials are both higher, the slope is close to that based on the Curie-Weiss law. One however have to be cautious, when comparing relative permittivity values measured by others, as the value depends on how relative permittivity is defined in the given research. In most cases it is taken at 1 kHz, while in the case of impedance spectroscopy, the value is fitted to the peak frequency of the semicircle, which is one to two orders of magnitude higher. Although according to the measurements of Linz[52], at room temperature the relative permittivity of STO is independent from the frequency in a large range, it is possible, that the situation is different at elevated temperatures.

A temperature dependent element of the UV effect can be observed as well, as the change turns sign on 500 °C for both sample.

Relative permittivity, just like resistivity should be independent from electrode or sample size. Nonetheless, measurement of microelectrodes with different diameters show a clear decreasing tendency with increasing electrode size.
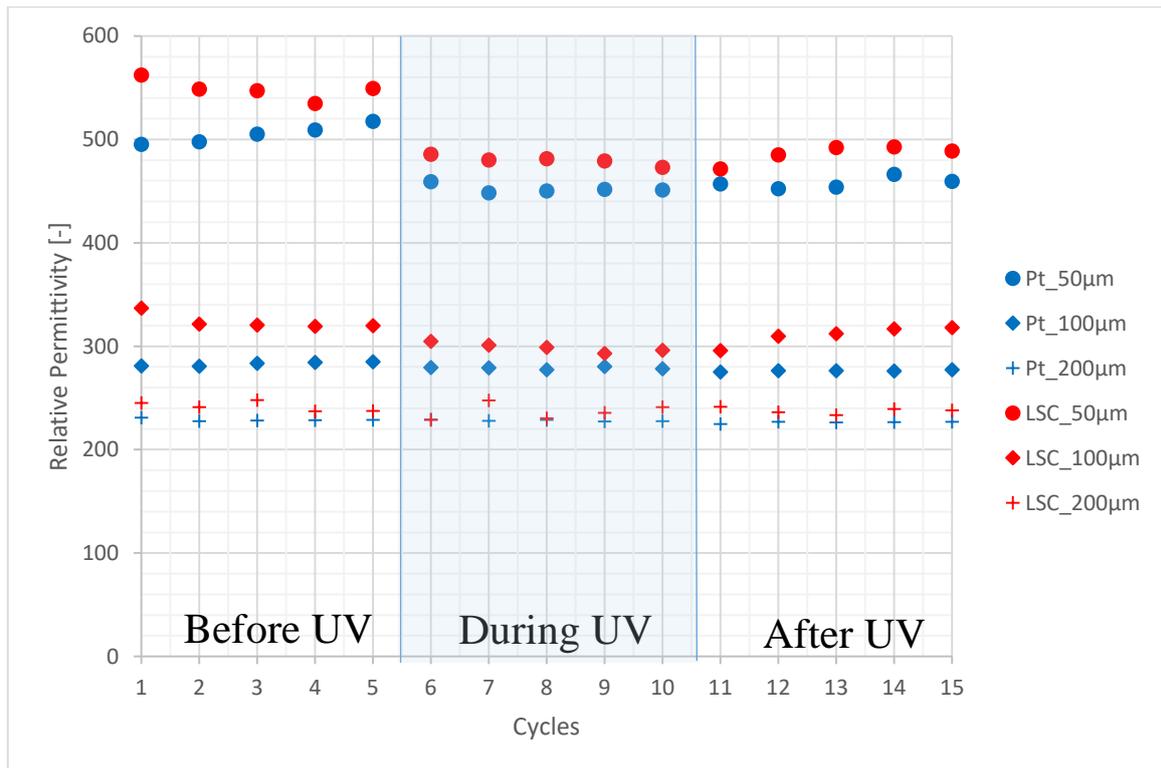

Figure 3.17 - Relative permittivity values of the high-frequency semicircle for microelectrodes with different diameters and materials on STO substrate

Despite the fact that the substrate was the same under all three microelectrodes, the difference in the relative permittivity values are significant. A possible reason is that the permittivity might be inhomogeneous throughout the bulk, and as the different microelectrode sizes probe a different amount of the substrate volume, the apparent relative permittivity shows a disparity. The largest deviation from the grid values are shown by the smallest microelectrodes, which are probing closest to the surface. The 200 μm microelectrodes, probing almost the whole 500 μm thickness of the STO single crystal are very close to the values of the grid sample. One option to be considered is thermal inhomogeneity in the cross-section of the substrate. The reason behind lies in the measurement setup itself. The sample is only heated from below and

the platinum needle, which used to contact the top electrode has excellent heat conducting properties. This could lead to a significant heat withdrawal from the surrounding area of the microelectrode[154]. Furthermore, the smaller electrodes are more prone to this effect due to their smaller surface. As we have seen earlier the permittivity is higher on lower temperatures, which is exactly the tendency seen in Figure 3.16.

Looking at the two different electrode materials, the above described apparent size dependency is exactly the same for the two different samples. This further supports the idea, that the high-frequency semicircle stems from the substrate, and is not affected by the material of the electrode.

The change upon UV illumination depends on the size of the electrode as well. In the case of microelectrodes, a decrease in permittivity can be observed, which diminishes with increasing microelectrode size. This might be explained if the circumference to area ratios are taken into account. Both electrodes block the UV light, which means that photo effect in the substrate can only occur on the bare STO surface. Each microelectrode can only probe a limited surface area around it, restricted by the sheet resistance. Although the extent of the measured periphery is difficult even to estimate, we can clearly determine, that if a constant "extended radius" is assumed, then the bare to blocked surface ratio is smallest in the case of the largest, 200 μm electrode, larger in the case of the 50 μm electrode, and largest for the grid electrode, which is in good agreement with the results.

In order to achieve a deeper understanding of the underlying process of the high-frequency semicircle, the samples with grid electrodes were measured at two additional temperatures (300 °C, 600 °C). The Arrhenius plot of samples with grid electrodes is shown in Figure 3.18.
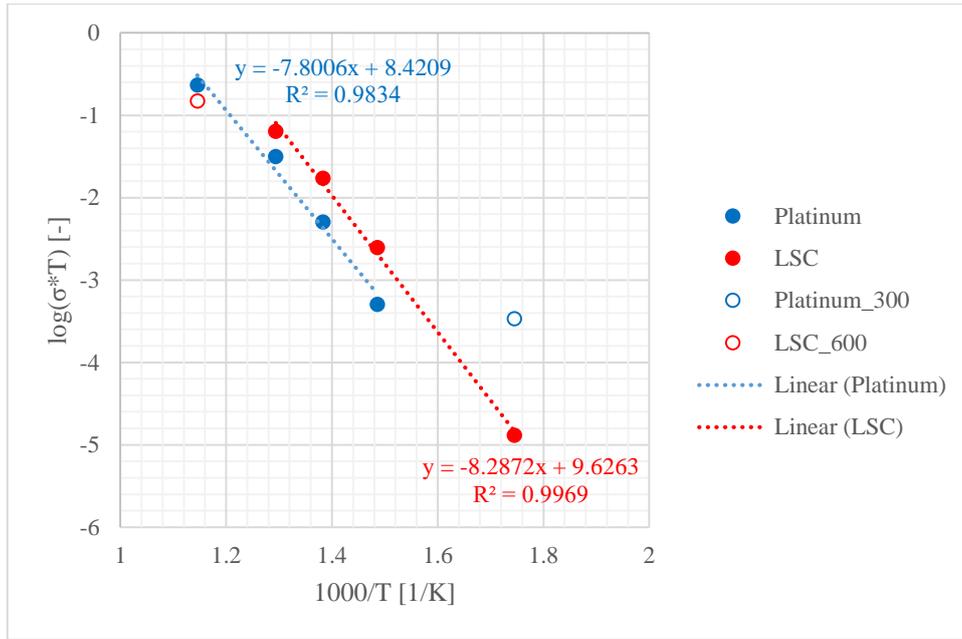
Figure 3.18 – Arrhenius plot for STO samples with grid electrodes

The Arrhenius equation in this form is:

$$\ln(\sigma * T) = \ln(A) - \frac{E_a}{k_B} * \frac{1000}{T} \tag{39}$$

Where A is the pre-exponential constant, E_a is the activation energy and k_B is the Boltzmann-constant ($8.61*10^{-5}$ eV/K). The activation energy can obtained by dividing the slope in equation (39) by k_B. The obtained activation energies are 1.55 and 1.64 eV for samples with platinum and LSC grid electrode respectively. These numbers fit into the general range found for ionic and hole conductivity, which is between 0.9-1.8 eV[3, 49, 62, 73, 77, 155]. It is important to note, that two points were left out from the fitting: The sample with LSC grid electrode at 600 °C, and the one with platinum grid electrode at 300 °C. Fitting a line with two points does not bring meaningful results, however the shift of slope could indicate a shift between ionic and electronic conduction.

Summarizing the results of the high-frequency semicircle, a significant light effect was measurable *via* an increased conductivity and a slightly varied permittivity, which however decreased or even diminished at elevated temperature. An apparent size dependency in both properties could be the result of a temperature gradient due to the one-sided heating. Generally,

the resistivity as well as the relative permittivity values were in close proximity for both electrode materials, and showed a similar apparent size dependency in case of the relative permittivity. Furthermore, the measured relative permittivity is in the same range as the estimated literature value of strontium titanate. Moreover, calculated activation energies were in the range literature data of the bulk. Subsequently the changes of both properties under the measured conditions could be adequately explained by assuming changes in the STO substrate. These arguments strongly support the assumption, that the high-frequency semicircle is caused by the strontium titanate bulk.

3.2.2. Investigation of the mid-frequency semicircle

Fitting of the mid-frequency semicircle with an equivalent circuit was more challenging, as the measurement of one point in the lower frequency region takes more time, which means significant distortion in the shape of the semicircle due to the change during and after UV illumination. This also means that the first measurement point during UV illumination (6. Cycle) had to be excluded from the evaluation. The third to fifth measurement cycles in each UV step, where the changes were smaller were considered reliable and used for further evaluation.

In the case of the mid-frequency semicircle, we could not rely on preliminary studies, therefore calculation of size independent properties was not trivial. As a starting point the fitted resistance data was inspected. Figure 3.19 shows the size dependency of the fitted resistance in the case of the sample with platinum microelectrodes. One can see that the resistance clearly does not scale linearly with the electrode diameter (*d*), but somewhere between its square and third power. On one hand the scaling suggests that the mid-frequency semicircle is not another bulk property. On the other hand, most electrochemical processes do not scale with d^3. Hence, it is assumed that the underlying property scales with the square of the electrode diameter, or more precisely with the electrode area, and some other effect distorts the pure scaling. The most probable cross-effect is the cooling effect of the needle, described earlier in section 3.2.1. As one can see in Figure 3.19 temperature has a significant effect on the resistance of the mid-frequency semicircle as well. 50 °C temperature difference causes almost the same effect as doubling the electrode diameter. The heat drain can be as much as 30 °C, and is more pronounced in the case of a smaller microelectrode, which could explain a higher than expected resistance value.
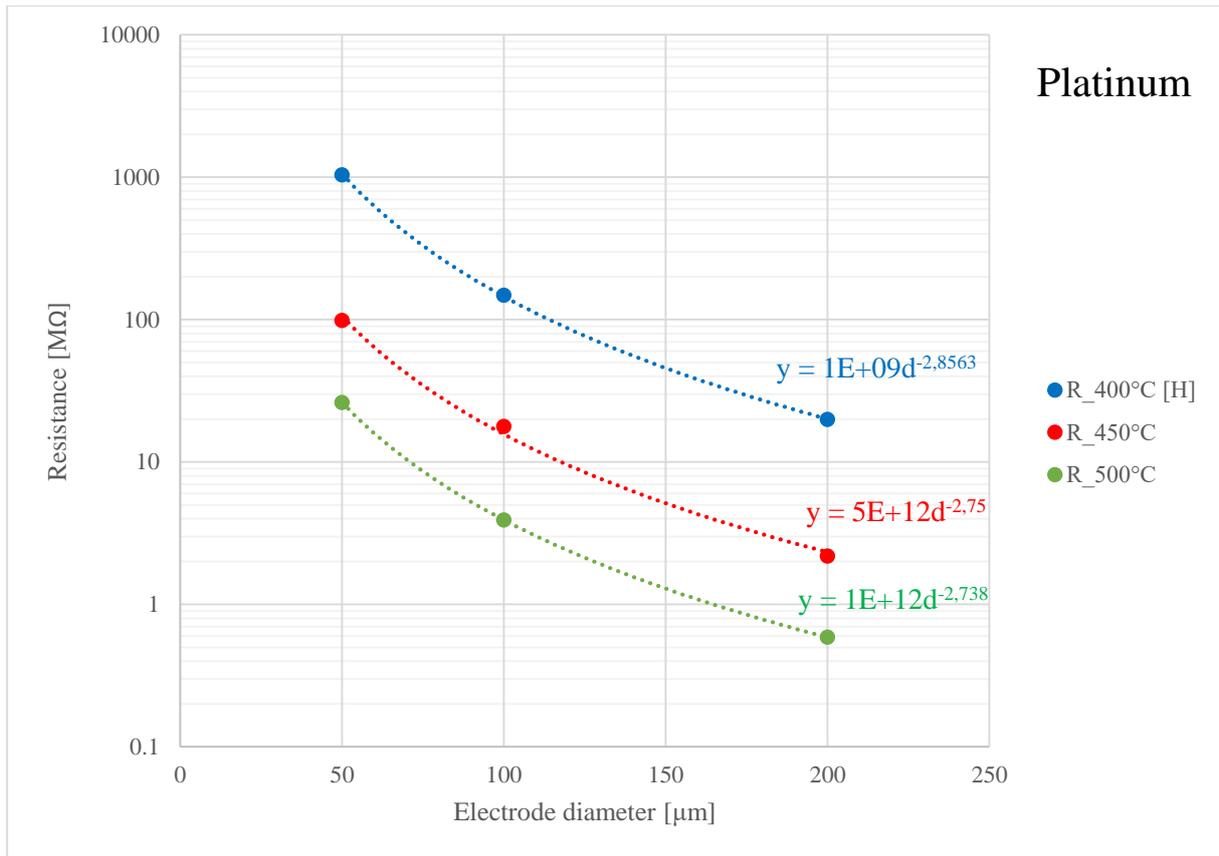
Figure 3.19 – Size and temperature dependence of the fitted resistance for the mid-frequency semicircle for platinum microelectrodes with fitted trend lines

A similar tendency can be observed in the case of the sample with LSC microelectrodes (Figure 3.20).
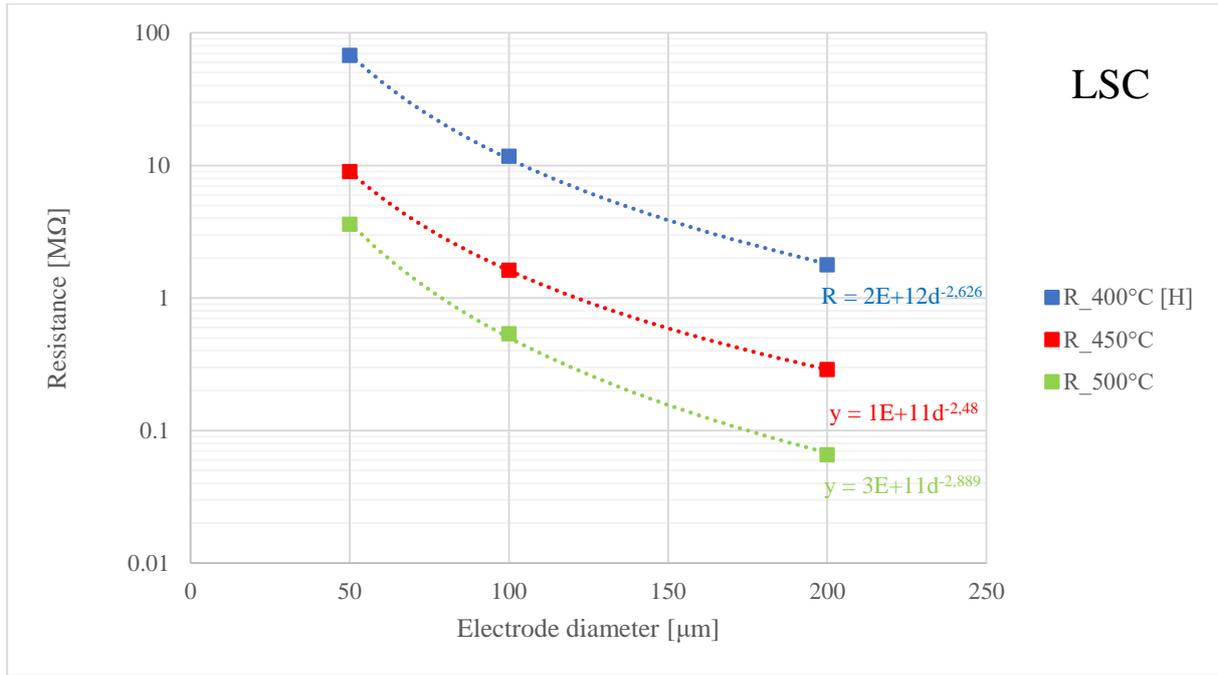
Figure 3.20 – Size and temperature dependence of the fitted resistance for the mid-frequency semicircle on different temperatures with LSC microelectrodes with fitted trend lines

Considering the possibilities of electrochemical processes in the sample which could scale with the area, a reasonable candidate is the space charge, which builds up between the strontium titanate substrate and the electrode layer. In that case the resistivity can be calculated if the space charge depth is known. According to literature a good estimation for acceptor doped STO is between 10 and 50 nm[77]. In the case of undoped STO the layer is somewhat thicker. Here a 200 nm thick space charge was assumed:

$$\rho_{microelectrode} = R * \frac{r^2 \pi}{200\ nm} \qquad (40)$$

Calculation was done similarly in the case of the grid electrode, by assuming an electrode size of 75% of the whole surface:

$$\rho_{grid} = R * \frac{0.75A}{200\ nm} \qquad (41)$$

The calculated resistivity values are shown in Figure 3.21 and Figure 3.22 for platinum and LSC electrodes respectively.
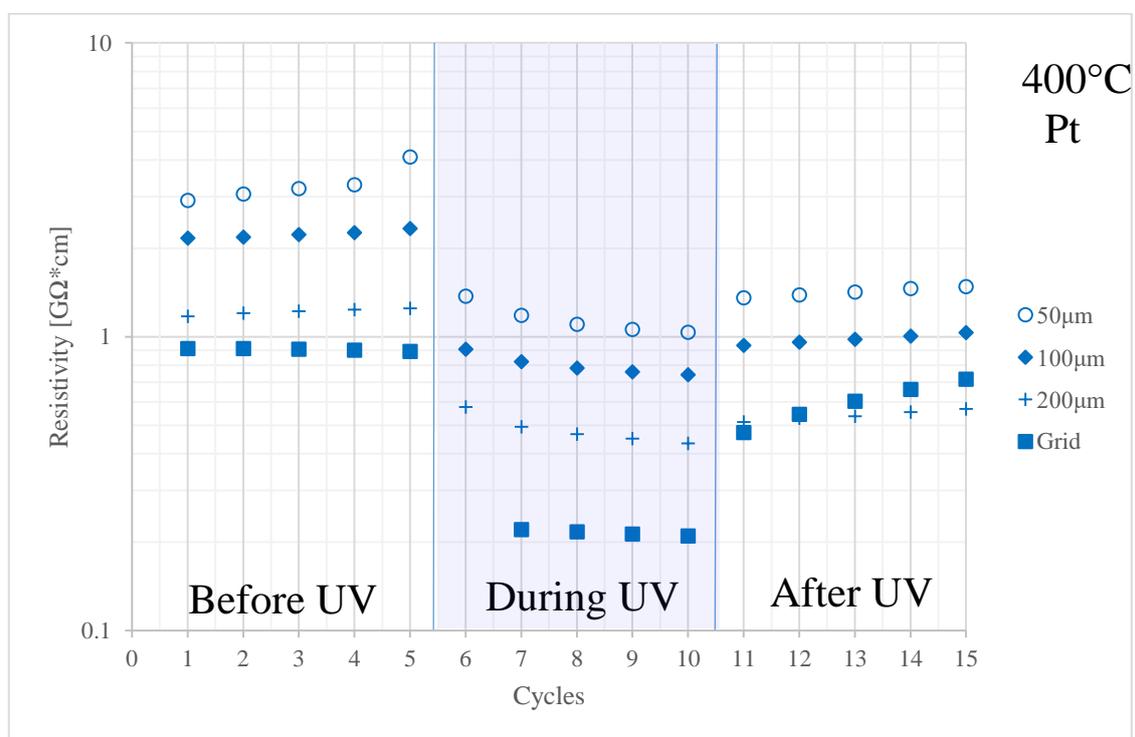

Figure 3.21 – Calculated resistivity of the mid-frequency semicircle of samples with platinum micro- and grid electrodes throughout the UV program

As expected, the size dependency did not disappear, however not only the microelectrodes are in close proximity, but the grid electrode with a significantly larger area is also in the same order of magnitude.

In the case of LSC electrodes, the disparity between the microelectrodes are similarly to platinum a factor of two, however the grid shows a larger difference with a factor of about six. The difference might be a result of an error in estimated area of the grid electrode.
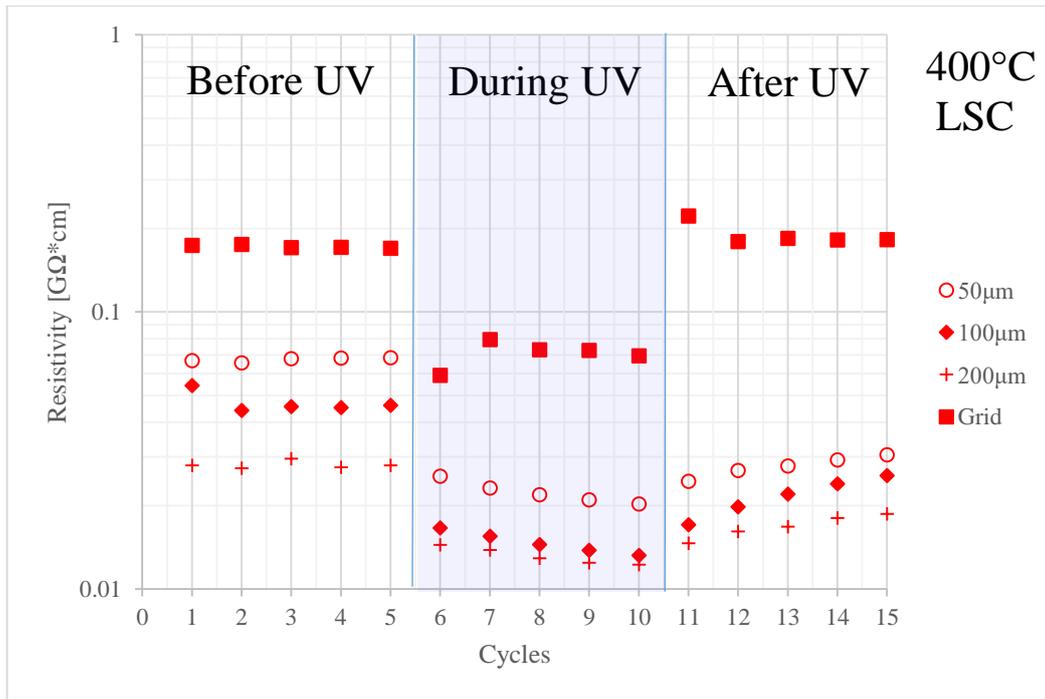
Figure 3.22 - Calculated resistivity of the mid-frequency semicircle of samples with LSC micro- and grid electrodes throughout the UV program

A clear UV effect can be determined for both electrode materials with about 60-70% drop of resistivity under UV irradiation. It is a well-documented phenomenon, that the photogenerated charge carriers can decrease the effect of the space charge layer.

The effect of UV irradiation diminishes with increasing temperature. The reason behind this is most likely the same that could be observed in the case of the high-frequency semicircle: The combined effect of thermally excited free charge carriers and a faster recombination reaction hinders further significant enhancement of the conductivity.
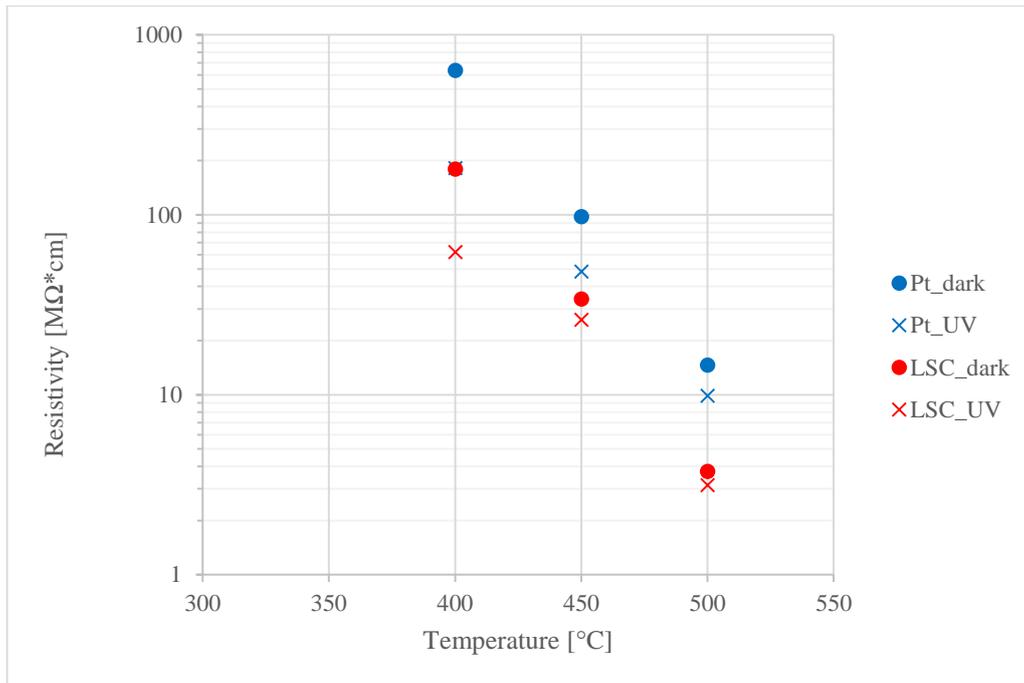
Figure 3.23 - Temperature dependence of the calculated resistivity and the UV-effect with two different grid electrode materials

In Figure 3.24 and Figure 3.25 the size and temperature dependence of the fitted capacitance is shown for samples with platinum and LSC microelectrodes respectively. Beside a clear negative temperature coefficient, a non-linear size dependence can be observed for both samples with platinum and LSC microelectrodes.
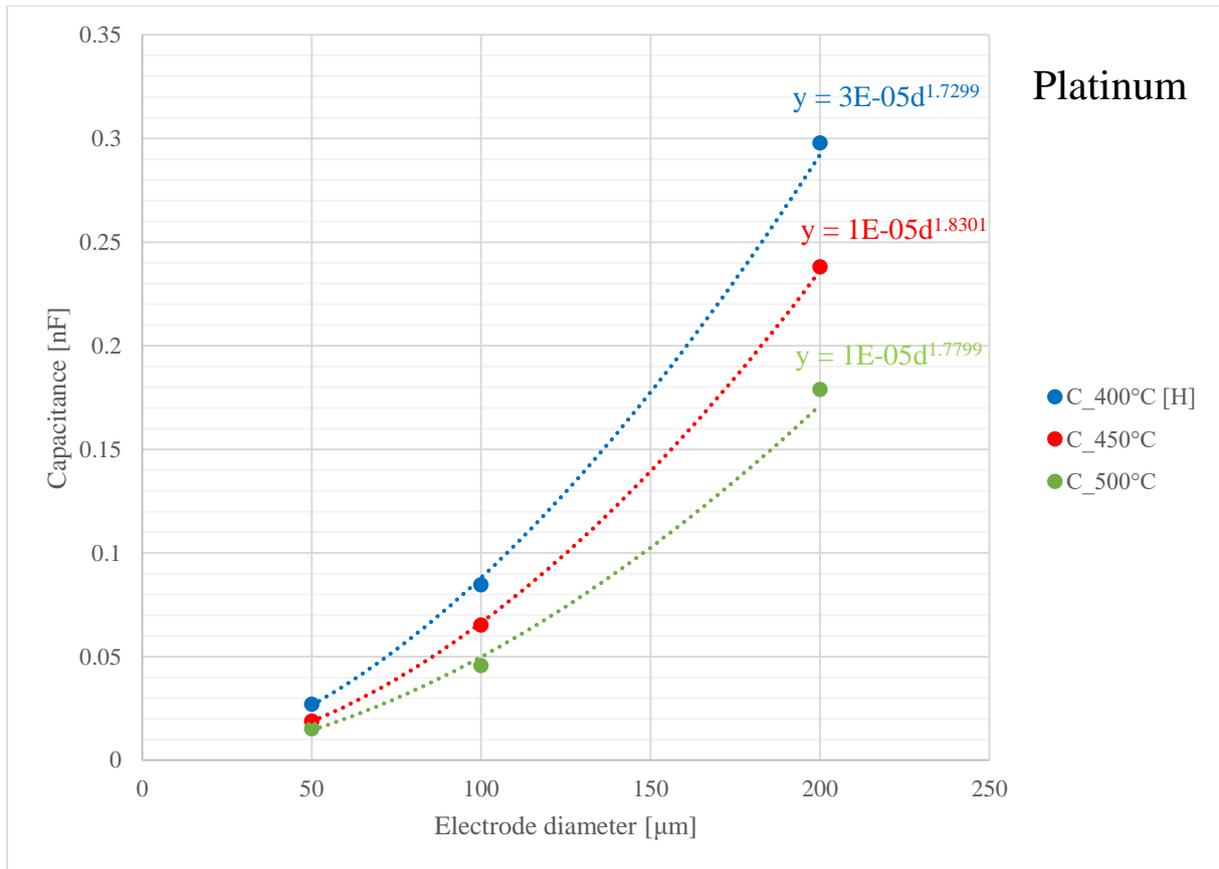
Figure 3.24 - Fitted capacitance of platinum microelectrodes of different sizes on different temperatures
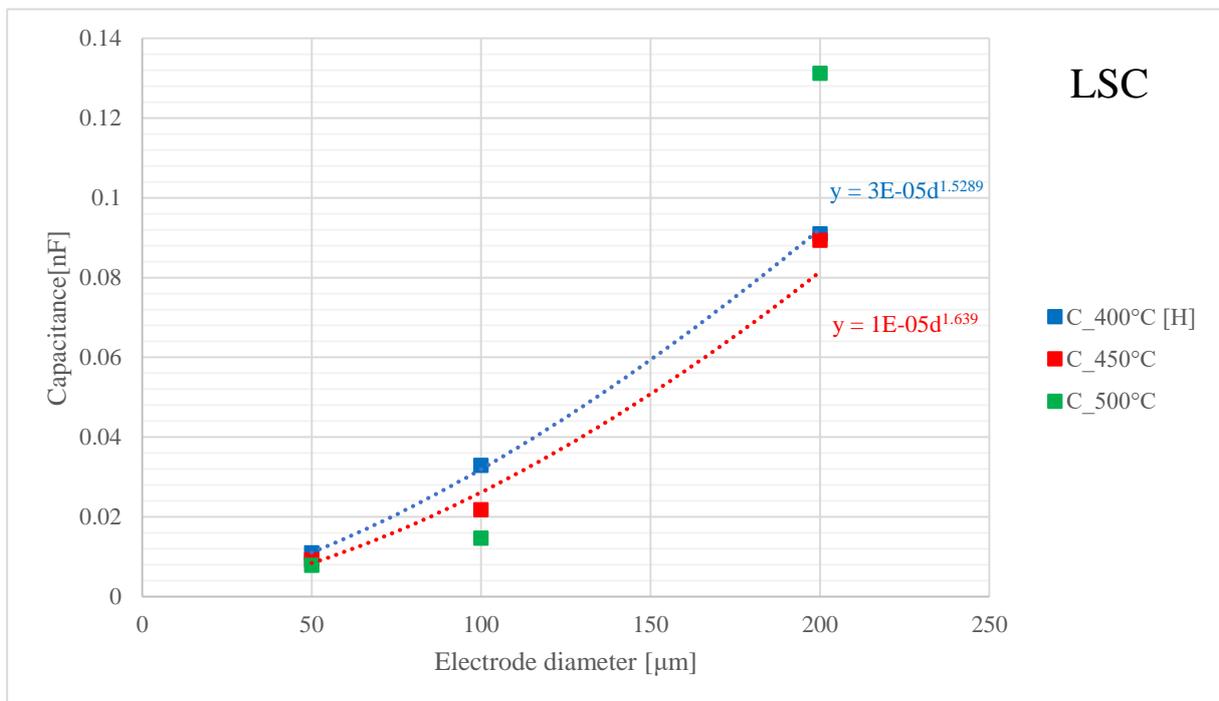

Figure 3.25 - Fitted capacitance of LSC microelectrodes of different sizes on different temperatures

However, the fitted trend lines show a scaling between linear and with the square of the diameter. In this case the earlier mentioned cooling effect also plays a role, however it should push the scaling towards the second power. Although, the exact reason for the discrepancy from the perfect scaling with the area is unknown, the existence of a disc-like space charge is the most reasonable assumption. The double layer capacitance in that case can be calculated in the case of microelectrodes by the following equation:

$$C_{SC} = \frac{C_{fitted}}{r^2 \pi} \tag{42}$$

since the electrode area in the case of the grid electrode is 75% of the sample area we get:

$$C_{SC} = \frac{C_{fitted}}{0.75 * A} \tag{43}$$

The calculated double layer capacitance values for the sample with platinum and LSC microelectrodes are shown in Figure 3.24 and Figure 3.25 respectively.
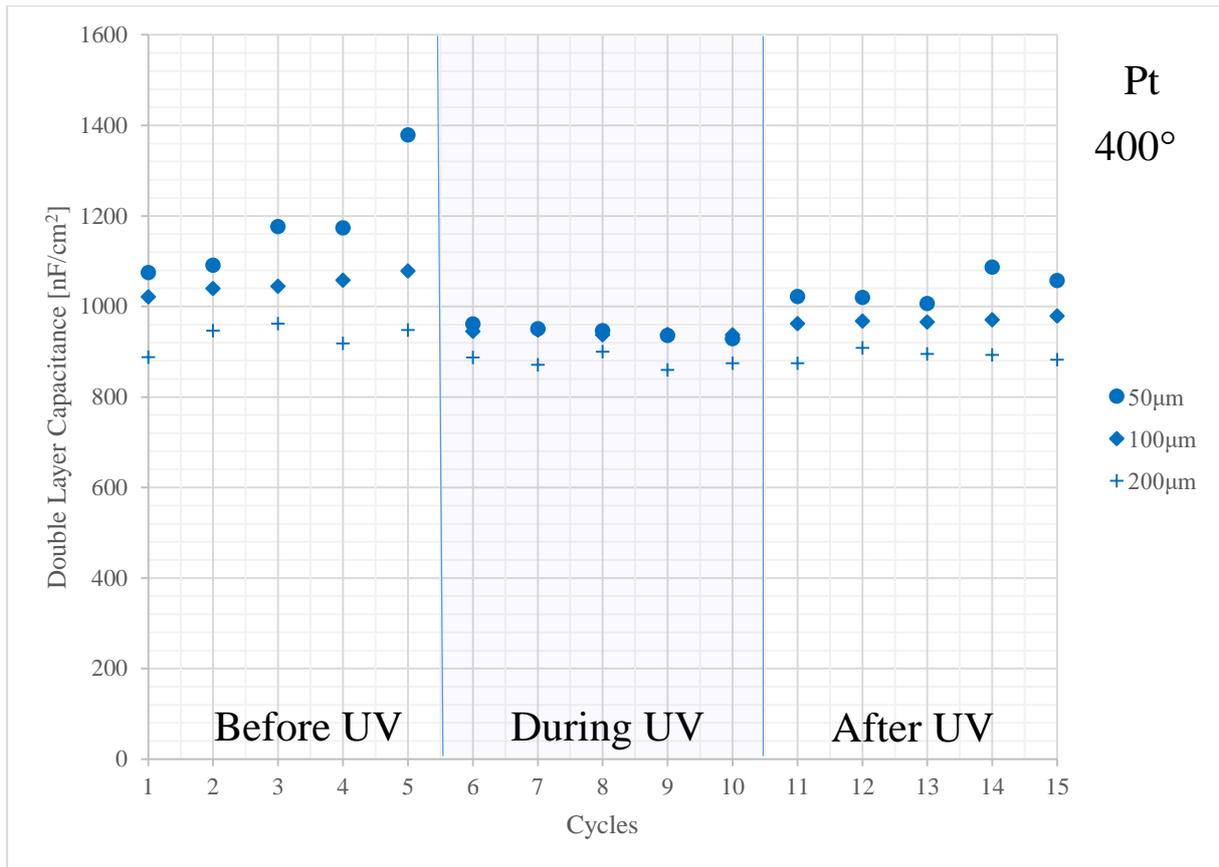
Figure 3.26 - Double layer capacitance of platinum microelectrodes on STO substrate at 400 °C
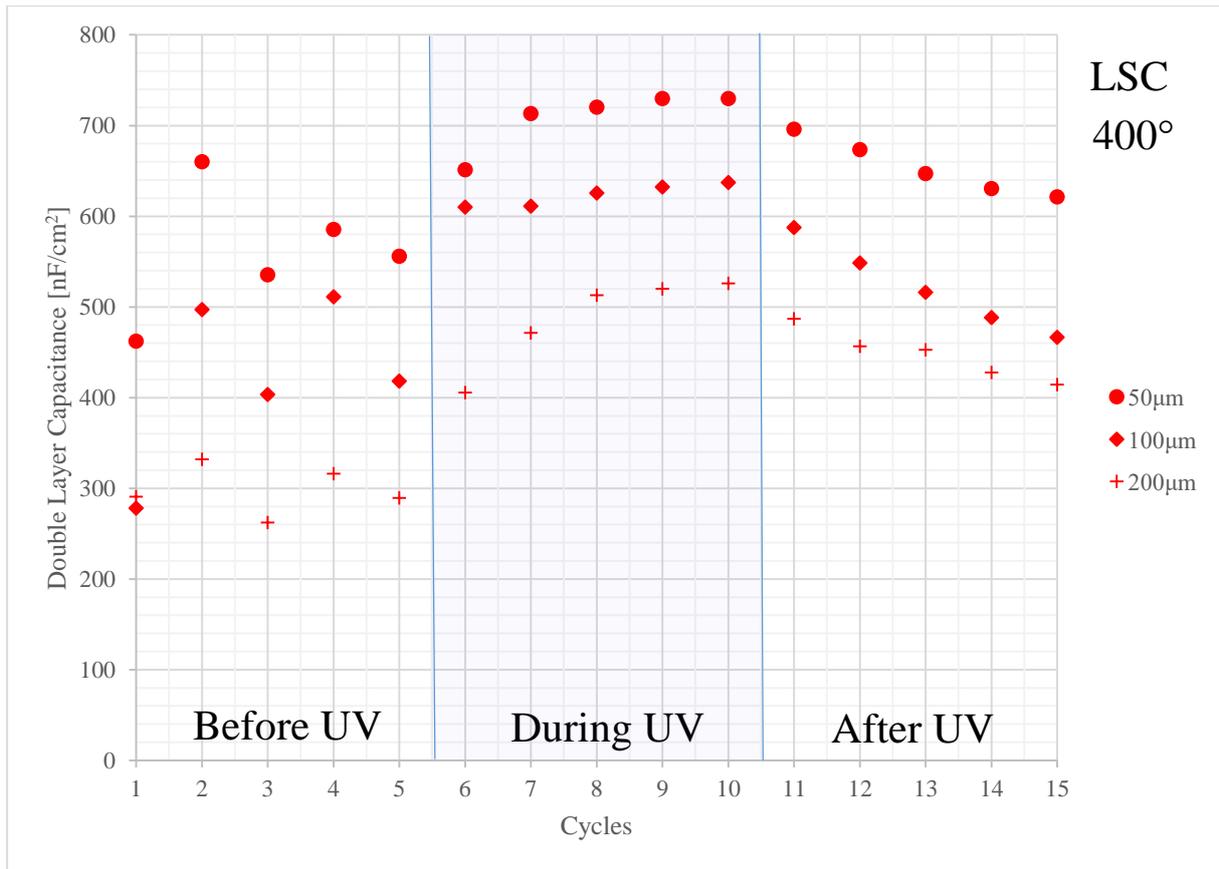
Figure 3.27 - Double layer capacitance of LSC microelectrodes on STO substrate at 400 °C

UV irradiation affects the double layer capacitance in the case of both electrode materials, however in different ways. The capacitance at the platinum-STO interface slightly decreases under UV illumination, the decrease persists subsequently in dark. The effect is somewhat larger in the case of the smallest microelectrode, however due to the scattering of the individual measurement points it is difficult to determine clear tendencies. Contrary to that, in the case of LSC microelectrodes, UV light causes a gradual increase of double layer capacitance, which slowly relaxes back to the initial value in dark.
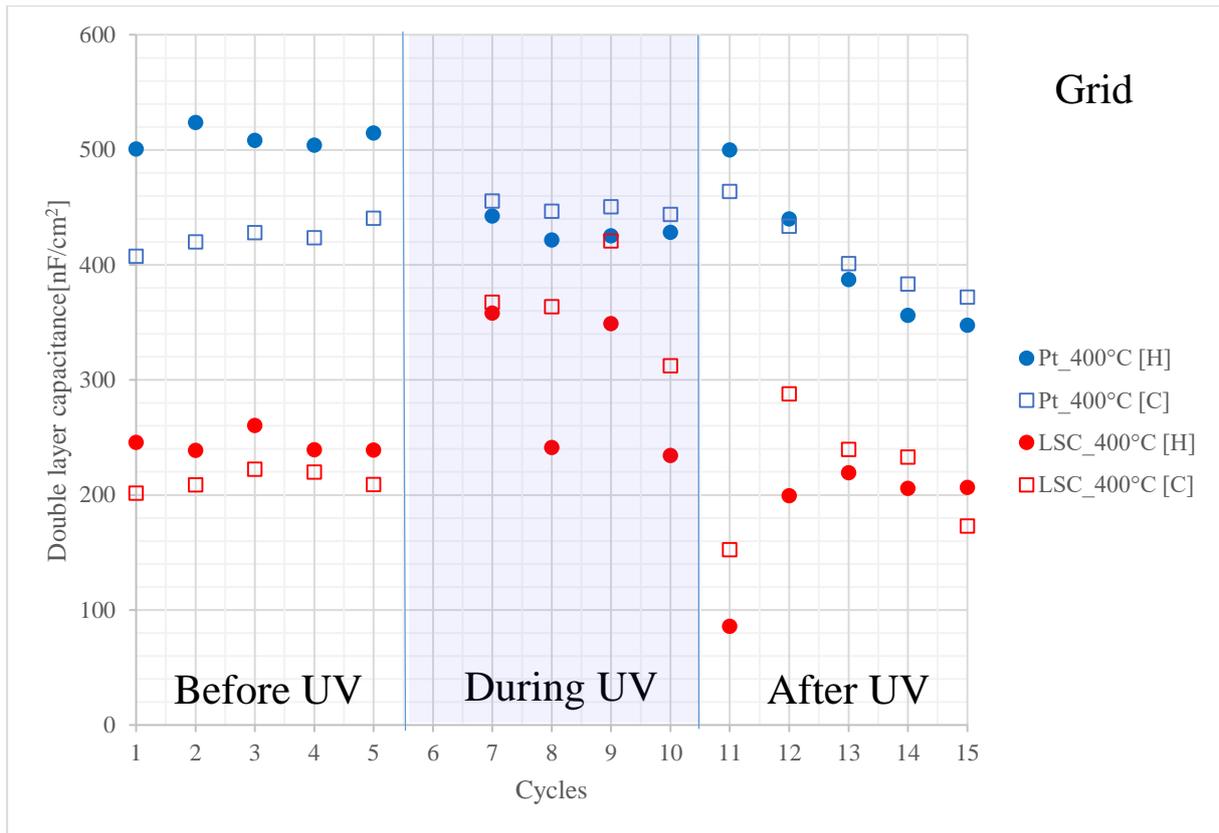
Figure 3.28 - Double layer capacitance at the space charge between the STO substrate and two different electrode materials

Calculation of the double layer capacitance with Equation 43 for the grid electrodes results in values in the same order of magnitude as for microelectrodes (Figure 3.28).

In Figure 3.29 the temperature dependence of the double layer capacitance and the effect of UV illumination is shown. The reaction upon ultraviolet light seem to change upon increased temperature in the case of platinum, however, this result is doubtful considering the uncertainty of the fitting results, which is also visible in the apparent sharp increase of the capacitance at 500 °C of the sample with LSC grid electrode. Nevertheless, a decreasing double layer capacitance would be expected under UV illumination, as the space charge should be suppressed by the excess free charge carriers.

Figure 3.29 - Temperature dependence of the double layer capacitance and the UV effect

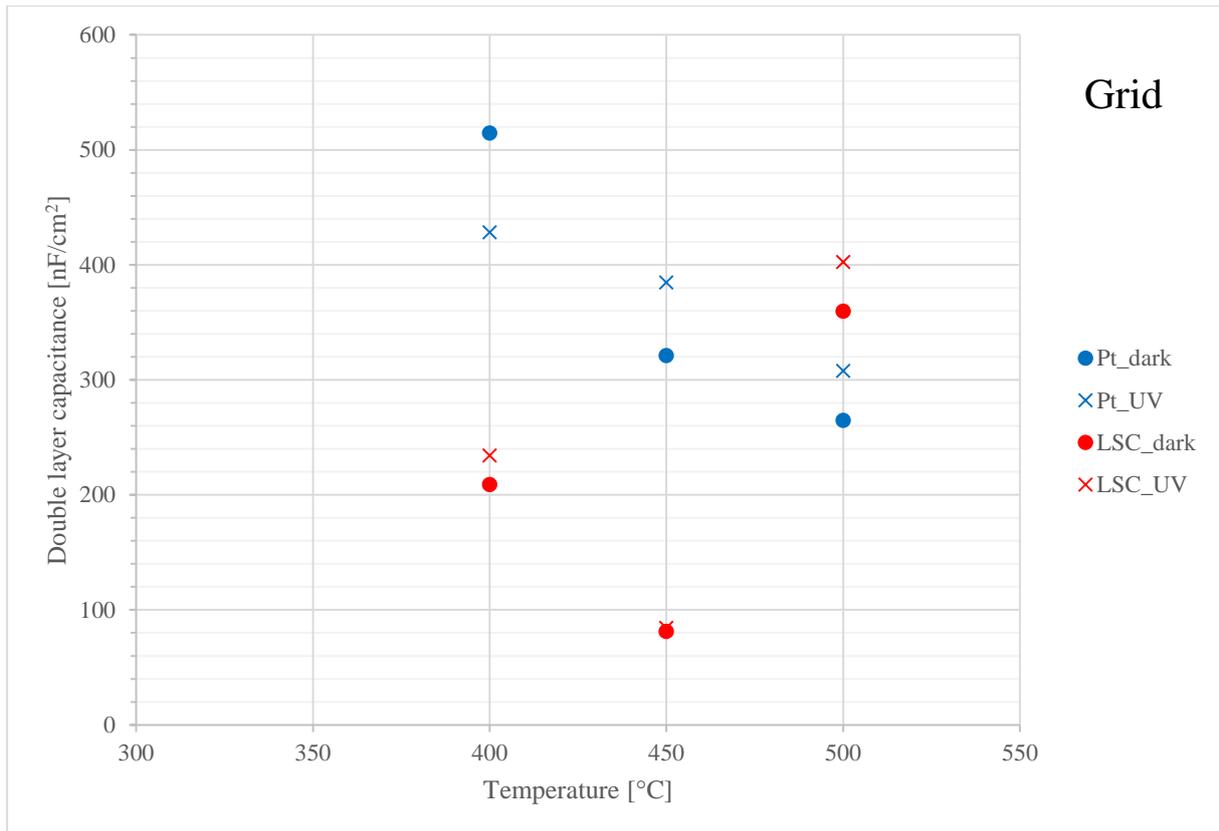Summarizing the analysis of the mid-frequency semicircle, a non-linear size dependence was observed for both the fitted resistance and capacitance values, and for both samples with platinum and LSC electrodes. However, the scaling was not perfectly quadratic due to distorting effects, such as the cooling of the measurement needle. Still the results suggest an electrochemical process dependent on the electrode size. A reasonable assumption is, that the mid-frequency semicircle stems from the space charge layer, which forms at the interface of the STO substrate and the electrode material. A modified equation was proposed accordingly for the calculation of resistivity and the double layer capacitance.

Resistivity has a negative temperature coefficient, which was expected due to the increased number of thermally activated free charge carriers at elevated temperature, which suppresses the space charge effect. UV illumination decreases the resistivity, due to the photogenerated free charge carriers. The effect diminishes with increasing temperature similarly and most likely for the same reasons as it was described in the case of the high-frequency semicircle (s. Section 3.2.1)

Evaluation of the double layer capacitance was more challenging as the results show significant scattering. It can be stated however, that the capacitance decreases with increasing temperature, however the effect is significantly smaller compared to the resistivity. Furthermore, a larger capacitance builds up at the interface of Pt|STO, than of LSC|STO. A more significant UV effect was observed at the sample with LSC electrode. Why UV illumination leads to an enhanced double layer capacitance is not understood yet.

3.2.3. The low-frequency semicircle

The low-frequency semicircle was in most cases only partially visible on the impedance spectra in the standard measurement range. The restricted visibility limits the possible depth of the investigation, which was also not the main focus of this thesis.

In most cases only the ascending branch lies in the standard measurement range, which however disappears under UV illumination. Furthermore, the third semicircle was not consistently present at the same temperature for all samples, which makes comparison harder. Also, even when fitting was possible, the fitted curve showed significant discrepancy, therefore those results are excluded from the evaluation. In order to get a clearer picture about the nature of the underlying process, few EIS measurements were attempted in an extended frequency range (10^6 – $3*10^{-3}$ Hz) as well. Unfortunately, only the sample with platinum microelectrodes could be meaningfully measured, as the sample with LSC electrodes got extremely noisy. Nevertheless, some conclusions can still be made. The EIS spectra taken from a sample with 100 μm platinum microelectrode is shown in Figure 3.30.
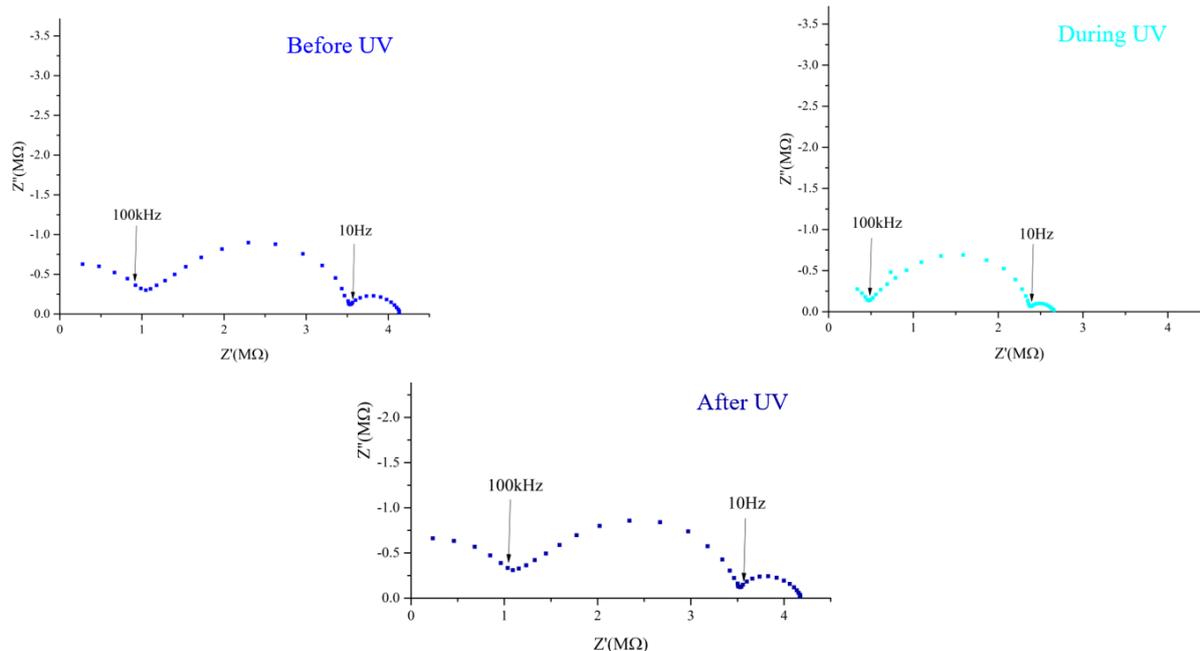
Figure 3.30 - EIS spectra of STO with 100 μm large platinum microelectrode at 500 °C

Looking at the EI spectra with extended frequency range, one can clearly state that no fourth semicircle exist. Also, compared to the other two semicircles, the low-frequency one is at least two times smaller than the other two. Fitting of a parallel R||CPE equivalent circuit reveals a relatively high capacitance, shown in Figure 3.31, which gets even higher under UV illumination. These values are higher than what one would expect in the case of a typical plate capacitor. The result of the first cycles during and after illumination are left out of the evaluation, as due to the slow measurement speed and fast changes under UV, these points could be fitted poorly. The fitted resistance is shown in Figure 3.32. UV irradiation causes a clear enhancement of the conductivity in the case of the process belonging to the third semicircle as well.

Figure 3.31 - Fitted capacitance values of the low-frequency semicircle of STO with 100 μm platinum micreoelectrode at 500 °C

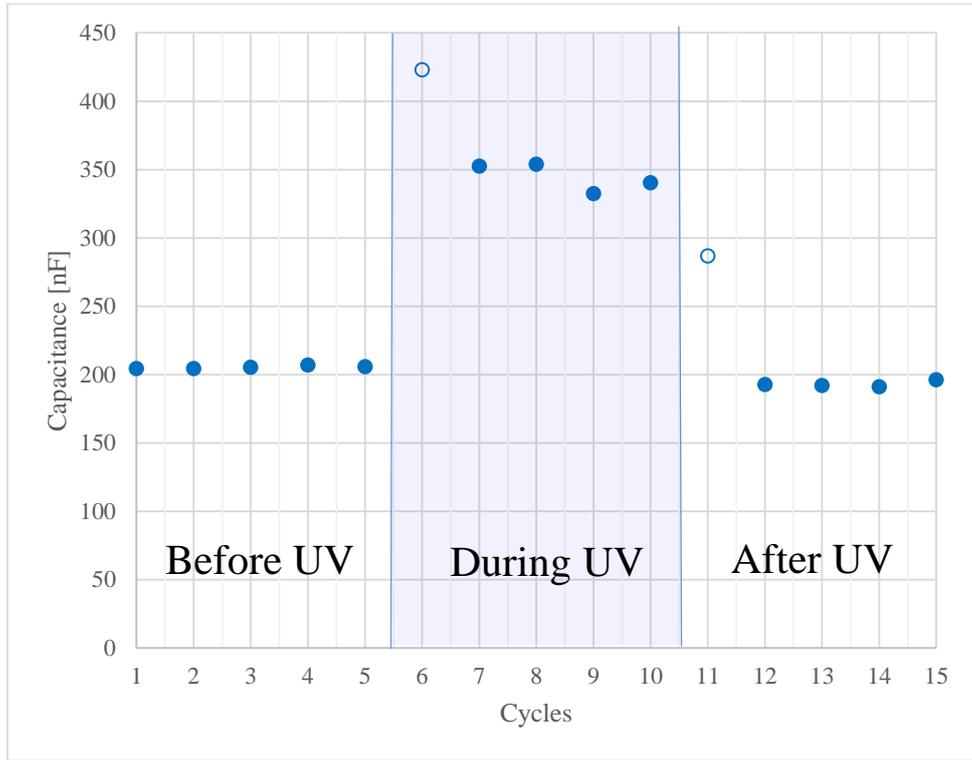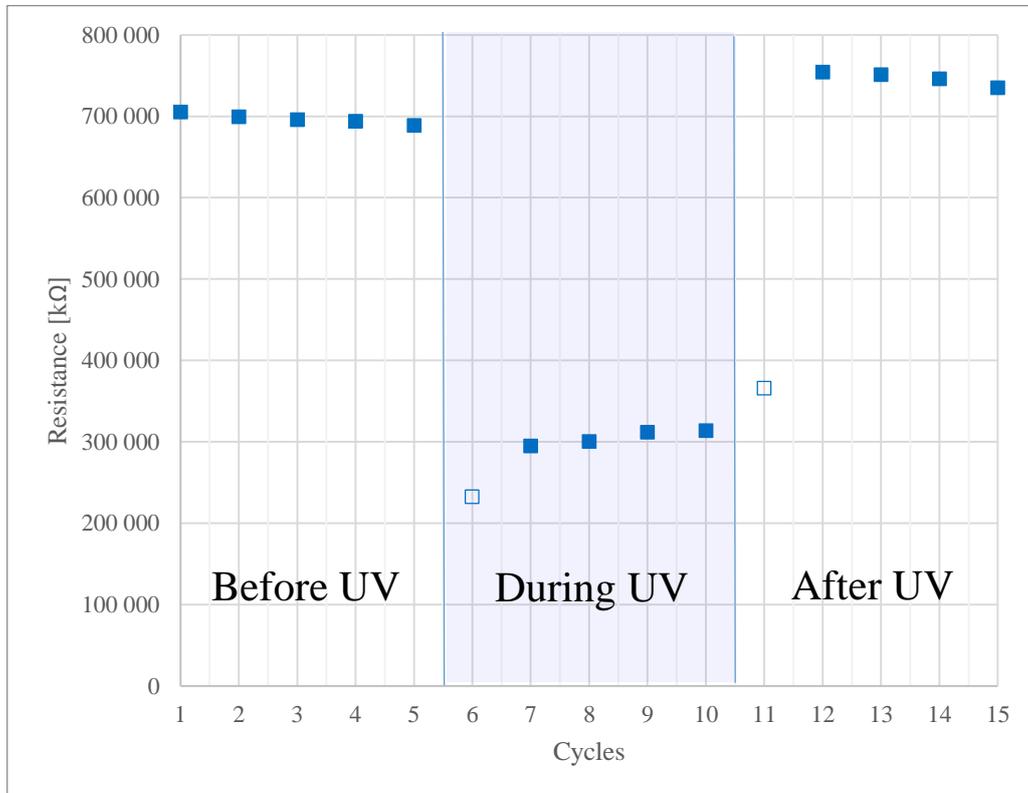*Figure 3.32 - Fitted resistance values of the low-freuqency semicircle of STO with 100 μm Pt microelectrode at 500 °C*

Although, no size or electrode material dependency was investigated in the framework of this thesis, a few conclusions could be drawn from the existing results. As it is the last semicircle the current path at the low frequency end of the process is the DC current path. This, together with a platinum electrode which is only electronically conductive, points towards a transition from an electronic+ionic conduction regime to a purely electronic one. Ultraviolet light has a clear and quick effect on it, which suggests that oxygen in- or excorporation is not involved, as it would be at least visibly slower after the illumination is over. These observations lead to the assumption that the low-frequency semicircle is caused by pure electronic conduction of the STO bulk. However, further investigation would be necessary for a more detailed analysis.

3.2.4. Summary and an improved equivalent circuit

Summarizing the results of the AC measurement section, we have observed that the electrochemical impedance spectra of strontium titanate samples with two different electrode materials generally consist of three semicircles. Investigation of the high-frequency semicircle indicate, that it can be assigned to the strontium titanate bulk. This was supported by the fact that the calculated relative permittivity values were in close proximity to the literature value of STO. Furthermore, the fitted properties were close to each other in case of two samples with LSC and platinum electrodes, which shows that the high-frequency semicircle is independent or more precisely only partially affected by the electrode material. Subsequently, the effect of ultraviolet light showed also striking similarities between samples, which could also be well explained by changes in strontium titanate.

Evaluation of the mid-frequency semicircle showed that the fitted resistance and capacitance values did not scale linearly with the electrode diameter as it would be expected for a bulk property, but with the area of the electrode. Behavior under illumination with ultraviolet light showed a significant difference between the two electrode materials, which means that the process is strongly affected by the electrode. Based on these observations, it was deduced that the second semicircle is caused by the space charge, which is generated at the substrate-electrode interface.

Deep investigation of the low-frequency semicircle was not conducted in the framework of this thesis, however evaluation of limited results and general considerations led to the assumption

that in such a low frequency range the only possible process is the pure electronic conduction of the strontium titanate substrate.

Considering the acquired knowledge with the help of electrochemical impedance spectroscopy an improved equivalent circuit is suggested for the measured system, which is shown in Figure 3.33.
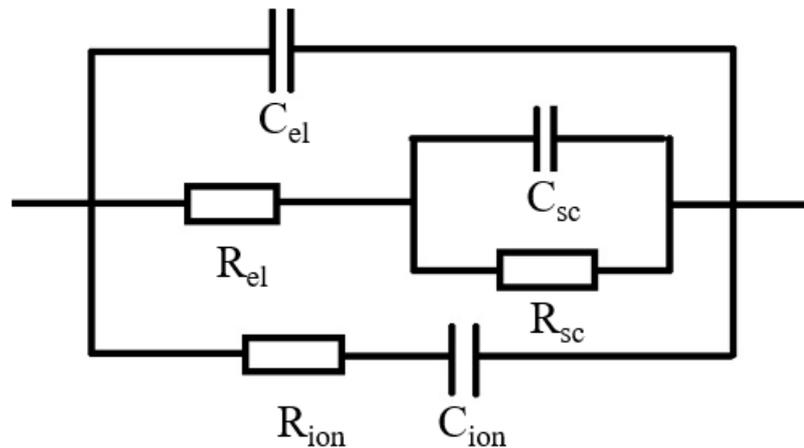
Figure 3.33 - New equivalent circuit for single crystal strontium titanate with electrodes

The elements R_{el} and C_{el} represent electronic conduction, while R_{ion} and C_{ion} are due to ionic conduction in strontium titanate bulk. R_{sc} and C_{sc} are the resistance and capacitance generated by the space charge respectively.

In DC case, current can only flow through the polarized space charge layer and, as in the STO bulk ionic conductivity is blocked (represented by C_{ion}), only electronic conduction is possible. At higher frequencies polarization of the space charge decreases, therefore the overall impedance decreases as well. Further increasing the AC frequency will enable ionic conductivity and further conduction paths.

Further testing of the applicability of the new model was not conducted in the framework of this thesis.

3.3. DC measurements

In the last section information was obtained about the different conduction paths in the samples, and how light affects those. The results revealed indirectly that UV illumination induces changes in the measured cell, which have different time constants. This section will attempt to investigate the nature of these changes by directly measuring the voltage change under UV illumination and the light induced current flow with a time resolution of 0.1 ms.

Earlier results were obtained in the working group in the framework of the PhD thesis of Gregor Walch[89], who also measured a few STO single crystal samples with platinum and gold electrodes, and a YSZ electrolyte in between. He addressed the challenge of equilibration of the samples at elevated temperatures. According to his calculations an optimal equilibration time for strontium titanate single crystal samples with a thickness of 500 μm at 400 °C would be about 6 days. This would imply unfeasible measurement times, so he chose to equilibrate the samples for 1 day, and in most cases this decision did not distort the results significantly. In the case of this thesis however, the given time span of the research was even more confined, therefore an equilibration time of 1 hour was chosen. This was enough in the case of grid electrodes, where the active current collector surface is large, however with microelectrodes, the results were affected by this restriction.

3.3.1. Photovoltage measurements

In his work Walch[89] realized a general tendency at the photovoltage measurements of single crystal STO samples, which led to the classification of *typical* and *atypical* effects. As the same general trend was realized in the results presented here, the next section will follow the classification and terminology of Walchs work as well. Figure 3.34 shows the *typical* light effect on a single crystal strontium titanate substrate with YSZ electrolyte and current collectors on both sides.
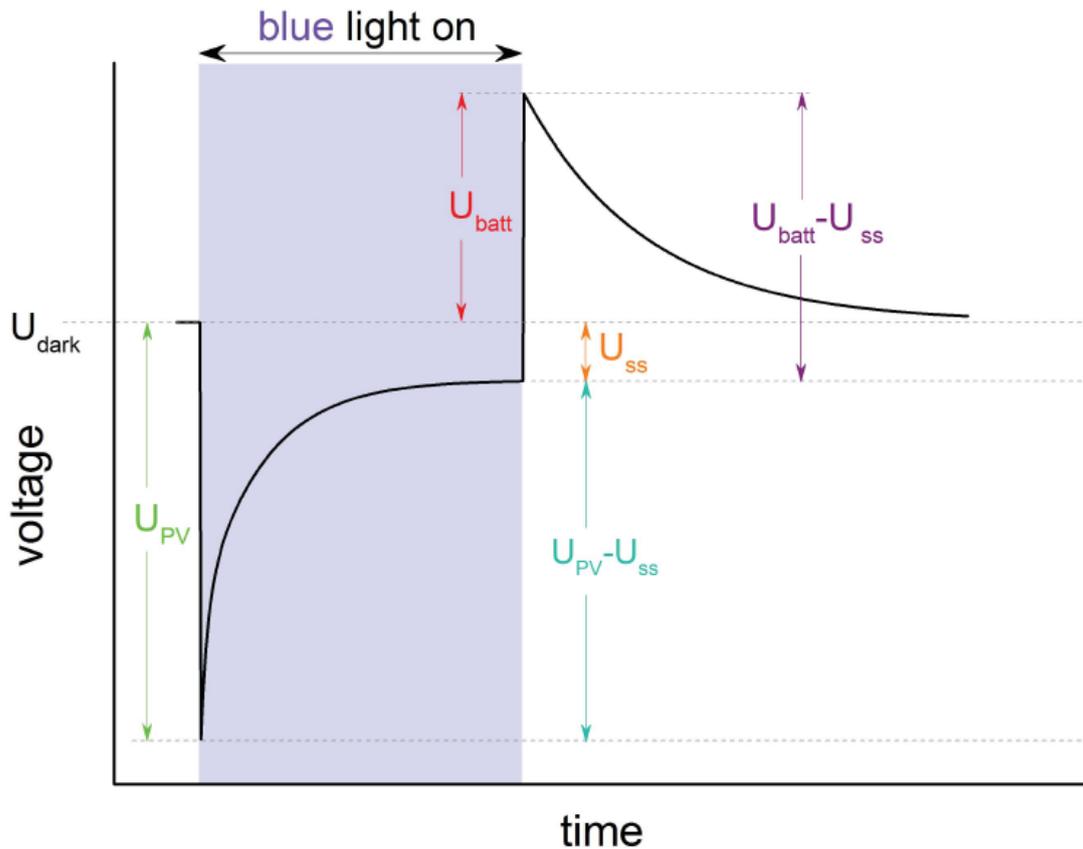
Figure 3.34 - Typical U(t) curve[3]

From left to right, U_{dark} is the voltage measured in dark before UV illumination. A significant dark voltage was observed and could only be partially explained by the formation of a thermoelectric voltage, due to the one sided heating of the sample. After turning UV illumination on, a quick jump occurs into the negative region. Walch concluded, that this jump is the photovoltaic contribution, caused by the charge separation of the photo-excited charge carriers at the electrode|STO interface. Here it is called U_{PV}, and is measured against U_{dark}. The voltage then generally takes up more positive values, subsequently reaching the steady-state voltage under UV irradiation. As Walch concluded, the voltage change is caused by the UV light driven oxygen incorporation. The exchange reaction is changing not only the defect chemistry but also the number of free charge carriers, and therefore the electrostatic potential, hence the measured photovoltage as well. While reaching this plateau the curve can have multiple inflection points. The voltage remaining after UV illumination (vs. U_{dark}) is given the

---

[3] Taken from the PhD thesis of G. Walch (2016)

name U_{batt}, as it is resembling the voltage of a battery which was charged during the illumination cycle. Subsequently the voltage reaches its dark value again, while oxygen excorporates from the lattice.

Results of the photovoltage measurement of strontium titanate single crystals with grid current collectors of LSC and platinum are shown in Figure 3.35. For both electrode materials the general UV effect can be well described by the *typical* curve introduced above. The ultraviolet light almost instantly generates a photovoltage, due to the photoexcitation of electrons from the valence to the conduction band. This voltage is larger in the case of LSC electrode, with a maximum absolute value of 100 mV, compared to 70 mV with platinum electrode. The difference can be attributed to the fact, that the maximum potential of the photovoltaic contribution is proportional to the height of the Schottky-barrier at the substrate-electrode interface. The voltage then gradually decreases due to the increased oxygen incorporation rate, which increases the hole concentration. In the case of grid electrodes, steady-state under UV illumination is reached in less than a minute.
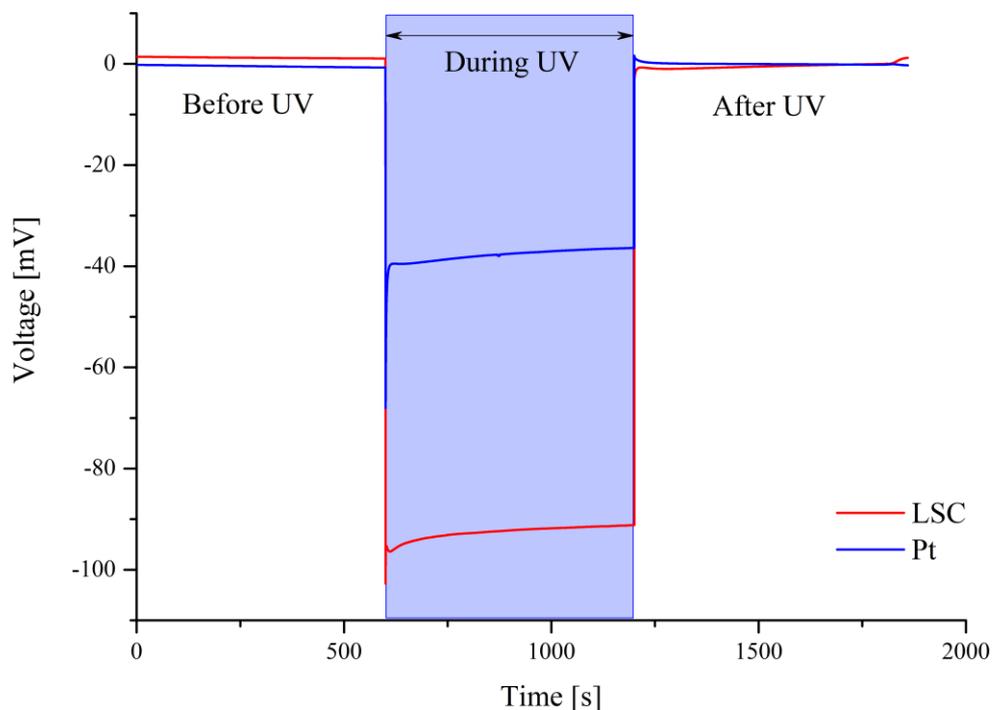
Figure 3.35 - Voltage curve of strontium titanate single crystal with grid electrodes at 400 °C

After turning the ultraviolet light off, the voltage instantly jumps back close to the dark value. In both cases a small feature appears directly after illumination is turned off. The absence of the battery voltage is caused by the fact that in this setup, the potential difference is measured directly between the top and bottom side of the strontium titanate substrate, and there is no electrolyte in between. The minor spike might be caused by a remaining inhomogeneous stoichiometry in STO and some ion conduction, i.e. STO acting partly as an electrolyte.

As seen by the AC measurements in section 3.2 , increasing temperature generally decreases the extent of the photo-effect. Photovoltage measurement of the same samples, seen in Figure 3.36 supports this observation.

Figure 3.36 - Photovoltaic contribution (U_{PV}) to the photovoltage at different temperatures

The voltage curves of samples with LSC microelectrodes were fallen partially into the *atypical* group, which made comparison and deduction of clear trends difficult. Moreover, as the equilibration and after UV relaxation times were longer, the measurement times were extended in some cases. A few examples are shown in Figure 3.37.

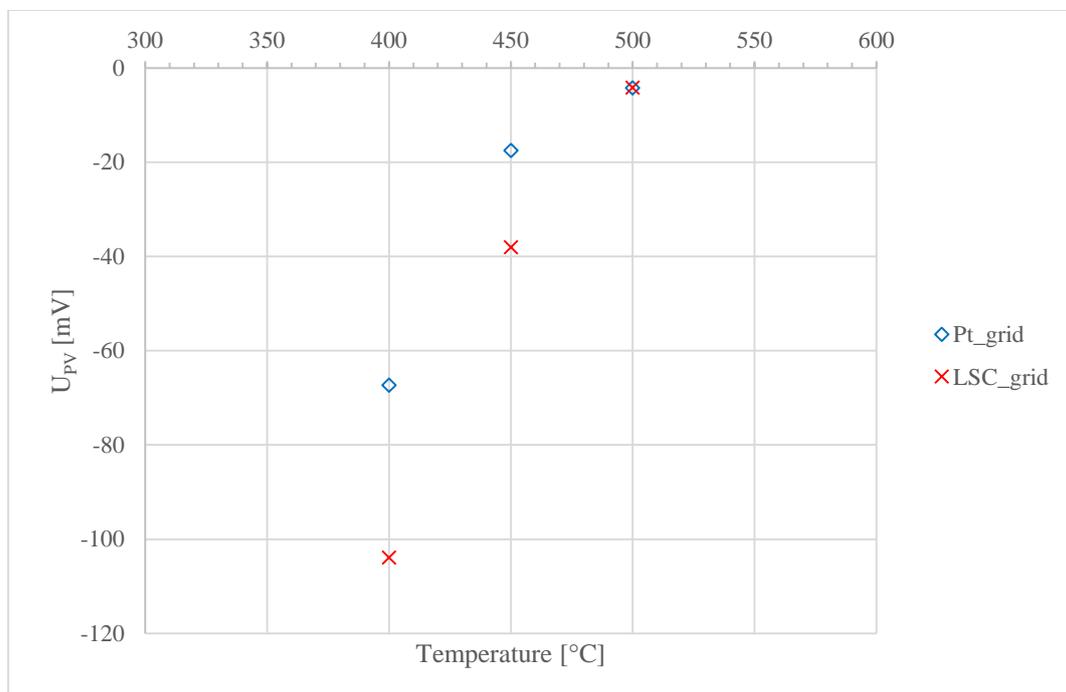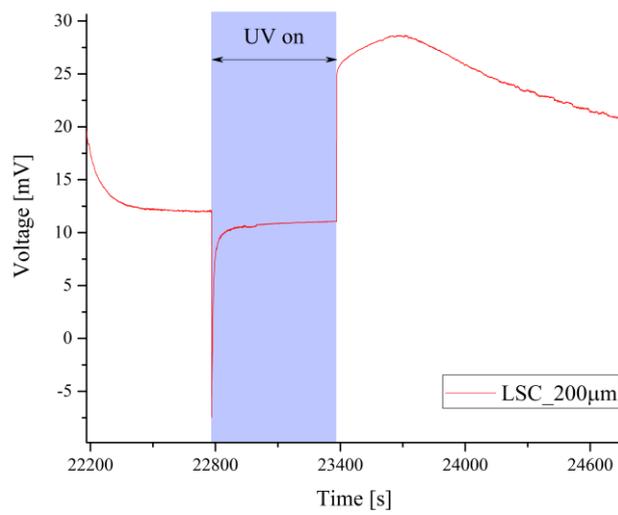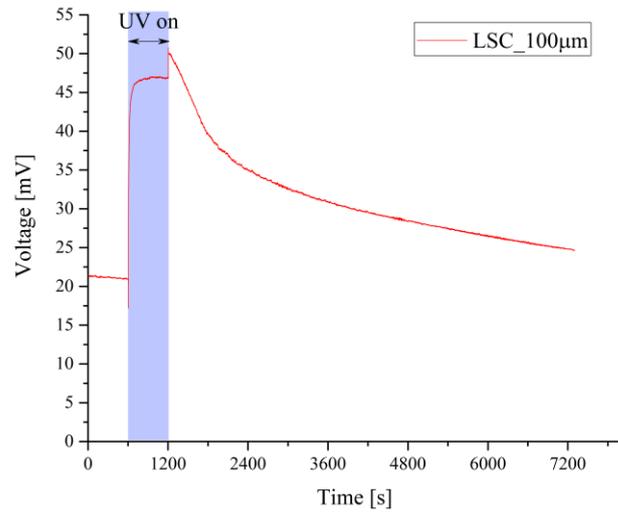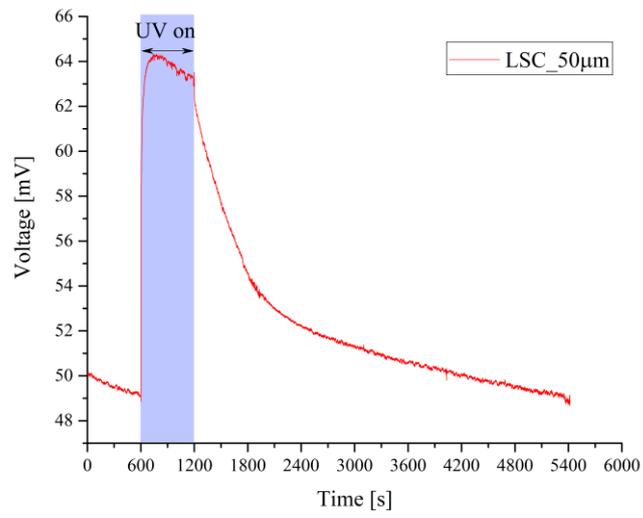*Figure 3.37 - Atypical voltage curves of LSC microelectrodes at 400°C*

Compared to the grid electrodes, LSC microelectrodes display significant dark current, which decreases with increasing electrode diameter. This could be explained by the temperature gradient caused by the cooling effect of the needle, explained more detailed in section 3.2.1. The photovoltaic contribution (U_{PV}) increases with increasing electrode size, which is well aligned with the assumption that it is directly connected to the space charge. In case of the 50 μm and 100 μm large electrodes, the steady-state voltage reached under UV illumination (U_{ss}) surpasses the dark voltage, which suggests that the first quick jump and the "charging" are two independent processes. The lack of the first does not hinder the second. However, the extent of the "charging" does not seem to scale clearly with size or temperature as seen in Figure 3.38.
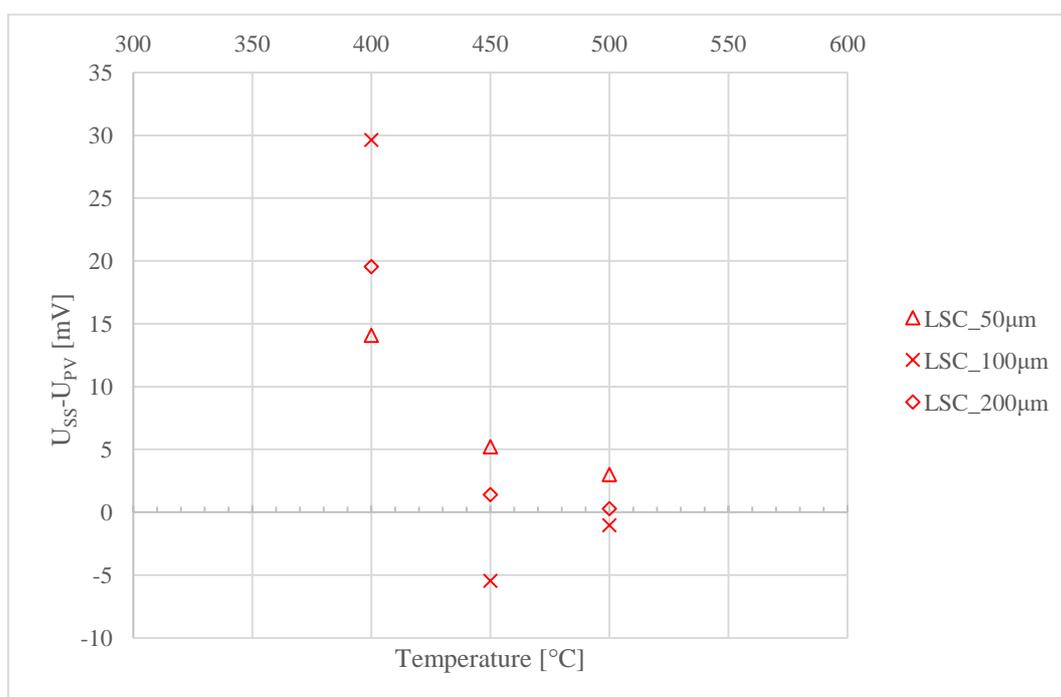
Figure 3.38 - Size and temperature dependence of the "charging" effect under UV illumination

Although battery voltage cannot exist in a way, as Walch has described it in his setup due the lack of an electrolyte, a similar effect can be observed in this case. An atypical effect can be seen in the case of the 200 μm LSC microelectrode, where the after UV relaxation begins by a further increase of the voltage, and only starts to converge to the dark value after ca. 5 minutes.

Measurement of strontium titanate single crystal with platinum microelectrodes yielded solely *atypical* curves with irregular photo-effects. Some examples are shown in Figure 3.39. The dark voltage, which was present in the case of the LSC microelectrodes is even larger in this case, nevertheless with increasing electrode area, it decreases. Possible reason is the better heat conducting property of platinum compared to LSC, which leads to more significant heat drain from the sample. In the case of the 50 μm large electrode, an unusually long equilibration time was necessary under UV irradiation, which was followed by an even longer relaxation process after ultraviolet light was turned off. Moreover, the jump after UV is much smaller than the one under UV illumination, which results in a smaller battery voltage, than the dark voltage.
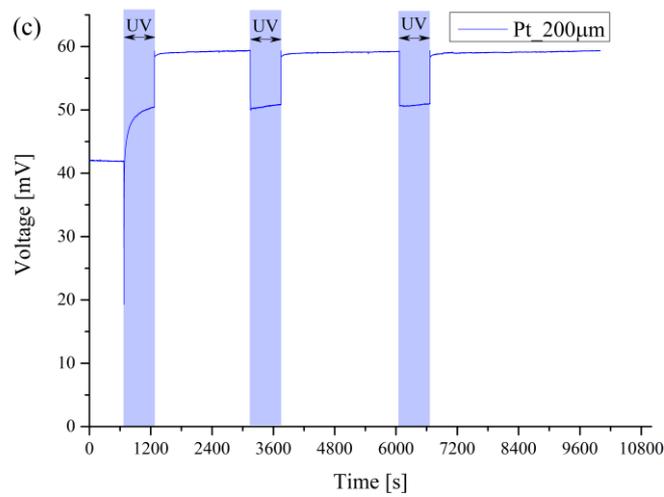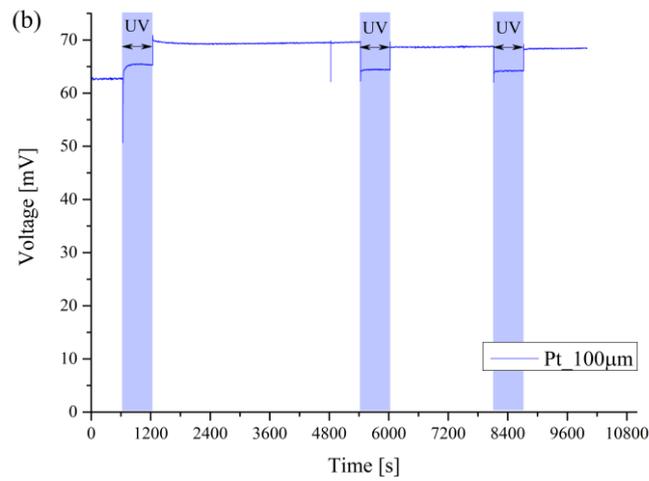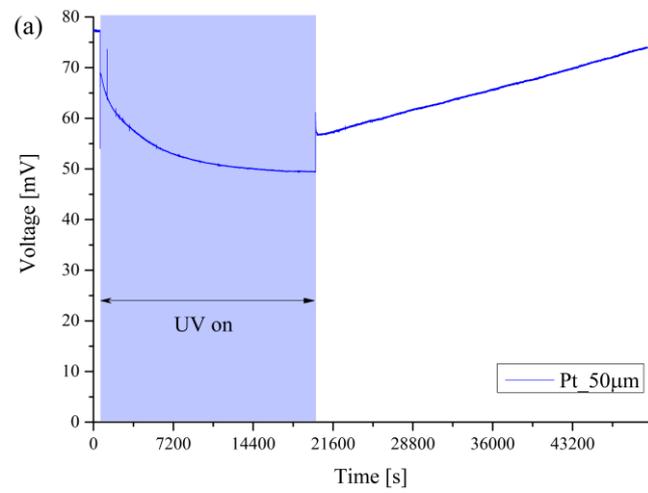
Figure 3.39 - Voltage curves of platinum microelectrodes at 400 °C

The two larger microelectrodes (100 μm, 200 μm) showed a photo-effect closer to the typical curve upon illumination with ultraviolet light. However, after turning the light source off, the battery voltage seems to persist. Upon repeated illumination, the quick drop of the photovoltage appears though, however, it is on one hand smaller than at the first illumination, on the other hand the "charging" of the battery voltage is absent as well. Possible reason could be the bad ion conducting property of platinum, which means that oxygen exchange reaction can only happen in the vicinity of the triple phase boundary. In the case of the larger microelectrodes the triple phase boundary (TPB) to area ratio is significantly lower compared to the 50 μm large microelectrode or the grid current collector. This could lead to a situation, where oxygen, incorporated into the lattice under the driving force of UV light, cannot excorporate in dark without additional energy input (e.g. heating). However, this ratio is only two times smaller in the case of the 100 μm microelectrode compared to the smallest. This could though explain a slower relaxation rate, but not a complete persistence. Moreover, the effect is inconsistent with the EIS results, where microelectrodes showed although a slower relaxation, but not a complete persistence.

3.3.2. Photocurrent measurements

Photocurrent measurements were conducted on the grid samples as well. Deeper investigation of the current curves was not conducted in the framework of this thesis, nevertheless it can supply additional information to the behavior of strontium titanate under UV illumination. The general shape of the current curves closely resembles the voltage curves; thus an analogous terminology will be used.

Current curves of strontium titanate single crystal samples with LSC and platinum grid current collectors on various temperatures are shown in Figure 3.40. Generally, all curves show similar characteristics: After stable dark current, significant photocurrent builds up over time under UV illumination, which gets faster at higher temperatures. Both sample show a small positive peak after UV is turned off, which is analogous to the battery voltage, seen earlier in section 3.3.1. However, some striking differences can be observed as well: In the case of platinum grid current collector (Figure 3.40 (a-c)), a small local peak appears right after turning the UV light on. This is a similar feature as the photovoltage (U_{PV}), although in this case, the peak increases with increasing temperature, and is seemingly absent in the case of the LSC grid. However, at 500 °C (Figure 3.40 (f)) a maximum peak, following closely what was seen at the voltage curves can

be observed. The photocurrent builds up although significantly slower in the beginning in the case of a platinum current collector, it reaches a larger current than the sample with LSC electrode. This could be a contradiction to what was observed in the case of the PV measurement, as larger photovoltage should mean a larger driving force. However, it is important to keep in mind, that current is an extensive variable. A larger sample can generate larger current, and in the case of these two particular samples, the one with LSC grid is about half the size of the one with platinum current collector. Further surprising is the steadily growing photocurrent under continuous illumination, as the photovoltage was decreasing over time due to the stoichiometric contribution. If the voltage, as a driving force is decreasing, a decreasing photocurrent would be expected. However, results of the EIS measurement showed, that the overall resistivity of the sample also decreases under UV illumination. The system must obey Ohm's law, which means, that the resistivity decreases more significantly, than the voltage under UV illumination.
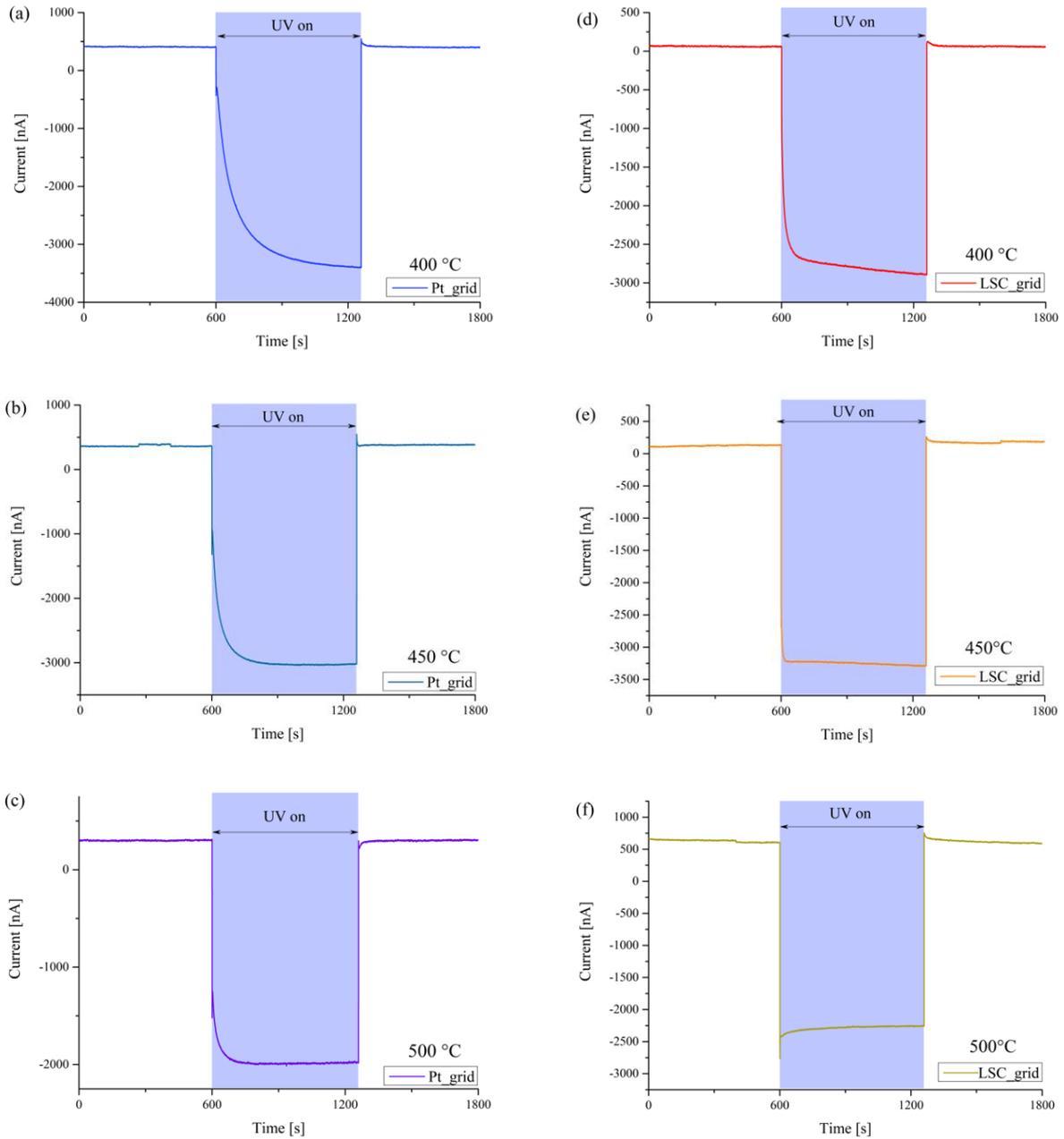
Figure 3.40 - Current curves of STO samples with platinum (a-c) and LSC (d-f) current collectors at various temperatures

Temperature dependence of the maximum photocurrent (I_{SS} - I_{dark}) for the two different electrode materials are shown in Figure 3.41. It is expected as seen earlier that increasing temperature decreases any photo-effect. In the case of platinum grid electrode this tendency is clear. 100 °C temperature difference causes almost 50% drop in maximum achievable photocurrent. The sample with LSC grid current collector does not show a clear tendency however. Possible reason could be that at 400 °C equilibrium under UV irradiation was not reached, which suggests a higher maximum current at that temperature.
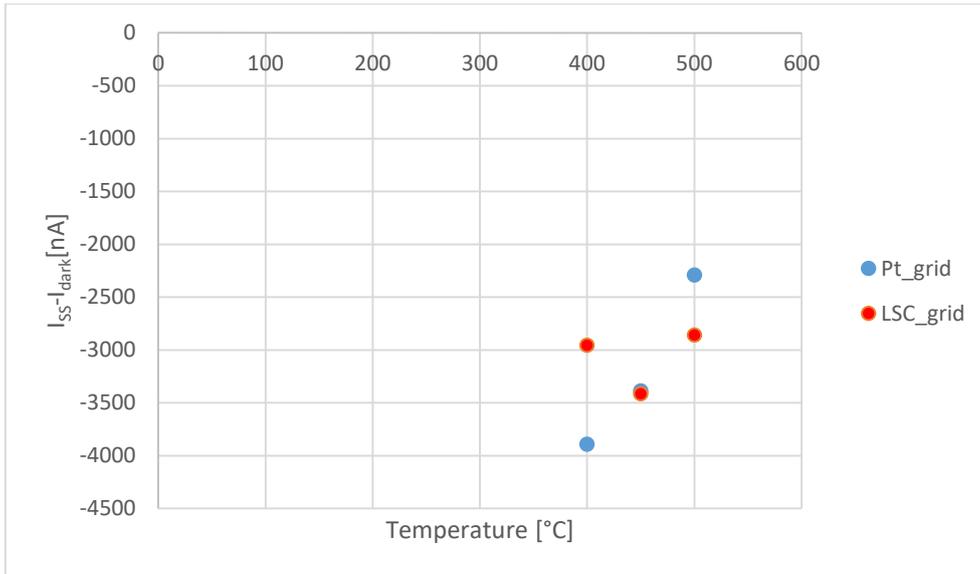
Figure 3.41 - Temperature dependence of maximum photocurrent

Analogous to the PV measurements, a small feature is also present here after turning UV off, which for the sake of simplicity we define as a battery current (Figure 3.42), although only very little battery effect is expected, as explained in section 3.3.1. Seemingly the trends show that while with platinum grid electrode temperature causes the decrease of battery current, in the case of LSC grid the effect is the opposite. Note, that the extremely low I_{batt} for Pt_grid at 500 °C is most probably a result of the atypical shape of the current curve after UV, and not a total absence of the battery effect.
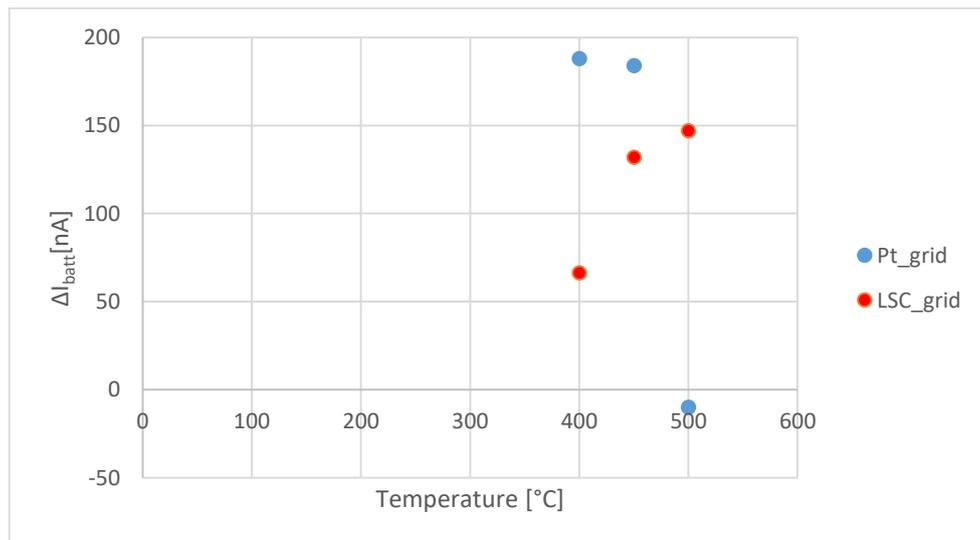
Figure 3.42 - Temperature dependence of the battery current

3.3.3. Summary

Photovoltage and photocurrent measurements of strontium titanate samples yielded insight to the nature of the changes under UV illumination by giving a better time resolution compared to EIS measurements. Voltage curves of both samples with grid electrodes made of LSC and Pt follow a typical course, and the light effect is generally well explained by conclusions made earlier by Walch: Most UV effects can be described as a sum of two parts. First, the photovoltaic contribution causes a sudden peak, which is followed by a slower voltage decrease, caused by the stoichiometric contribution (enhanced oxygen incorporation). The photovoltaic contribution is larger in the case of LSC electrode, which suggests a larger Schottky-barrier at the STO|LSC, than at the STO|Pt interface. No battery voltage was observed in the case of grid electrodes, due to the lack of electrolyte material. In the case of microelectrodes, the equilibration time under UV illumination was significantly shorter than the subsequent relaxation in dark. This underpins the earlier reported observation of Merkle[88] that UV light enhances solely the incorporation of oxygen into the lattice, while the excorporation in dark stays slow. Although, the voltage curves of the microelectrode samples were mostly atypical, it can be stated, that relaxation after UV illumination is faster with LSC electrodes, due to the good oxygen-ion conductivity of the electrode material, which helps the surface reaction. Both light induced changes (photovoltage, battery voltage) diminish with increasing temperature. In the case of samples with microelectrodes, significant dark voltage was observed regardless of the electrode material, which decreased with increasing electrode size. The reason is most probably a thermal gradient caused by the one sided heating, and the heat draining effect of the measurement needle.

Photocurrent measurement of the two samples with grid electrodes revealed that the current curves under UV illumination closely resemble the main features of the *typical* voltage curves. However, contrary to voltage, photocurrent increases over time under UV light. As the voltage as driving force should decrease under the same condition, this result suggests that the enhanced conductivity of the strontium titanate bulk (see section 3.2) is more significant from the viewpoint of current flow. A small peak after turning UV off analogous to the battery voltage could also be observed. This could be caused by the excess free electrons generated by the excorporation reaction. Increasing temperatures generate dark currents, due to the thermal gradient, shorten equilibration time and decrease the maximum achievable photocurrent.

4. Conclusions

The aim of this thesis was to get a better understanding of the changes in the electrical and conductive properties of strontium titanate under UV illumination. In order to achieve this goal, high-temperature solid state photoelectrochemical cells of undoped strontium titanate single crystals were measured utilizing AC (electrochemical impedance spectroscopy) and DC (photovoltage, photocurrent) methods. The EIS spectra revealed three conductive pathways in different frequency ranges. The high-frequency arc was found to be the combined electronic and ionic conductivity of the strontium titanate bulk. The result was not only supported by preliminary measurements by Walch with similar conclusion, but also calculating the relative permittivity matching the literature value of STO. Moreover, the electrode material had only limited influence on the arc and the effect of UV illumination on the semicircle could be satisfactorily explained by assumed changes in the bulk substrate. Investigation of the mid-frequency semicircle showed that the fitted resistance and capacitance values were scaling roughly with the electrode area. Moreover, the mid-frequency arc showed a more significant dependence on the electrode material, or more precisely on the electrode|STO interface. It was concluded that in the mid-frequency range the space charge layer generates a double layer capacitance and a resistance by depletion of free charge carriers. The third semicircle was found to be the last one as well, meaning that it ends in the DC pathway. Without deeper investigation, a good assumption is that it corresponds the pure electronic conductivity of the strontium titanate bulk. Utilizing the acquired knowledge, a new equivalent circuit was suggested, which should better describe the behavior of STO.

All three semicircles were strongly affected by UV light. The combined ionic and electronic conductivity of STO is found to increase up to one order of magnitude, depending on the electrode material. The change could be adequately explained under various conditions by the enhanced incorporation of oxygen into the STO lattice and the shift of the stoichiometric equilibrium in the bulk. The space charge was also affected by UV light, decreasing the resistance by up to a factor of six. The effect can be interpreted as the light-induced change of the Schottky barrier at the STO|electrode interface. Subsequently the electronic conduction was also influenced, the corresponding arc shows a decreasing resistance by a factor of two, which

can be explained as well by the incorporation of oxygen, and the consequent increase of electron hole concentration and decrease of oxygen vacancies.

In order to achieve better time resolution, DC measurement were conducted as well. The results supported the conclusions of Walch, who suggested, that the photovoltage, which builds up under UV illumination, can be attributed to two separate processes: A photovoltaic and a stoichiometric contribution. The former is caused by the illumination of the Schottky barrier at the electrode|STO interface and the subsequent separation of photogenerated charge carriers. The latter is connected to the enhanced incorporation of oxygen into the STO lattice under UV light, and the subsequent excorporation in dark. Photocurrent measurements have revealed a similarity in current and voltage curves, with the main difference being the gradual increase of photocurrent compared to the decrease of voltage under UV illumination.

Hence by the present study deeper understanding of the electrochemical processes and electrical property changes in strontium titanate under the influence of UV light was achieved.

Acknowledgment

I would like thank Prof. Fleig for giving me the possibility of this thesis in the working group and for the insightful discussions. This thesis would also not exist without Dr. Kubicek, who was aiding my every step from the very first ones, stumbling through the complex sample preparation, to the very last discussions. His ideas and undiminished enthusiasm were catalysts of my work.

Furthermore, I would like to thank all colleagues for helpful advices and friendly support: Gregor W., Bernhard, Alex V., Alex O., Edvinas, Michi , Matthias, Alex S., Ghislain, Max, Alex S., Alex H., Clemens.

The work in the group could not flow unimpeded without the tireless work of "The Force", Udo, Kurt, Eva, solving administrative, IT and gas issues.

Finally, I would like to thank my family and friends, for the support.

References

1.   Bube, R.H., *Photoelectronic properties of semiconductors*. 1992: Cambridge University Press.

2.   Zhang, Q.G., B.Y. Cao, X. Zhang, M. Fujii, and K. Takahashi, *Influence of grain boundary scattering on the electrical and thermal conductivities of polycrystalline gold nanofilms*. Physical Review B, 2006. **74**(13): p. 134109.

3.   Nuss, M., D. Auston, and F. Capasso, *Direct subpicosecond measurement of carrier mobility of photoexcited electrons in gallium arsenide*. Physical Review Letters, 1987. **58**(22): p. 2355.

4.   Studenikin, S., N. Golego, and M. Cocivera, *Carrier mobility and density contributions to photoconductivity transients in polycrystalline ZnO films*. Journal of Applied Physics, 2000. **87**(5): p. 2413-2421.

5.   Law, K.Y., *Organic photoconductive materials: recent trends and developments*. Chemical Reviews, 1993. **93**(1): p. 449-486.

6.   Johnson, H.L., *Astronomical measurements in the infrared*. Annual Review of Astronomy and Astrophysics, 1966. **4**(1): p. 193-206.

7.   Feurer, T., A. Glass, and R. Sauerbrey, *Two-photon photoconductivity in SiC photodiodes and its application to autocorrelation measurements of femtosecond optical pulses*. Applied Physics B: Lasers and Optics, 1997. **65**(2): p. 295-297.

8.   Cui, D., J. Xu, S.-Y. Xu, G. Paradee, B.A. Lewis, and M.D. Gerhold, *Infrared photodiode based on colloidal PbSe nanocrystal quantum dots*. IEEE transactions on nanotechnology, 2006. **5**(4): p. 362-367.

9.   Yusa, G. and H. Sakaki, *Trapping of photogenerated carriers by InAs quantum dots and persistent photoconductivity in novel GaAs/n-AlGaAs field-effect transistor structures*. Applied Physics Letters, 1997. **70**(3): p. 345-347.

10.   Fonash, S., *Solar cell device physics*. 2012: Elsevier.

11.   Shockley, W. and H.J. Queisser, *Detailed Balance Limit of Efficiency of p-n Junction Solar Cells*. Journal of Applied Physics, 1961. **32**(3): p. 510-519.

12.   Green, M.A., K. Emery, Y. Hishikawa, W. Warta, and E.D. Dunlop, *Solar cell efficiency tables (Version 45)*. Progress in Photovoltaics: Research and Applications, 2015. **23**(1): p. 1-9.

13.   Manser, J.S., J.A. Christians, and P.V. Kamat, *Intriguing Optoelectronic Properties of Metal Halide Perovskites*. Chemical Reviews, 2016. **116**(21): p. 12956-13008.

14. Bryant, D., N. Aristidou, S. Pont, I. Sanchez-Molina, T. Chotchunangatchaval, S. Wheeler, J.R. Durrant, and S.A. Haque, *Light and oxygen induced degradation limits the operational stability of methylammonium lead triiodide perovskite solar cells.* Energy & Environmental Science, 2016. **9**(5): p. 1655-1660.

15. Chun-Ren Ke, J., A.S. Walton, D.J. Lewis, A. Tedstone, P. O'Brien, A.G. Thomas, and W.R. Flavell, *In situ investigation of degradation at organometal halide perovskite surfaces by X-ray photoelectron spectroscopy at realistic water vapour pressure.* Chemical Communications, 2017. **53**(37): p. 5231-5234.

16. Juarez-Perez, E.J., Z. Hawash, S.R. Raga, L.K. Ono, and Y. Qi, *Thermal degradation of $CH_3NH_3PbI_3$ perovskite into NH_3 and CH_3I gases observed by coupled thermogravimetry-mass spectrometry analysis.* Energy & Environmental Science, 2016. **9**(11): p. 3406-3410.

17. Yuan, Y., Q. Wang, Y. Shao, H. Lu, T. Li, A. Gruverman, and J. Huang, *Electric-Field-Driven Reversible Conversion Between Methylammonium Lead Triiodide Perovskites and Lead Iodide at Elevated Temperatures.* Advanced Energy Materials, 2016. **6**(2): p. 1501803-n/a.

18. Matteocci, F., L. Cinà, E. Lamanna, S. Cacovich, G. Divitini, P.A. Midgley, C. Ducati, and A. Di Carlo, *Encapsulation for long-term stability enhancement of perovskite solar cells.* Nano Energy, 2016. **30**(Supplement C): p. 162-172.

19. Callegaro, L., *Electrical impedance: principles, measurement, and applications.* 2012: CRC Press.

20. Gellings, P.J. and H. Bouwmeester, *Handbook of solid state electrochemistry.* 1997: CRC press.

21. Bockris, J.O.M. and A.K. Reddy, *Modern electrochemistry 2B: electrodics in chemistry, engineering, biology and environmental science.* Vol. 2. 2000: Springer Science & Business Media.

22. Johnson, D.H., *Origins of the equivalent circuit concept: the voltage-source equivalent.* Proceedings of the IEEE, 2003. **91**(4): p. 636-640.

23. Millikan, R.A., E.S. Bishop, and A.T. Society, *Elements of Electricity: A Practical Discussion of the Fundamental Laws and Phenomena of Electricity and Their Practical Applications in the Business and Industrial World.* 1917: American Technical Society.

24. Alexander, C.K. and M.N.O. Sadiku, *Fundamentals of Electrical Circuits.* 5th ed.

25. Fleig, J., *Microelectrodes in solid state ionics.* Solid State Ionics, 2003. **161**(3): p. 279-289.

26. Jones, F.L., *The physics of electrical contacts.* 1957: Clarendon Press.

27. Holm, R. and E. Holm, *Electric contacts handbook.* 1958: Springer.

28. Newman, J., *Resistance for flow of current to a disk.* J. Electrochem. Soc, 1966. **113**(5): p. 501-502.

29.   Fleig, J. and J. Maier, *Finite element calculations of impedance effects at point contacts.* Electrochimica Acta, 1996. **41**(7): p. 1003-1009.

30.   Scholz, F., *Electroanalytical methods.* Vol. 1. 2010: Springer.

31.   Macdonald, J.R. and W.B. Johnson, *Fundamentals of impedance spectroscopy.* Impedance Spectroscopy: Theory, Experiment, and Applications, Second Edition, 2005: p. 1-26.

32.   Hirschorn, B., M.E. Orazem, B. Tribollet, V. Vivier, I. Frateur, and M. Musiani, *Determination of effective capacitance and film thickness from constant-phase-element parameters.* Electrochimica Acta, 2010. **55**(21): p. 6218-6227.

33.   Fricke, H., *XXXIII. The theory of electrolytic polarization.* The London, Edinburgh, and Dublin Philosophical Magazine and Journal of Science, 1932. **14**(90): p. 310-318.

34.   Brug, G., A. Van Den Eeden, M. Sluyters-Rehbach, and J. Sluyters, *The analysis of electrode impedances complicated by the presence of a constant phase element.* Journal of Electroanalytical Chemistry and Interfacial Electrochemistry, 1984. **176**(1-2): p. 275-295.

35.   Maier, J., *Evaluation of Electrochemical Methods in Solid State Research and Their Generalization for Defects with Variable Charges*, in *Zeitschrift für Physikalische Chemie*. 1984. p. 191.

36.   Steinsvik, S., R. Bugge, J. GjØnnes, J. TaftØ, and T. Norby, *The defect structure of $SrTi_{1-x}Fe_xO_{3-y}$ (x=0–0.8) investigated by electrical conductivity measurements and electron energy loss spectroscopy (EELS).* Journal of Physics and Chemistry of Solids, 1997. **58**(6): p. 969-976.

37.   Cowley, R., *Lattice dynamics and phase transitions of strontium titanate.* Physical Review, 1964. **134**(4A): p. A981.

38.   Lytle, F.W., *X-Ray Diffractometry of Low-Temperature Phase Transformations in Strontium Titanate.* Journal of Applied Physics, 1964. **35**(7): p. 2212-2215.

39.   Fleury, P., J. Scott, and J. Worlock, *Soft Phonon Modes and the 110° K Phase Transition in SrTi O 3.* Physical Review Letters, 1968. **21**(1): p. 16.

40.   Rossella, F., P. Galinetto, G. Samoggia, V. Trepakov, and L. Jastrabik, *Photoconductivity and the structural phase transition in $SrTiO_3$.* Solid State Communications, 2007. **141**(2): p. 95-98.

41.   Müller, K.A. and H. Burkard, *SrTiO3 An intrinsic quantum paraelectric below 4 K.* Physical Review B, 1979. **19**(7): p. 3593-3602.

42.   Itoh, M., R. Wang, Y. Inaguma, T. Yamaguchi, Y. Shan, and T. Nakamura, *Ferroelectricity induced by oxygen isotope exchange in strontium titanate perovskite.* Physical Review Letters, 1999. **82**(17): p. 3540.

43.   Uwe, H. and T. Sakudo, *Stress-induced ferroelectricity and soft phonon modes in $SrTiO_3$.* Physical Review B, 1976. **13**(1): p. 271.

44. Bednorz, J. and K. Müller, *Sr₁₋ₓCaₓTiO₃: An XY Quantum Ferroelectric with Transition to Randomness.* Physical Review Letters, 1984. **52**(25): p. 2289.

45. Grupp, D.E. and A.M. Goldman, *Giant piezoelectric effect in strontium titanate at cryogenic temperatures.* Science, 1997. **276**(5311): p. 392-394.

46. Rice, W., P. Ambwani, M. Bombeck, J. Thompson, C. Leighton, and S. Crooker, *Persistent optically induced magnetism in oxygen-deficient strontium titanate.* arXiv preprint arXiv:1401.1871, 2014.

47. Levin, S., N. Field, F. Plock, and L. Merker, *Some optical properties of strontium titanate crystal.* JOSA, 1955. **45**(9): p. 737-739.

48. Gandy, H.W., *Optical Transmission of Heat-Treated Strontium titanate.* Physical Review, 1959. **113**(3): p. 795.

49. Paladino, A.E., L.G. Rubin, and J.S. Waugh, *Oxygen ion diffusion in single crystal SrTiO3.* Journal of Physics and Chemistry of Solids, 1965. **26**(2): p. 391-397.

50. Cardona, M., *Optical Properties and Band Structure of SrTiO₃ and BaTiO₃.* Physical Review, 1965. **140**(2A): p. 651-655.

51. Yang, J. and Q. Fan. *Understanding electronic and optical properties of strontium titanate at both PBE and HSE06 levels.* in *IOP Conference Series: Materials Science and Engineering.* 2017. IOP Publishing.

52. Linz, A., *Some Electrical Properties of Strontium Titanate.* Physical Review, 1953. **91**(3): p. 753-754.

53. Barrett, J.H., *Dielectric constant in perovskite type crystals.* Physical Review, 1952. **86**(1): p. 118.

54. Weaver, H., *Dielectric properties of single crystals of SrTiO₃ at low temperatures.* Journal of Physics and Chemistry of Solids, 1959. **11**(3): p. 274-277.

55. Poole, V.M. and M.D. McCluskey. *Large persistent photoconductivity in strontium titanate single crystals.* in *Proc. of SPIE Vol.* 2016.

56. Kröger, F.A. and H.J. Vink, *Relations between the Concentrations of Imperfections in Crystalline Solids.* Solid State Physics, 1956. **3**: p. 307-435.

57. Balachandran, U. and N.G. Eror, *Electrical Conductivity in Strontium Titanate.* Journal of Solid State Chemistry, 1981. **39**: p. 351-359.

58. Moos, R. and K.H. Hardtl, *Defect Chemistry of Donor-Doped and Undoped Strontium Titanate Ceramics between 1000°C and 1400°C* Journal of American Ceramic Society, 1997. **80**(10): p. 2549-61.

59. L.C. Walters, R.E.G., *Formation of point defects in strontium titanate.* Journal of Physics and Chemistry of Solids, 1967. **28**(2): p. 239-244.

60.   Yamada, H. and G. Miller, *Point defects in reduced strontium titanate.* Journal of Solid State Chemistry, 1973. **6**(1): p. 169-177.

61.   Chan, N.H., R.K. Sharma, and D.M. Smyth, *Nonstochiometricity in SrTiO₃.* J. Electrochem. Soc., 1981. **128**(8): p. 1762-1769.

62.   Merkle, R. and J. Maier, *How Is Oxygen Incorporated into Oxides? A Comprehensive Kinetic Study of a Simple Solid-State Reaction with SrTiO3 as a Model Material.* Angewandte Chemie International Edition, 2008. **47**(21): p. 3874-3894.

63.   Denk, I., W. Münch, and J. Maier, *Partial Conductivities in SrTiO3: Bulk Polarization Experiments, Oxygen Concentration Cell Measurements, and Defect-Chemical Modeling.* Journal of the American Ceramic Society, 1995. **78**(12): p. 3265-3272.

64.   Merkle, R. and J. Maier, *Defect association in acceptor-doped SrTiO₃: case study for Fe' Ti V¨ O and Mn "Ti V¨ O.* Physical Chemistry Chemical Physics, 2003. **5**(11): p. 2297-2303.

65.   Yu, C., M.L. Scullin, M. Huijben, R. Ramesh, and A. Majumdar, *The influence of oxygen deficiency on the thermoelectric properties of strontium titanates.* Applied Physics Letters, 2008. **92**(9): p. 092118.

66.   Morin, F. and J. Oliver, *Energy Levels of Iron and Aluminum in SrTiO₃.* Physical Review B, 1973. **8**(12): p. 5847.

67.   Tenne, D., I. Gonenli, A. Soukiassian, D. Schlom, S. Nakhmanson, K. Rabe, and X. Xi, *Raman study of oxygen reduced and re-oxidized strontium titanate.* Physical Review B, 2007. **76**(2): p. 024303.

68.   Moos, R., W. Menesklou, and K. Härdtl, *Hall mobility of undoped n-type conducting strontium titanate single crystals between 19 K and 1373 K.* Applied Physics A: Materials Science & Processing, 1995. **61**(4): p. 389-395.

69.   Bieger, T., J. Maier, and R. Waser, *An Optical In-Situ Method to Study Redox-Kinetics in SrTiO₃.* Berichte der Bunsengesellschaft für physikalische Chemie, 1993. **97**(9): p. 1098-1104.

70.   Shanthi, N. and D. Sarma, *Electronic structure of electron doped SrTiO₃: SrTiO₃₋δ and Sr₁₋ₓLaₓTiO₃.* Physical Review B, 1998. **57**(4): p. 2153.

71.   Lee, B., K.M. Choi, H.-S. Ahn, S. Han, and J. Lee, *Oxygen vacancy clustering and electron localization in oxygen-deficient SrTiO₃: LDA+U study.* Physical review letters, 2007. **98**(11): p. 115503.

72.   Cordero, F., *Hopping and clustering of oxygen vacancies in SrTiO₃ by anelastic relaxation.* Physical Review B, 2007. **76**(17): p. 172106.

73.   De Souza, R.A., V. Metlenko, D. Park, and T.E. Weirich, *Behavior of oxygen vacancies in single-crystal SrTiO₃: equilibrium distribution and diffusion kinetics.* Physical Review B, 2012. **85**(17): p. 174109.

74. Maier, J., G. Schwitzgebel, and H.J. Hagemann, *Electrochemical investigations of conductivity and chemical diffusion in pure and doped cubic SrTiO3 and BaTiO3.* Journal of Solid State Chemistry, 1985. **58**(1): p. 1-13.

75. Eror, N.G. and U. Balachandran, *High-Temperature Defect Structure of Acceptor-Doped Strontium Titanate.* Journal of the American Ceramic Society, 1982. **65**(9): p. 426-431.

76. Paladino, A.E., *Oxidation Kinetics of Single-Crystal SrTiO3.* Journal of the American Ceramic Society, 1965. **48**(9): p. 476-478.

77. Waser, R., *Bulk Conductivity and Defect Chemistry of Acceptor-Doped Strontium Titanate in the Quenched State.* Journal of the American Ceramic Society, 1991. **74**(8): p. 1934-1940.

78. Akhtar, M.J., Z.U.N. Akhtar, R.A. Jackson, and C.R.A. Catlow, *Computer simulation studies of strontium titanate.* Journal of the American Ceramic Society, 1995. **78**(2): p. 421-428.

79. Bunting, E.N., G.R. Shelton, and A.S. Creamer, *Properties of barium-strontium titanate dielectrics.* Journal of the American Ceramic Society, 1947. **30**(4): p. 114-125.

80. Itoh, C., M. Sasabe, and H. Kida, *Electric field-induced retardation of the drift mobility of the photocarriers in SrTiO3 crystal.* Journal of luminescence, 2005. **112**(1-4): p. 263-266.

81. Grabner, L., *Photoluminescence in SrTiO₃.* Physical Review, 1969. **177**(3): p. 1315.

82. Leonelli, R. and J. Brebner, *Time-resolved spectroscopy of the visible emission band in strontium titanate.* Physical Review B, 1986. **33**(12): p. 8649.

83. Rubano, A., D. Paparo, F.M. Granozio, U. Scotti di Uccio, and L. Marrucci, *Blue luminescence of SrTiO₃ under intense optical excitation.* Journal of Applied Physics, 2009. **106**(10): p. 103515.

84. Hasegawa, T., M. Shirai, and K. Tanaka, *Localizing nature of photo-excited states in SrTiO₃.* Journal of Luminescence, 2000. **87**: p. 1217-1219.

85. Mochizuki, S., F. Fujishiro, and S. Minami, *Photoluminescence and reversible photo-induced spectral change of SrTiO3.* Journal of Physics: Condensed Matter, 2005. **17**(6): p. 923.

86. Cord, B. and R. Courths, *Electronic study of SrTiO3 (001) surfaces by photoemission.* Surface Science, 1985. **162**(1-3): p. 34-38.

87. Courths, R., B. Cord, and H. Saalfeld, *Bulk and surface Ti3d valence and defect states in SrTiO₃ (001) from resonant photoemission.* Solid State Communications, 1989. **70**(11): p. 1047-1051.

88. Merkle, R., R.A. De Souza, and J. Maier, *Optically Tuning the Rate of Stoichiometry Changes: Surface-Controlled Oxygen Incorporation into Oxides under UV Irradiation.* Angewandte Chemie, 2001. **113**(11): p. 2184-2187.

89.   Walch, G., *Effects of light on mixed conducting electrodes in high-temperature solid oxide electrochemical cells*. 2016, Vienna University of Technology.

90.   Kawai, M., S. Watanabe, and T. Hanada, *Molecular beam epitaxy of $Bi_2Sr_2CuO_x$ and $Bi_2Sr_2Ca0. 85Sr0. 15Cu_2O_x$ ultra thin films at 300 °C.* Journal of Crystal Growth, 1991. **112**(4): p. 745-752.

91.   Nassau, K. and A. Miller, *Strontium titanate: An index to the literature on properties and the growth of single crystals.* Journal of crystal growth, 1988. **91**(3): p. 373-381.

92.   Hansen, P.J., *AlGaN/GaN metal-oxide-semiconductor heterostructure field-effect transistors using barium strontium titanate.* Journal of Vacuum Science & Technology B: Microelectronics and Nanometer Structures Processing, Measurement, and Phenomena, 2004. **22**: p. 2479-2485.

93.   Setter, N. and R. Waser, *Electroceramic Materials.* Acta Mater, 2000. **48**: p. 151-178.

94.   Kingon, A., J.P. Maria, and S.K. Streiffer, *Alternative dielectrics to silicon dioxide for memory and logic devices.* Nature, 2000. **406**(6799): p. 1032-8.

95.   Janousch, M., G.I. Meijer, U. Staub, B. Delley, S.F. Karg, and B.P. Andreasson, *Role of oxygen vacancies in Cr-doped SrTiO3 for resistance-change memory.* Advanced Materials, 2007. **19**(17): p. 2232-2235.

96.   Waser, R., R. Dittmann, G. Staikov, and K. Szot, *Redox-based resistive switching memories–nanoionic mechanisms, prospects, and challenges.* Advanced Materials, 2009. **21**(25-26): p. 2632-2663.

97.   Gerblinger, J. and H. Meixner, *Fast oxygen sensors based on sputtered strontium titanate.* Sensors and Actuators B: Chemical, 1991. **4**(1): p. 99-102.

98.   Menesklou, W., H.-J. Schreiner, K.H. Härdtl, and E. Ivers-Tiffée, *High temperature oxygen sensors based on doped SrTiO3.* Sensors and Actuators B: Chemical, 1999. **59**(2–3): p. 184-189.

99.   Fergus, J.W., *Perovskite oxides for semiconductor-based gas sensors.* Sensors and Actuators B: Chemical, 2007. **123**(2): p. 1169-1179.

100.   Xing, J., K. Zhao, H. Lu, X. Wang, G. Liu, K. Jin, M. He, C. Wang, and G. Yang, *Visible-blind, ultraviolet-sensitive photodetector based on $SrTiO_3$ single crystal.* Optics Letters, 2007. **32**(17): p. 2526-2528.

101.   Troy K. Townsend, N.D.B., F. Osterloh, *Nanoscale Strontium Titanate Photocatalysts for Overal Water Splitting.* ASC Nano, 2012. **6**(8): p. 7420 - 7426.

102.   Wei, X., G. Xu, Z. Ren, C. Xu, W. Weng, G. Shen, and G. Han, *Single-Crystal-like Mesoporous SrTiO3 Spheres with Enhanced Photocatalytic Performance.* Journal of the American Ceramic Society, 2010. **93**(5): p. 1297-1305.

103.   Miyauchi, M., M. Takashio, and H. Tobimatsu, *Photocatalytic activity of SrTiO3 codoped with nitrogen and lanthanum under visible light illumination.* Langmuir, 2004. **20**(1): p. 232-236.

104. Li, X., H. Zhao, X. Zhou, N. Xu, Z. Xie, and N. Chen, *Electrical conductivity and structural stability of La-doped SrTiO$_3$ with A-site deficiency as anode materials for solid oxide fuel cells.* International Journal of Hydrogen Energy, 2010. **35**(15): p. 7913-7918.

105. Rao, C., O. Parkash, D. Bahadur, P. Ganguly, and S. Nagabhushana, *Itinerant electron ferromagnetism in Sr^{2+}-, Ca^{2+}-, and Ba^{2+}-doped rare-earth orthocobaltites ($Ln^{3+1-x}M^{2+x}CoO_3$).* Journal of Solid State Chemistry, 1977. **22**(3): p. 353-360.

106. Rao, C.N.R. and J. Gopalakrishnan, *NEW DIRECTIONS IN SOLID STATE CHEMISTRY. Edition en anglais.* 1997: Cambridge University Press.

107. Petrov, A., O. Kononchuk, A. Andreev, V. Cherepanov, and P. Kofstad, *Crystal structure, electrical and magnetic properties of La1− xSrxCoO3− y.* Solid State Ionics, 1995. **80**(3-4): p. 189-199.

108. Thornton, G., B. Tofield, and A. Hewat, *A neutron diffraction study of LaCoO3 in the temperature range 4.2< T< 1248 K.* Journal of Solid State Chemistry, 1986. **61**(3): p. 301-307.

109. Kleveland, K., N. Orlovskaya, T. Grande, A.M.M. Moe, M.A. Einarsrud, K. Breder, and G. Gogotsi, *Ferroelastic Behavior of LaCoO3-Based Ceramics.* Journal of the American Ceramic Society, 2001. **84**(9): p. 2029-2033.

110. Mizusaki, J., Y. Mima, S. Yamauchi, K. Fueki, and H. Tagawa, *Nonstoichiometry of the perovskite-type oxides La1− xSrxCoO3− δ.* Journal of Solid State Chemistry, 1989. **80**(1): p. 102-111.

111. Petrov, A., V. Cherepanov, O. Kononchuk, and L.Y. Gavrilova, *Oxygen Nonstoichiometry of La1− xSrxCoO3− δ (0< x≤ 0.6).* Journal of Solid State Chemistry, 1990. **87**(1): p. 69-76.

112. Petrov, A.N., V.A. Cherepanov, and A.Y. Zuev, *Thermodynamics, defect structure, and charge transfer in doped lanthanum cobaltites: an overview.* Journal of Solid State Electrochemistry, 2006. **10**(8): p. 517-537.

113. Lankhorst, M.H., H. Bouwmeester, and H. Verweij, *Use of the rigid band formalism to interpret the relationship between O chemical potential and electron concentration in $La_{1−x}Sr_xCoO_{3−δ}$.* Physical Review Letters, 1996. **77**(14): p. 2989.

114. Lankhorst, M.H., H. Bouwmeester, and H. Verweij, *High-temperature coulometric titration of $La_{1−x}Sr_xCoO_{3−δ}$: Evidence for the effect of electronic band structure on nonstoichiometry behavior.* Journal of Solid State Chemistry, 1997. **133**(2): p. 555-567.

115. Kozhevnikov, V., I. Leonidov, E. Mitberg, M. Patrakeev, A. Petrov, and K.R. Poeppelmeier, *Conductivity and carrier traps in $La_{1−x}Sr_xCo_{1−z}Mn_zO_{3-δ}$ (x= 0.3; z= 0 and 0.25).* Journal of Solid State Chemistry, 2003. **172**(2): p. 296-304.

116. Patrakeev, M., I. Leonidov, E. Mitberg, A. Lakhtin, V. Vasiliev, V. Kozhevnikov, and K. Poeppelmeier, *Oxygen thermodynamics and ion conductivity in the solid solution La1− xSrxCoO3− δ at large strontium content.* Ionics, 1999. **5**(5-6): p. 444-449.

117. Jonker, G., *Semiconducting properties of lanthanum-cobalt oxide(Semiconducting properties of lanthanum-cobalt oxide measured, using Seebeck coefficient for analysis as function of resistivity).* Philips Research Reports, 1969. **24**: p. 1-14.

118. Matsuura, T., J. Tabuchi, J. Mizusaki, S. Yamauchi, and K. Fueki, *Electrical properties of $La_{2-x}Sr_xCoO_{4-1}$: Structure, electrical conductivity, and Seebeck coefficient of single crystals x= 0.0, 0.5, 1.0 and 1.5.* Journal of Physics and Chemistry of Solids, 1988. **49**(12): p. 1403-1408.

119. Mineshige, A., M. Inaba, T. Yao, Z. Ogumi, K. Kikuchi, and M. Kawase, *Crystal Structure and Metal–Insulator Transition of $La1-xSrxCoO3$.* Journal of Solid State Chemistry, 1996. **121**(2): p. 423-429.

120. Mizusaki, J., J. Tabuchi, T. Matsuura, S. Yamauchi, and K. Fueki, *Electrical Conductivity and Seebeck Coefficient of Nonstoichiometric $La_{1-x}Sr_xCoO_{3-\delta}$.* Journal of the Electrochemical Society, 1989. **136**(7): p. 2082-2088.

121. Jonker, G. and J. Van Santen, *Magnetic compounds with perovskite structure III. ferromagnetic compounds of cobalt.* Physica, 1953. **19**(1-12): p. 120-130.

122. Torrance, J.B., P. Lacorre, C. Asavaroengchai, and R.M. Metzger, *Why are some oxides metallic, while most are insulating?* Physica C: Superconductivity, 1991. **182**(4-6): p. 351-364.

123. Sarma, D., A. Chainani, R. Cimino, P. Sen, C. Carbone, M. Mathew, and W. Gudat, *Electronic Structure of and the Metal-Insulator Transition in $La1-xSrxCoO3-\delta$: A Soft-X-Ray Absorption Study.* EPL (Europhysics Letters), 1992. **19**(6): p. 513.

124. Arima, T., Y. Tokura, and J. Torrance, *Variation of optical gaps in perovskite-type 3d transition-metal oxides.* Physical Review B, 1993. **48**(23): p. 17006.

125. Chainani, A., M. Mathew, and D. Sarma, *Electron-spectroscopy study of the semiconductor-metal transition in $La_{1-x}Sr_xCoO_3$.* Physical Review B, 1992. **46**(16): p. 9976.

126. Berenov, A., A. Atkinson, J. Kilner, E. Bucher, and W. Sitte, *Oxygen tracer diffusion and surface exchange kinetics in La 0.6 Sr 0.4 CoO 3− δ.* Solid State Ionics, 2010. **181**(17): p. 819-826.

127. Kaga, Y., Y. Ohno, K. Tsukamoto, F. Uchiyama, M. Lain, and T. Nakajima, *Relationships between the gas permeabilities and the microstructures of plasma sprayed oxide layers.* Solid State Ionics, 1990. **40**: p. 1000-1002.

128. Ohno, Y., S. Nagata, and H. Sato, *Effect of electrode materials on the properties of high-temperature solid electrolyte fuel cells.* Solid State Ionics, 1981. **3**: p. 439-442.

129. Tedmon, C., H. Spacil, and S. Mitoff, *Cathode materials and performance in high-temperature zirconia electrolyte fuel cells.* Journal of the Electrochemical Society, 1969. **116**(9): p. 1170-1175.

130. Hjalmarsson, P., M. Søgaard, and M. Mogensen, *Electrochemical performance and degradation of $(La_{0.6}Sr_{0.4})_{0.99}CoO_{3-\delta}$ as porous SOFC-cathode.* Solid State Ionics, 2008. **179**(27): p. 1422-1426.

131. Nakamura, T., M. Misono, and Y. Yoneda, *Reduction-oxidation and catalytic properties of $La1-xSrxCoO3$.* Journal of Catalysis, 1983. **83**(1): p. 151-159.

132. Teraoka, Y., H.-M. Zhang, S. Furukawa, and N. Yamazoe, *Oxygen permeation through perovskite-type oxides.* Chemistry Letters, 1985. **14**(11): p. 1743-1746.

133. Tang, W. and D. Cameron, *Aluminum-doped zinc oxide transparent conductors deposited by the sol-gel process.* Thin Solid Films, 1994. **238**(1): p. 83-87.

134. Sang, B., A. Yamada, and M. Konagai, *Textured ZnO thin films for solar cells grown by a two-step process with the atomic layer deposition technique.* Japanese journal of applied physics, 1998. **37**(2B): p. L206.

135. Hosono, E., S. Fujihara, I. Honma, and H. Zhou, *The fabrication of an upright-standing zinc oxide nanosheet for use in dye-sensitized solar cells.* Advanced Materials, 2005. **17**(17): p. 2091-2094.

136. Ko, S.C., Y.C. Kim, S.S. Lee, S.H. Choi, and S.R. Kim, *Micromachined piezoelectric membrane acoustic device.* Sensors and Actuators A: Physical, 2003. **103**(1-2): p. 130-134.

137. Hossain, F.M., J. Nishii, S. Takagi, T. Sugihara, A. Ohtomo, T. Fukumura, H. Koinuma, H. Ohno, and M. Kawasaki, *Modeling of grain boundary barrier modulation in ZnO invisible thin film transistors.* Physica E: Low-dimensional Systems and Nanostructures, 2004. **21**(2-4): p. 911-915.

138. Nishii, J., F.M. Hossain, S. Takagi, T. Aita, K. Saikusa, Y. Ohmaki, I. Ohkubo, S. Kishimoto, A. Ohtomo, and T. Fukumura, *High mobility thin film transistors with transparent ZnO channels.* Japanese journal of applied physics, 2003. **42**(4A): p. L347.

139. Norris, B., J. Anderson, J. Wager, and D. Keszler, *Spin-coated zinc oxide transparent transistors.* Journal of Physics D: Applied Physics, 2003. **36**(20): p. L105.

140. Ma, J., F. Ji, H.-l. Ma, and S.-Y. Li, *Electrical and optical properties of ZnO: Al films prepared by an evaporation method.* Thin Solid Films, 1996. **279**(1-2): p. 213-215.

141. Tominaga, K., M. Kataoka, H. Manabe, T. Ueda, and I. Mori, *Transparent ZnO: Al films prepared by co-sputtering of ZnO: Al with either a Zn or an Al target.* Thin Solid Films, 1996. **290**: p. 84-87.

142. Zafar, S., C. Ferekides, and D. Morel, *Characterization and analysis of ZnO: Al deposited by reactive magnetron sputtering.* Journal of Vacuum Science & Technology A: Vacuum, Surfaces, and Films, 1995. **13**(4): p. 2177-2182.

143. Pechini, P.M., *Method of preparing lead and alkaline earth titanates and niobates and coating method using the same to form a capacitor.* 1967, Google Patents.

144. Rupp, G., *Unravelling the relationship between surface chemistry and oxygen exchange kinetics of (La,Sr)CoO3-δ thin film cathodes*. 2016, Vienna University of Technology.

145. Mastrikov, Y.A., R. Merkle, E. Heifets, E.A. Kotomin, and J. Maier, *Pathways for oxygen incorporation in mixed conducting perovskites: A DFT-based mechanistic analysis for (La, Sr) MnO3− δ*. The Journal of Physical Chemistry C, 2010. **114**(7): p. 3017-3027.

146. Huber, T., *Konstruktion einer Vakuum-Mikrokontaktapparatur und Impedanzmessungen an mikrostrukturierten Platin- und Nickelelektroden auf Yttrium stabilisiertem Zirconiumoxid in Wasserstoff Atmosphäre*. 2010, Vienna University of Technology.

147. Rotter, B., *in preparation*. 2016, Vienna University of Technology.

148. Powell, R.W., R.P. Tye, and J. Woodman Margaret, *Thermal Conductivities and Electrical Resistivities of the Platinum Metals*. Platinum Metals Review, 1962. **6**(4): p. 138-143.

149. Adler, S.B., *Factors governing oxygen reduction in solid oxide fuel cell cathodes*. Chemical reviews, 2004. **104**(10): p. 4791-4844.

150. Chopra, K., S. Major, and D. Pandya, *Transparent conductors—a status review*. Thin solid films, 1983. **102**(1): p. 1-46.

151. Henrich, V.E., G. Dresselhaus, and H. Zeiger, *Chemisorbed phases of O2 on TiO2 and SrTiO3*. Journal of Vacuum Science and Technology, 1978. **15**(2): p. 534-537.

152. Yamada, Y. and Y. Kanemitsu, *Photoluminescence spectra of perovskite oxide semiconductors*. Journal of Luminescence, 2013. **133**: p. 30-34.

153. Scullin, M.L., C. Yu, M. Huijben, S. Mukerjee, J. Seidel, Q. Zhan, J. Moore, A. Majumdar, and R. Ramesh, *Anomalously large measured thermoelectric power factor in Sr 1− x La x Ti O 3 thin films due to Sr Ti O 3 substrate reduction*. Applied physics letters, 2008. **92**(20): p. 202113.

154. Huber, T.M., A.K. Opitz, M. Kubicek, H. Hutter, and J. Fleig, *Temperature gradients in microelectrode measurements: Relevance and solutions for studies of SOFC electrode materials*. Solid State Ionics, 2014. **268**: p. 82-93.

155. Kubicek, M., A. Wachter-Welzl, D. Rettenwander, R. Wagner, S. Berendts, R. Uecker, G. Amthauer, H. Hutter, and J.r. Fleig, *Oxygen Vacancies in Fast Lithium-Ion Conducting Garnets*. Chemistry of Materials, 2017. **29**(17): p. 7189-7196.